

**Master Thesis in Geosciences**

# **Post-impact sedimentation in the Ritland impact structure, South- western Norway**

**Michał Tomczyk**



**UNIVERSITY OF OSLO**

**FACULTY OF MATHEMATICS AND NATURAL SCIENCES**

Dedicated to my mother, Barbara Tomczyk,  
to whom I owe everything

## Contents

1.	Introduction .....	4
2.	Impact geology .....	6
2.1	The origin and formation of impact structures .....	6
2.2	Terrestrial impact structures .....	8
3.	Geological setting .....	10
3.1	Target rocks – the sub-Cambrian peneplain .....	11
3.2	The impact event .....	13
3.3	Post impact – the Cambrian transgression and the Caledonian orogeny .....	13
4.	Methods .....	14
4.1	Field logging and sampling .....	14
4.2	Mineralogical and petrographical analysis .....	15
4.2.1	Thin sections .....	15
4.2.2	XRD analysis .....	16
4.2.3	Lidar survey .....	17
5.	Sedimentological description .....	19
5.1	Sedimentological logs .....	19
5.2	Facies description .....	25
5.3	Facies associations .....	30
5.3.1	Facies association 1 .....	39
5.3.2	Facies association 2 .....	40
5.3.3	Facies association 3 .....	41
6.	Mineralogical and petrographical description .....	42
6.1	Thin section analysis .....	42
6.1.1	Thin section analysis of samples from facies association 1 .....	43
6.1.2	Thin section analysis of samples from facies association 2 .....	44
6.1.3	Thin section analysis of samples from facies association 3 .....	48
6.2	X-ray diffraction analysis .....	51
6.2.1	Facies association 1 .....	52
6.2.2	Facies association 2 .....	52
6.2.3	Facies association 3 .....	53
7	Lidar acquisition data .....	59
8.1	Lower succession – suevite and breccia at the base .....	62
8.1.1	Suevite .....	62
8.1.2	Breccia at the base .....	63
8.2	Middle succession – sandstone sub-unit .....	66
8.2.1	Parallel-bedded sandstone .....	66
8.2.2	Low angle cross-stratified sandstone .....	68
8.2.3	Massive sandstone .....	70
8.3	Upper succession – conglomerate sub-unit and sedimentary breccia .....	72
8.3.1	Conglomerate .....	72
8.3.2	Conglomeratic sandstone .....	74
8.3.3	Soft sediment deformed sandstone .....	74
8.3.4	Matrix supported sedimentary breccia .....	75
8.3.5	Clast supported sedimentary breccia .....	75
9	Conclusions .....	79
	REFERENCES .....	81
	APPENDICES .....	87

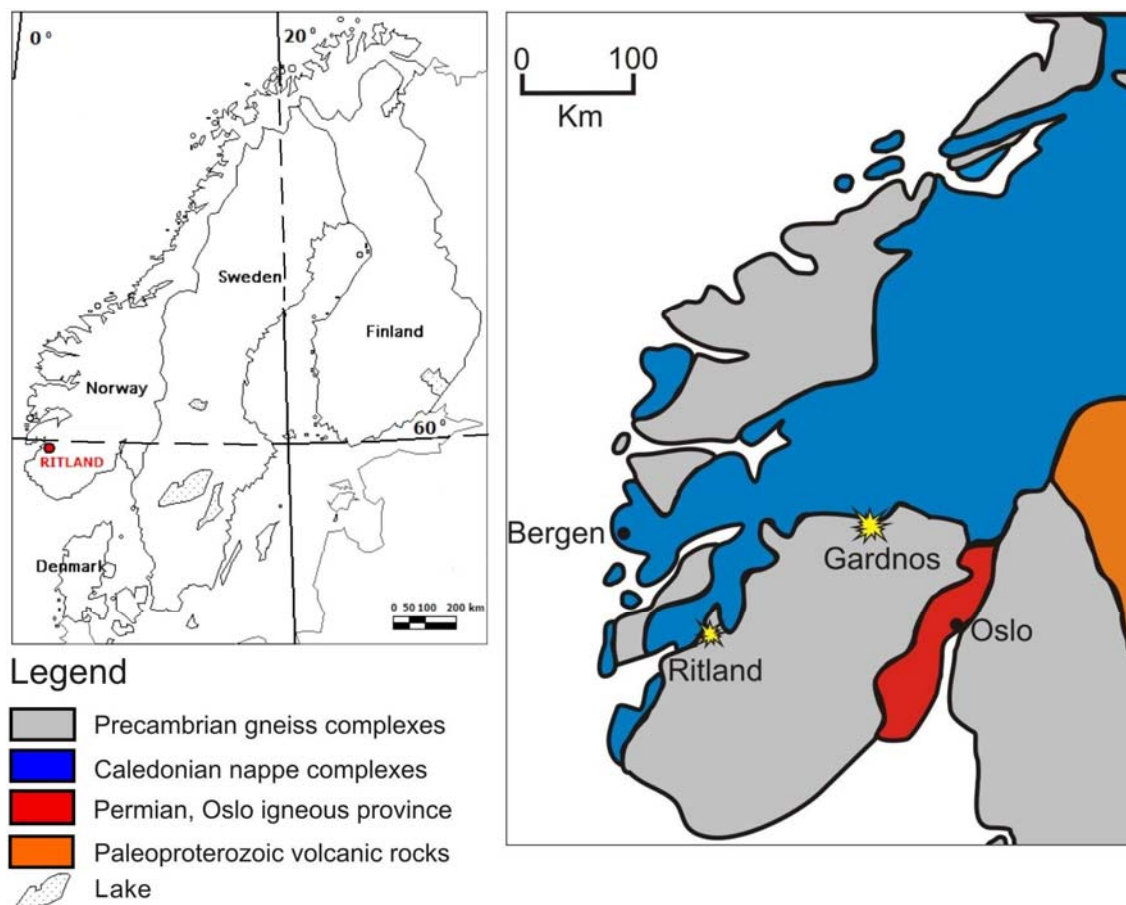
## ABSTRACT

A succession of crater infill sediments is preserved within the Ritland impact structure. Ritland is good example of a small depositional basin where a range of processes from debris flows to turbiditic currents and finally suspension fall-out took place within a very restricted area. Immediately after impact slumps/slides, and mass flows dominated, later to be replaced by running water activities in much calmer basin environment, like fine-grained sedimentation. The sedimentary successions of this small crater, which most likely was a terrestrial impact structure, reveal a shifting depositional environment. Just after the impact accommodation space for sediments was created in an extremely short period. The post-impact breccias covering the crater floor were most likely deposited by rock avalanches, triggered by collapse of crater rim. Breccia deposits interfingering with melt rocks (suevite) and ejecta, which were formed and deposited seconds after impact. The overlying lacustrine sediments, around the center of the crater, suggesting that a temporary lake was present at some time after the impact. Probably groundwater seepage, through the crushed basement, filled the structure to some level and initiated sediment deposition in water reservoir. The succeeding conglomeratic and sandy sequence characterizes local thickness variation. This sequence was deposited by various catastrophic sediment gravity flows, such as turbidity currents, debris flows, slides and slumps, likely triggered by the resurging water, during the Cambrian marine transgression. The resurging water breached the crater rim, which caused its collapse, producing series of rock avalanches. The crater was finally covered by sea and previous rapid depositional processes switched into deep water sedimentation processes (probably not very deep – epicontinental sea). Shales covering gravity flow deposits represent the reestablishment of quiet conditions.

## 1. Introduction

The Ritland structure is located in the community of Hjelmeland, county of Rogaland (south-western Norway) and represents the eroded remnant of an (likely) early Cambrian impact crater (Fig. 1). The crater formed when an approximately 100 m large rock (small asteroid?) collided with Earth and within seconds or minutes excavated a 2.5 km wide and 350 m deep hole (Riis et al., 2009). This study will focus on the distribution and depositional history of the crater infill sediments. The sediment infill of the structure is a complicated mosaic of various facies of several sedimentary depositional processes. Some of them were rapid (rock avalanches, landslides etc.) and some spanned extensive periods of time (e.g.

shallow sea sedimentation). Studying sedimentary facies is important in understanding the different depositional environments and associated processes after impact.



**Figure 1.** Geographic location (left) and geological map of the southern part of Norway (right) shows two impact structures (yellow symbols): the Gardnos Crater and the Ritland Crater. Grey colour represents South-western gneiss province (900-1700 Ma), blue colour represents Scandinavian Caledonides (400-700 Ma), red colour is rocks within the Oslo rift (volcanic rocks from 250-300 Ma and Cambro-Silurian sediments from 540-400?) and orange indicates volcanic rocks from the Paleoproterozoic (2500-1600 million years ago).

This master thesis is a part of a project on the Ritland impact structure, funded by the Research Council of Norway (NFR). The project is headed by professor Henning Dypvik (UiO) and Fridtjof Riis (NPD), and includes one post-doc, one ph.D. and several masters students. The project will try to answer questions like:

- Time of impact (?),
- Environment of impact (terrestrial or marine?),
- Initial shape and size of crater (immediately post-impact?),
- Properties of the extraterrestrial impactor (?),
- Energy of impact and mechanisms of basement deformation (?),

- Comparison of the Ritland and Gardnos structures (?) etc.

The aim of this master thesis is to describe and discuss sedimentary successions of the Ritland impact structure (mainly from the Svodene Hill in the central-to-southern part of the structure) and explain the processes of deposition within. The Ritland project is still in an early stage of investigation. Comparing the observations from Ritland with published data from similar structures like Gardnos (Hallingdal, Norway) or the Crater Lake (Oregon, the United States), I will try to illustrate the possible sedimentary processes that took place and how they developed through time in the Ritland structure.

## **2. Impact geology**

Scientists expressed first concerns over impact structures in perspective of lunar exploration. The astronauts who trained in the Ries crater in Germany before going to the moon, wanted to know what sorts of rocks they should expect (equivalents of the lunar regolith) (Margolin, 2000). Much more scientific investigations (Shoemaker, 1963; Grieve et al., 1981; Stöffler et al., 1988; Grieve and Pesonen, 1991), concerning aspects of geology of impact structures, were undertaken when scientists have discovered that the collision of the extraterrestrial object with the Earth could be the reason of the mass extinctions in the history of the planet (Alvarez et al., 1980).

### **2.1 The origin and formation of impact structures**

An impact structure is a depression in topography caused by the hypervelocity impact of a solid body from space. These bodies are asteroids and comets of different type and size. Small objects (with diameters smaller than ~50-100 m) frequently collide with the Earth, usually not hit the ground as a single body (Brown et al., 2002). Very large objects (a few kilometers in diameter) are rare, but their impacts can form craters hundreds kilometers in diameter (Atkinson et al., 2000). These enormous impacts may have caused some of the world's big extinction events, but only one has so far been proven. The big mass extinction between the Cretaceous and Paleogene periods (around 65 million years ago) were first proven to coincide with an iridium anomaly at the K-P boundary<sup>1</sup> all over the world and an extraterrestrial explanation suggested (Alvarez et al., 1980). Later the Chicxulub impact

---

<sup>1</sup> K-P boundary – K is the abbreviation for the Cretaceous period, and P is the abbreviation for the Paleogene period. It is a thin band of sediments contain a very high concentration of iridium (Alvarez et al., 1980). This is a proof of an extraterrestrial reason of the mass extinction.

structure (more than 180 km in diameter) was discovered linked to the mass extinction event (Hildebrand et al., 1991).

Impact cratering is an important geological process. We can distinguish two main types of impact structure: simple and complex structures. Generally the smaller craters have a simple form and the large ones are complex, i.e. they may have an uplifted center (very big craters, which have diameters of hundreds of kilometres, may have multi ring structures) (French, 1998). The Ritland impact structure is a simple crater<sup>2</sup> (Riis et al., 2009), and therefore this thesis introduction will concentrate on such type of crater. The Ritland structure is a rather small such structure on the Earth (comparing to the Vredefort Crater in Africa, the Ritland structure is 100 times smaller) (from the Earth Impact Database, 2010). Even so, the impact in Ritland involved a lot of energy (it is comparable to the San Francisco earthquake in 1906 of magnitude 8.4)<sup>3</sup>.

There are three stages of crater's development (Gault et al., 1968; Melosh, 1989; Fig. 2):

- 1) Contact/compression stage,
- 2) Excavation stage,
- 3) Modification stage

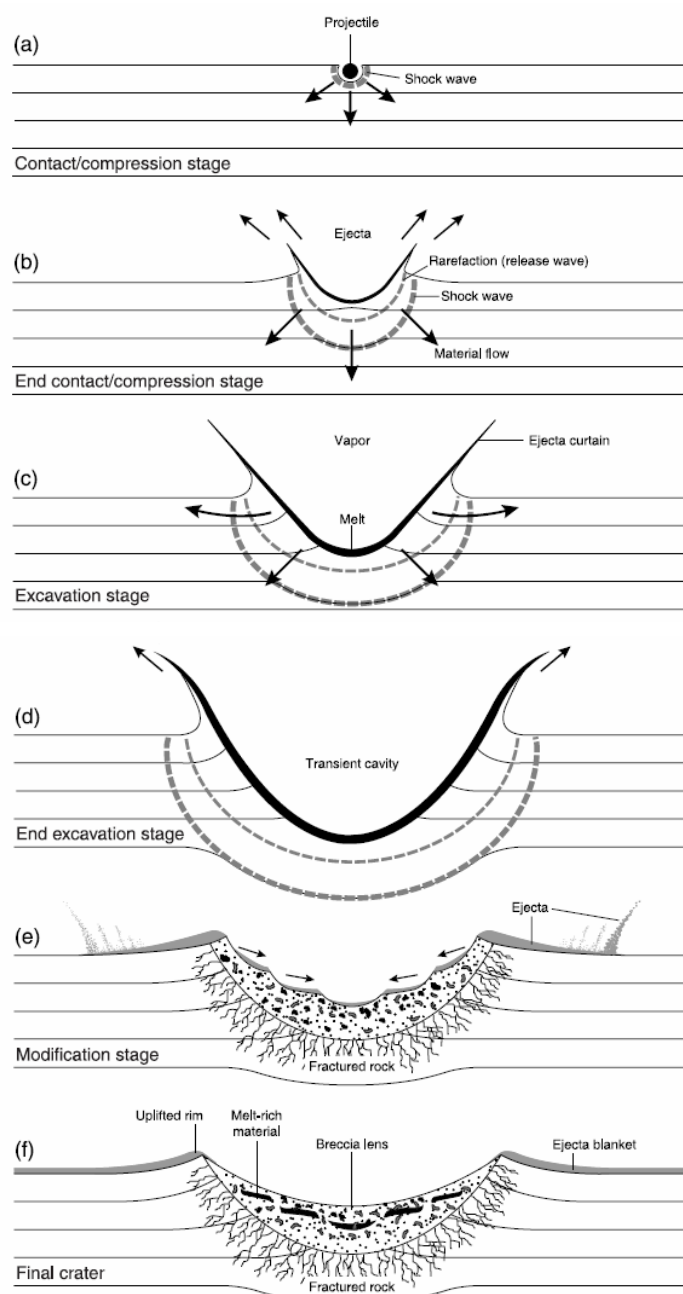
The *contact/compression stage* (Fig. 2a-2b) is very rapid and starts when the bolide impacts the ground surface. Target rocks absorb impact forces of the projectile. The projectile penetrates no more than 1-2x its own diameter (French, 1998). The kinetic energy transforms during the impact, into heat, consequently the vast volume of rock is melted and vaporized. The *excavation stage* (Fig. 2c-2d) lasts longer than the *contact/compression stage*. During this stage an open cavity is formed due to the expanding shock waves in the target rock, in addition the crater rim uplift develops. The fractured and shattered material is driven by these complex processes outward from the impact point. In the upper levels of target rock, material moves upward and outward. At lower levels, target material moves downward and outward (French, 1998). These movements in symmetrical pattern form a bowl-shaped depression (the transient crater) in the target rocks (Maxwell, 1977; Grieve et al., 1977; Grieve and Cintala, 1981; Melosh, 1989). During the last stage, the *modification stage* (Fig. 2e-2f), the transient crater is reaching its maximum size (French, 1998). Gravity processes take control in the structure (mass movements). Material from the crater rim is transferred to the center of the

---

<sup>2</sup> Simple craters occur as a bowl-shaped depression less than a few kilometers across (Melosh, 1989, p.129) and a structurally upraised rim.

<sup>3</sup> Estimation based on the Earth Impact Effects Program: <http://impact.ese.ic.ac.uk/ImpactEffects/>

structure and finally deposited. These changes in the crater last for less than a minute for small structure, a few for a large one (Melosh, 1989).



**Figure 2.** Development of a simple impact structure. Series of cross-section diagrams showing progressive development of a small, bowl-shaped simple impact structure in a horizontally layered target: **(a)** contact/compression stage: initial penetration of projectile, outward radiation of shock waves; **(b)** start of excavation stage: continued expansion of shock wave into target; development of tensional wave (rarefaction or release wave) behind shock wave as the near-surface part of original shock wave is reflected downward from ground surface; interaction of rarefaction wave with ground surface to accelerate near-surface material upward and outward; **(c)** middle of excavation stage: continued expansion of shock wave and rarefaction wave; development of melt lining in expanding transient cavity; well-developed outward ejecta flow (ejecta curtain) from the opening crater; **(d)** end of excavation stage: transient cavity reaches maximum extent to form melt-lined transient crater; near-surface ejecta curtain reaches maximum extent, and uplifted crater rim develops; **(e)** start of modification stage: oversteepened walls of transient crater collapse back into cavity, accompanied by nearcrater ejecta, to form deposit of mixed breccia (breccia lens) within crater; **(f)** final simple crater: a bowl-shaped depression, partially filled with complex breccias and bodies of impact melt. Times involved are a few seconds to form the transient crater **(a)–(d)**, and minutes to hours for the final crater **(e)–(f)**. Subsequent changes reflect the normal geological processes of erosion and infilling (Figures and Figure text from French, 1998).

## 2.2 Terrestrial impact structures

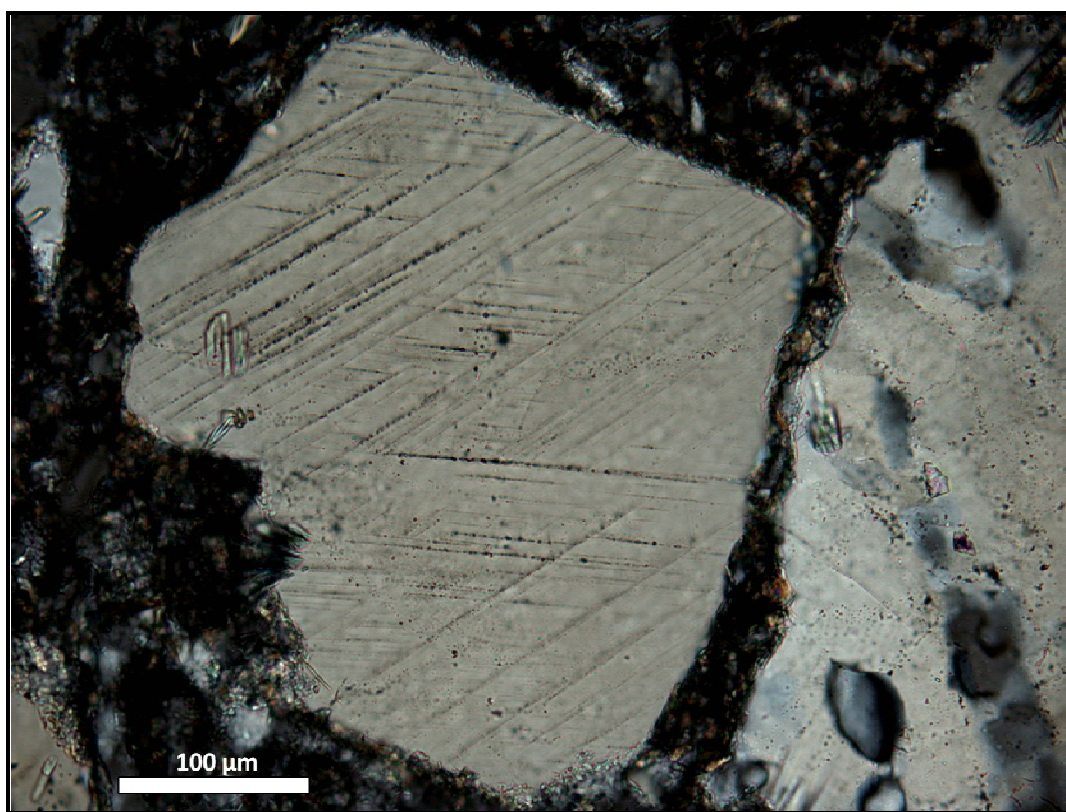
Only 19 % of the total number 176 confirmed impact structures are structures formed before the end of the Cambrian period (around 488 Ma)<sup>4</sup>. These old craters often are poorly

<sup>4</sup> Estimation based on data from the Earth Impact Database: [www.unb.ca/passc/ImpactDatabase/](http://www.unb.ca/passc/ImpactDatabase/)



preserved on Earth and remain undiscovered. In spite of a high unclear of impact at the time a low number has been found. The target rocks for these impacts were in most cases basement rocks. The discovered impact structures are located in the relatively geological stable cratonic areas of North America, Scandinavia, west Russia and Australia. These conditions favor good preservation of terrestrial impact structures (Grieve et al., 1997). The crater infills, some of these structures, have been excavated due to erosional processes.

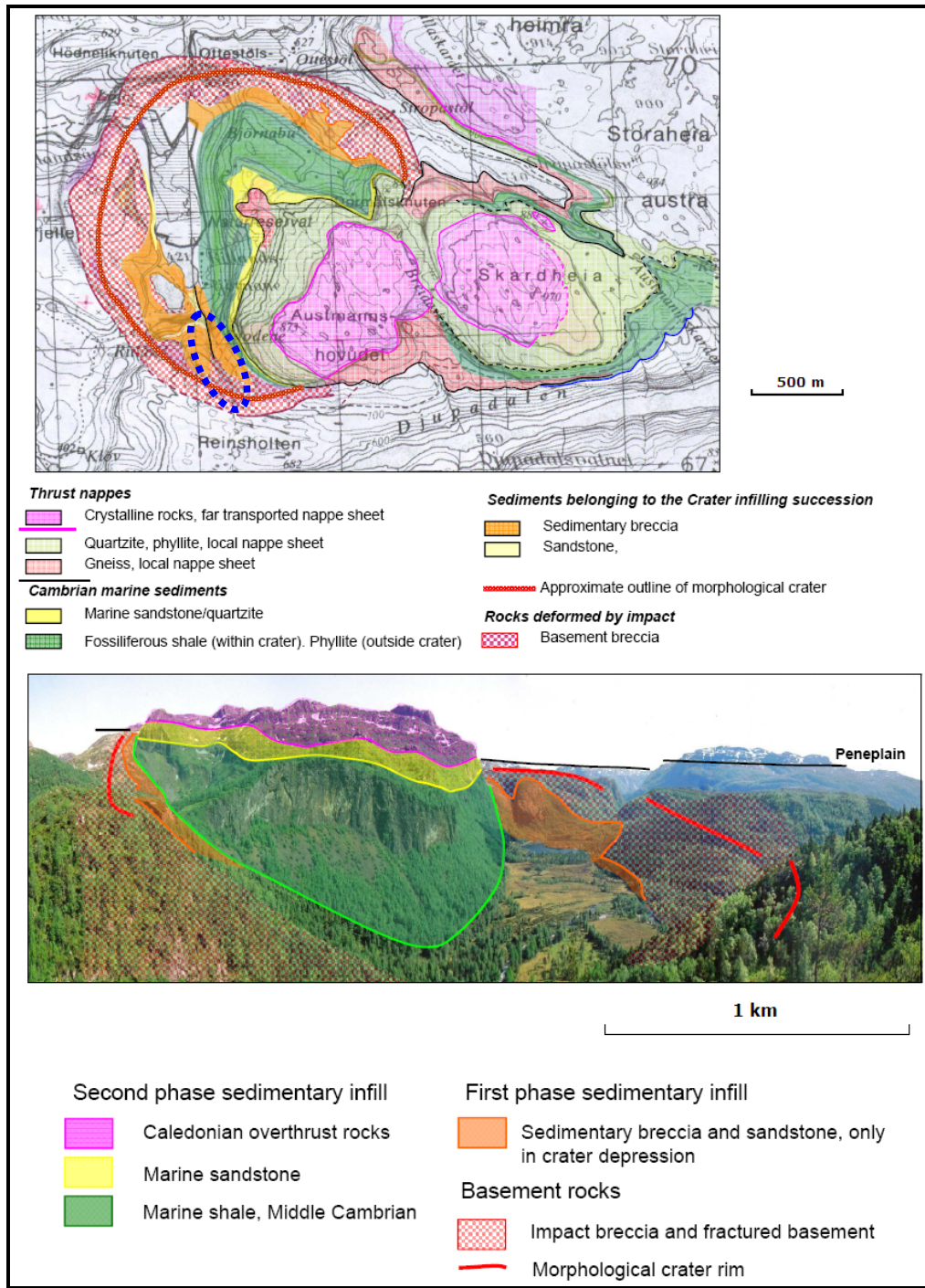
The hypothesis that the Ritland structure might be an impact structure was first suggested by Riis (2002), based on geological mapping of the structure. The first samples with clearcut shock deformed grains of quartz were found in the crater in 2007 (Riis et al., 2009), and during summer of 2009 the Ritland project group found additional exposures of melt rocks. Samples gathered from this location carried large numbers of quartz grains with characteristic shock features – PDF (Koeberl, 2006; Fig. 3). The PDFs are clear evidence for impact origin of the Ritland structure (Shoemaker, 1963; Langenhorst and Deutsch, 1993).



**Figure 3.** PDFs features of one shocked quartz grain found in the Ritland Crater, in 2009, sample RITT-10-3-09; the thin section image provided by Elin Kalleson (UiO)

### **3. Geological setting**

The Ritland impact structure represents a simple impact structure; 2,5 km in diameter and about 350 metres deep (Riis, 2009). The age of the Ritland structure is not certain, but shales deposited in the crater contain fossils dated to the middle Cambrian – making it certain that the impact occurred before that time (Henningsmoen 1952, Bruton and Harper 2000), therefore, Riis et al. (2009) estimated the age of the crater between 500 and 600 million years ago. The formation suffered several events of uplift, erosion and finally the Pleistocene glaciations. The last postglacial events helped to uncover the sedimentary crater infill and create a three-dimensional surface depression (Riis et al., 2009). Minor amount of impact melt rock, crater infill sediments, Cambrian shales and overlying sandstone are presently formed within the structure, covered by remnants of Caledonian thrust nappes (Fig. 4).



**Figure 4.** Top: the geological map of the Ritland structure, the Svodene Hill, study area of this thesis, is marked by dashed line ellipse; Bottom: the panoramic photo with the sedimentary succession description (modified from Riis et al., 2009).

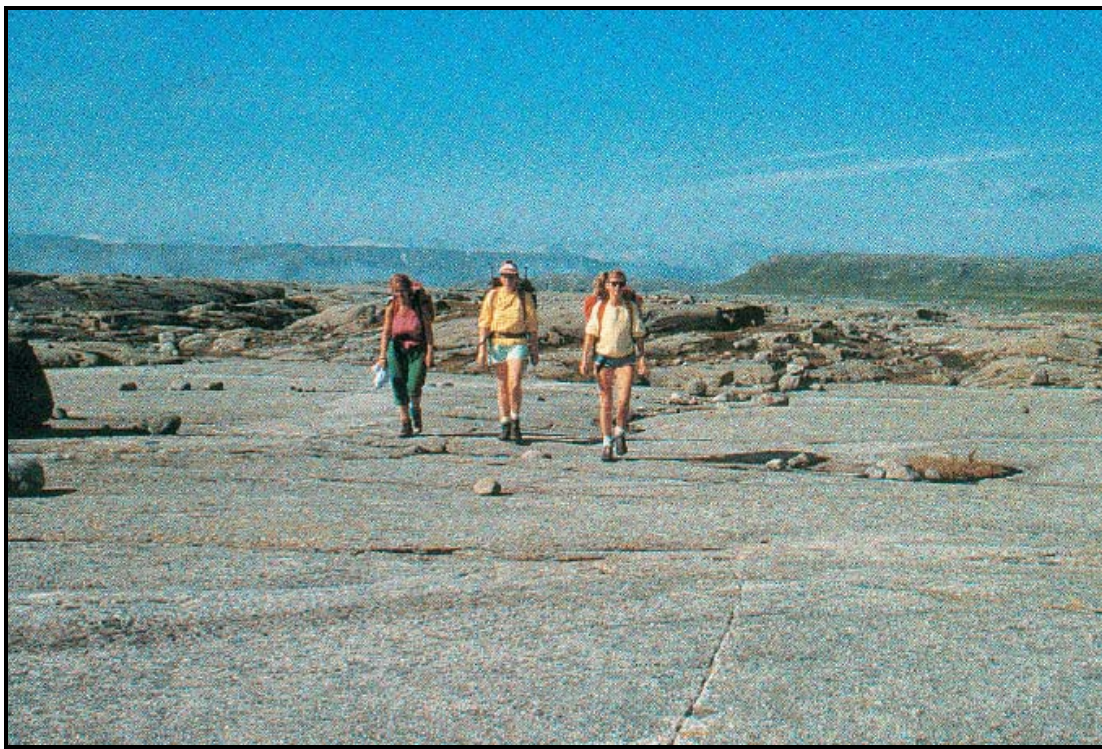
### 3.1 Target rocks – the sub-Cambrian peneplain

The meteorite impacted into the sub-Cambrian peneplain which was composed of Precambrian gneissic rocks (Riis et al., 2009). The sub-Cambrian peneplain is today exposed as a conspicuous flat to slightly undulating surface in the mountainous areas of southern



Norway and also 2-5 km east of Ritland (Fig. 5). Target rocks in the area are dated from 1750 to 900 million years. The Precambrian evolution of southern Norway culminated with the Sveconorwegian orogeny 1130-900 million years ago, when mostly granitic rocks were folded, strongly deformed and metamorphosed (Nordgulen and Andresen, 2008).

The Sveconorwegian orogeny was induced by collision between the Laurentia-Fennoscandia margin and the Amazonia indenter (Bingen et al., 2008). The plate amalgamation created the continent, Rodinia. When the supercontinent had started to break up about 850 million years ago, the old rocks from the Fennoscandian shield were exposed to erosion. At that time the new plate/continent, Baltica was born, Norway was a part of Baltica, which replaced Fennoscandia. The basement rocks were eroded during the Varangerian glaciations, around 700 million years ago. Later tropical climate during the Ediacaran Period (630-542 years ago) caused deep weathering of the basement (Ramberg eds., 2008). The eroded surface, the sub-Cambrian peneplain, represents a hiatus which indicates the boundary between Precambrian metamorphic and igneous rocks and overlying Cambro-Silurian deposits (Riis et al., 2009). In Scandinavia the peneplain often marks a morphological surface (e.g. Lidmar-Bergström and Näslund 2002).



**Figure 5.** The exhumated sub-Cambrian peneplain (from Riis et al., 2009).

### **3.2 The impact event**

When the meteorite impacted the sub-Cambrian peneplain, Ritland was probably located at the Baltoscandia margin, on the north-western rim of Baltica (500-600 Ma) (Meert and Torsvik, 2004). In addition to excavating a crater, the rocks beneath the crater floor were fractured and brecciated. The basement rocks exposed along the crater walls today are intensely fractured and brecciated, commonly with a characteristic dark grey to black fracture fill. The quartz and feldspar grains typically have dark grey to black colour and individual quartz grains commonly display a mosaic fracture pattern and strongly undulating extinction (Riis et al., 2009).

Three meteorite impact craters have so far been recognised in Norway. Two of them are located on land: the Gardnos structure (French et al., 1997; Kalleson et al., 2008) and the Ritland structure (Riis et al., 2009). The third structure is located in the Barents Sea, the Mjølner structure (Dypvik and Jansa, 2003; Dypvik et al., 2004; Dypvik et al. 2006). The first two formations have similar features: comparable age of crater formation (the late Precambrian), the location in front of the Caledonian overthrust rocks (Fig. 1), the target rock (the Precambrian basement). Probably meteorites fell on land (the Ritland structure; Riis et al., 2009) or into shallow sea (the Gardnos structure; French et al., 1997) in late Precambrian/early Cambrian, when Norway was located on the north-western rim of Baltica at the time (Meert and Torvik, 2004). During last glaciations younger strata were eroded from the sub-Cambrian peneplain, and the Gardnos structure and the Ritland structure have been excavated.

### **3.3 Post impact – the Cambrian transgression and the Caledonian orogeny**

Within the crater, the crushed basement rocks are covered by sedimentary, post-impact breccias with fragments reaching up to 2-3 m. In the deeper part of the crater depression, the sedimentary breccia is intercalated with crossbedded sandstones, deposited in water. Overlying coarse-grained deposits form wedges of variable thickness along the margin of the structure. The maximum stratigraphic thickness observed is almost 200 m along the rim of the crater (Fig. 13) (Riis et al., 2008).

At the end of Precambrian Baltica began to fracture and split into two continents: the Baltica and Laurentia. A huge rifting zone separated these continents and gave the start to a new ocean, Iapetus (Worsley and Nakrem, 2008). The water level rose resulting in flooding, and vast areas of Baltica were transgressed. During an early Cambrian marine transgression

the crater was dominated by fine-grained sedimentation, in the field seen as shales onlapping the crater walls (Fig. 4 and 13).

On the peneplain east of the Ritland Crater, a fine grained, bioturbated sandstone bed is found. This thin unit (up to 10-20 m) was widely distributed during the Cambrian marine transgression, and it covers Cambrian shales in the Ritland structure (Fig. 13) (Riis et al., 2008).

The whole impact structure was covered by thrust nappes of the Caledonian Orogen in the Silurian-Devonian times. The crust was detached and moved hundreds of kilometres from northwest to southeast at the time (Fossen et al., 2008). These overlying nappes partly protected the crater from post Caledonian erosion.

## **4. Methods**

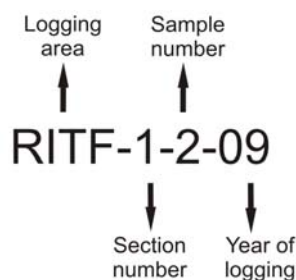
Several different methods were applied to study the sediments at Ritland. Classical field logging and observations in combination with Lidar data acquisition represent the macroscale observations. The mineralogical and petrographical analysis (thin section and XRD) revealed details in micro scale.

### **4.1 Field logging and sampling**

The field logging was performed from 11<sup>th</sup> to 20<sup>th</sup>, on August 2009, in the Ritland structure. This work focused on mainly one area, the Svodene hill, in the southern part of the structure (Fig. 4). The Svodene hill is a large continuous outcrop (maximum 90 m in height and 350 m in width) which offers three dimensional exposures of the crater's infill. Three sections have been logged: RITF-1 (around 18 m; Fig. 9), RITF-3 (around 48 m; Fig. 10), RITF-4 (around 22 m; Fig. 11). It was difficult to log the section between RITF-1 and RITF-3, as had been planned, due to a very hard working conditions there (too steep cliff). The sections were logged on logging sheets in the scale of 1:50. The rock exposures were investigated with the aid of hand-lens, ruler, hammer, compass, grain-size scale, camera etc. The Lidar (altitude) and GPS (position) measurements were used to correlate all logs. The author was logging under the supervision of Professor Henning Dypvik, and with the assistance of Abdus Samad Azad.

A total number of 26 samples were taken from each section. There were no fixed intervals between the samples, but the sampling aimed at getting representative lithologies and facies, and consequently sampling intervals were dependent on changes in facies, i.e. denser sampling in parts where there were rapid changes of depositional style. The samples

were named according to a fixed style to ensure secure sample identification, referring to area, section number, sample number and year of sampling (Fig. 6). In addition photo documentation was prepared and measurements of structures present ripples were taken (length, strike and dip etc.).



**Figure 6.** Schematic description of the sample naming.

## 4.2 Mineralogical and petrographical analysis

The mineralogical and petrographical analysis has been performed using both thin sections and X-ray diffraction (XRD) analysis. The matrix analyses were in. Samples which contained only clasts were omitted.

Sedimentary facies has been identified using field logs, pictures and thin sections to determine lithology, texture and structures. Each facies have been grouped into different facies associations.

### 4.2.1 Thin sections

Thin sections were prepared by “Anszlif” company (Krakow, Poland). Rock samples were polished down to 30 µm thickness in two stages: 1 – prepolishing on chromium oxide  $(\text{NH}_4)_2\text{Cr}_2\text{O}_7$ , 2 – then polishing on diamond suspension, the Struers brand. The final products were glued to a 2,8 cm x 4,6 cm glass slide.

21 thin sections were selected for study under a petrographic microscope. The microscopic observations were done in plain polarized and cross polarized light. Thin sections were studied (in addition to getting petrological introduction) to support data from logging, to improve a lithologic column, to get to know relations between beddings, facies, facies associations etc. Different attributes were chosen to describe origin and transport of sediments:

- Average grain size,
- Maximum grain size,
- Sorting,
- Roundness,

- Grain contact ,
- Compaction etc.

All results from thin sections investigation are summarized in Appendix 4.

In order to get the mineral content point counting has been performed using a Swift automatic counter (see Appendix 3). An average number of counts were around 400. In order to get an overall impression of the petrographic properties of the crater's infill succession a representative selection of 18 thin sections were picked out (Tab. 1).

**Table 1.** Analysed samples from the Ritland impact structure. Mineralogical, petrographical and sedimentological analyses have been performed (✓), and in some few cases only qualitative observations (✗).

Sample name	Point counting	XRD	Sample name	Point counting	XRD
RITF-1-1-09	✓	✓	RITF-3-2-09	✓	✓
RITF-1-2-09	✓	✓	RITF-3-3-09	✓	✓
RITF-1-3-09	✗	✓	RITF-3-4-09	✗	✓
RITF-1-4-09	✓	✓	RITF-3-5-09	✗	✓
RITF-1-5-09	✓	✓	RITF-3-6-09	✓	✓
RITF-1-6-09	✓	✓	RITF-4-1-09	✓	✓
RITF-1-7-09	✗	✓	RITF-4-2-09	✗	✓
RITF-1-8-09	✗	✓	RITF-4-3-09	✓	✓
RITF-1A-1-09	✓	✓	RITF-4-4-09	✗	✓
RITF-1A-2-09	✓	✓	RITF-4-5-09	✓	✓
RITF-1A-3-09	✓	✓	RITF-4-6-09	✓	✓
RITF-2-1-09	✓	✓	RITF-4-7-09	✓	✓
RITF-3-1-09	✗	✓	RITF-4-8-09	✓	✓

#### 4.2.2 XRD analysis

X-ray diffraction (XRD) provides an estimation of the mineral composition of a bulk sample based on the crystal structure of individual components. The presence of particular components is detected through a visual recognition of characteristic peak positions (Bolewski and Żabiński eds., 1988). XRD determines particular phases in a bulk, in addition, a special software (e.g. Macdiff) can estimate percentage of individual phases. Macdiff can serve well for the preliminary quantitative analysis, however, the software's database is too small to give precise results in qualitative analysis.

The quantitative analysis by X-ray diffraction is complicated, and have to be determined as semi-quantitative. For the bulk analysis the quantitative analysis was conducted by using



the maximum intensities for the respective mineral reflections. The targeted peaks are shown in Table 2.

**Table 2.** D-values used in XRD analysis.

Mineral	d-value (Å)	Range
Stilpnomelane	12,1	0,2
Biotite + Muscovite	10	0,2
Chlorite	7	0,1
Quartz	4,26	0,02
K-feldspar	3,24	0,01
Plagioclase	3,19	0,012
Calcite	3,03	0,02
Actinolite	2,96	0,01
Dolomite	2,89	0,01
Siderite	2,79	0,03
Pyrite	2,71	0,03

In order to get a detailed knowledge of the mineralogical composition of the 26 bulk samples were analyzed by XRD using a Philips X'Pert MPD, at the University of Oslo. XRD-analyses have been carried out to get both qualitative and semi-quantitative results. All results from the XRD analyses are summarized in Appendix 2

The samples were hand crushed by mortar and pestle, and powdered for 5 minutes using a “a steel slinging mill”. The samples were packed into XRD sample holders to retain random orientation.

The XRD data were processed digitally using MacDiff software (version 4.2.5) to establish a baseline of intensity, correct peak positions (relative to quartz), calculate peak intensities and peak areas, and to identified different minerals (Petschick, 2001).

#### 4.2.3 Lidar survey

The well exposed sediments at the Svodene Hill were examined by Lidar acquisition – laser scanning (Fig. 7 and 8) (Bellian et al., 2005; Buckley, 2010). Lidar survey was executed by Simon Buckley from the Centre for Integrated Petroleum Reaserch (CIPR, Univ. of Bergen) from 12<sup>th</sup> to 13<sup>th</sup> August 2009. The purpose of the acquisition of detailed outcrop data was mapping of sedimentary and structural features. A Lidar scanner Riegl LMS Z420 (Fig. 7) was applied with a set-up as described in Buckley et al. (2008a). During processing and

analysis both RiSCAN Pro (ver 1.5.1b17) and Lime (ver 0.3) software were applied (Buckley, 2009).



**Figure 7.** A Riegl LMS-Z420i, showing mounted camera, GPS antenna, power supply and laptop interface. The total setup weighs around 60 kg, and is moderately portable in the field (the figure description from Buckley et al.2008a).

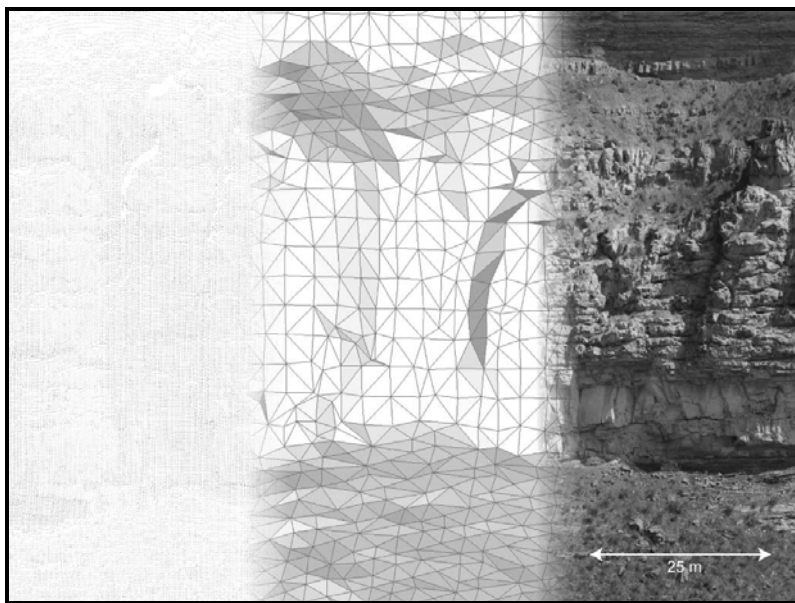
Laser scanning is an active measurement technique based on the time that takes for a single laser beam to travel a distance between the instrument and a surface (time-of-flight). This information is sufficient to calculate distances between the sensor and a topographic surface. The scanned surface represents a cloud of high resolution 3D data points (Fig. 8, left). This cloud is formed by rapid horizontal and vertical deflection of the laser beam (Buckley, 2010). During processing the unorganized and noisy 3D data points is transform into a 2-manifold triangular mesh of a flat plane pointed towards the target surface implied by the LiDAR points (Fig. 8, center) (Sahillioglu, 2009). Digital photographs<sup>5</sup> are additionally required to interpret features, which cannot be identified in the point cloud. These provide colour and texture information which are used later in the processing (Fig. 8, right) (Buckley, 2010).

In the point clouds a large amount of vegetation is presence, disturbing the obervations of the 3D model. Presence of vegetation can degrade meshing and texturing results, consequently vegetated areas have been removed from the final results (Buckley, 2010). Because lidar operates in the visible and near-infrared wavelenghts, its signal is affected by

---

<sup>5</sup> in this case the Nikon D200 camera and the Nikon 18-55 mm lens were used

atmospheric conditions (Mather, 2004). Another difficulties for a Lidar acquisition is water on a rock surface. The Lidar-derived image appears darker in the place where water was sipping (Fig. 37 and 38), as the water reflect a laser beam.



**Figure 8.** Detailed view of point cloud (left), triangle mesh (centre) and textured outcrop (right) (from Buckley et al., 2008a). Such small area like in the figure, contains over 100 000 points in the point cloud, but after processing a few thousand triangles has left. Finally, the texture, derived from photos taken by camera, is put on a triangular mesh of a flat planes.

## **5. Sedimentological description**

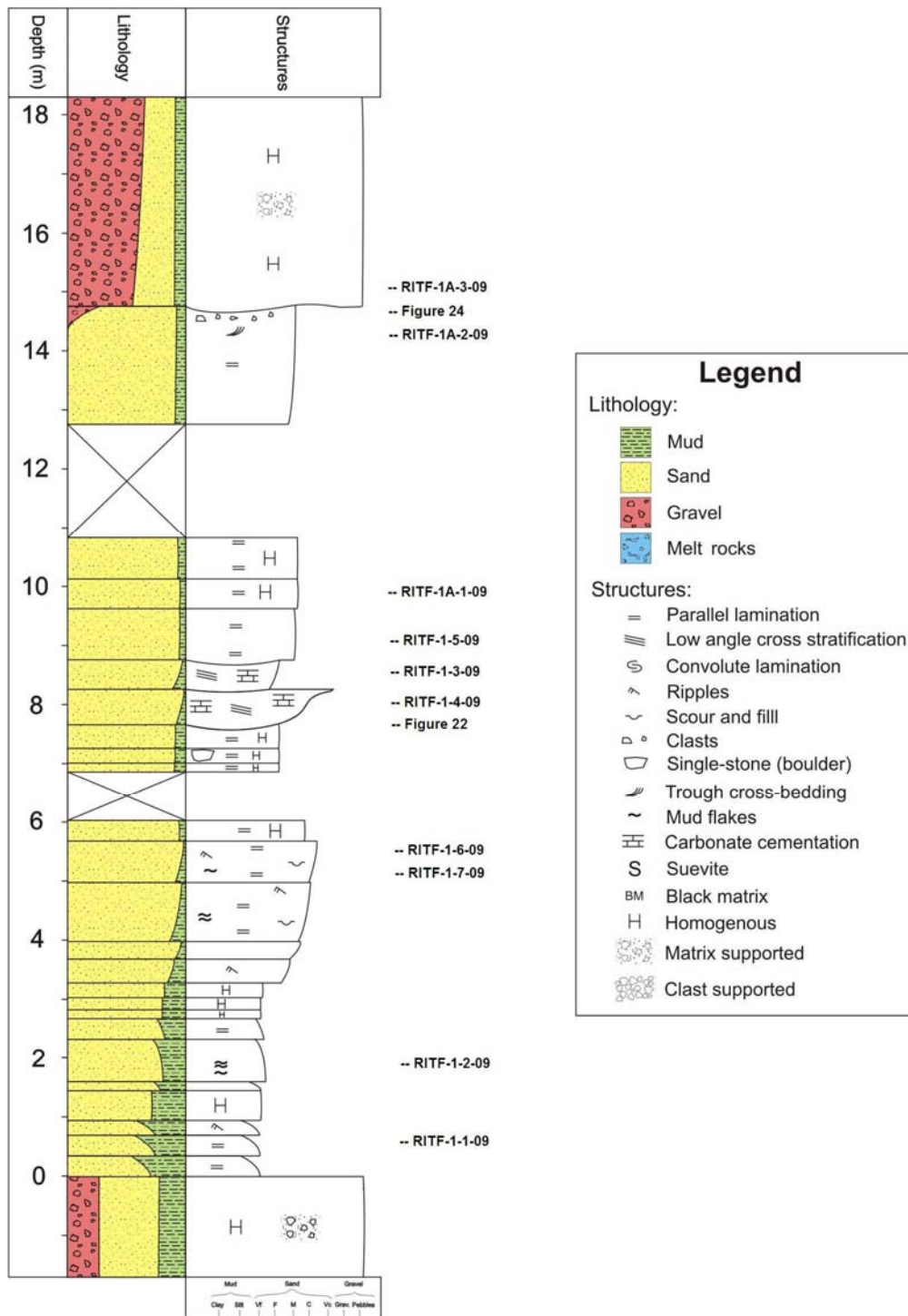
The master thesis is based mainly on log description, supported by Lidar analyses, mineralogical and petrographical analyses. During field work three sections were logged in details at the Svodene hill.

### **5.1 Sedimentological logs**

The Svodene hill provides very good three dimensional exposures of the sedimentary rocks filling the southern part of the impact structure. Three sections (Fig. 10, 11 and 12) were picked out in order to obtain a good understanding of the post-impact sediments filling in the area (Fig. 9). The log RITF-4 (Fig. 12) begins from the suevite and follows sediments up to conglomerate units interfering with sandstones. The next logs RITF-1 (Fig. 10) and RITF-3 (Fig. 11) are located on steep west slope of the Svodene hill. Finally, the three sections have been associated together, showing the stratigraphic relation between logs. It helped to compose the crater infill (Fig. 13).

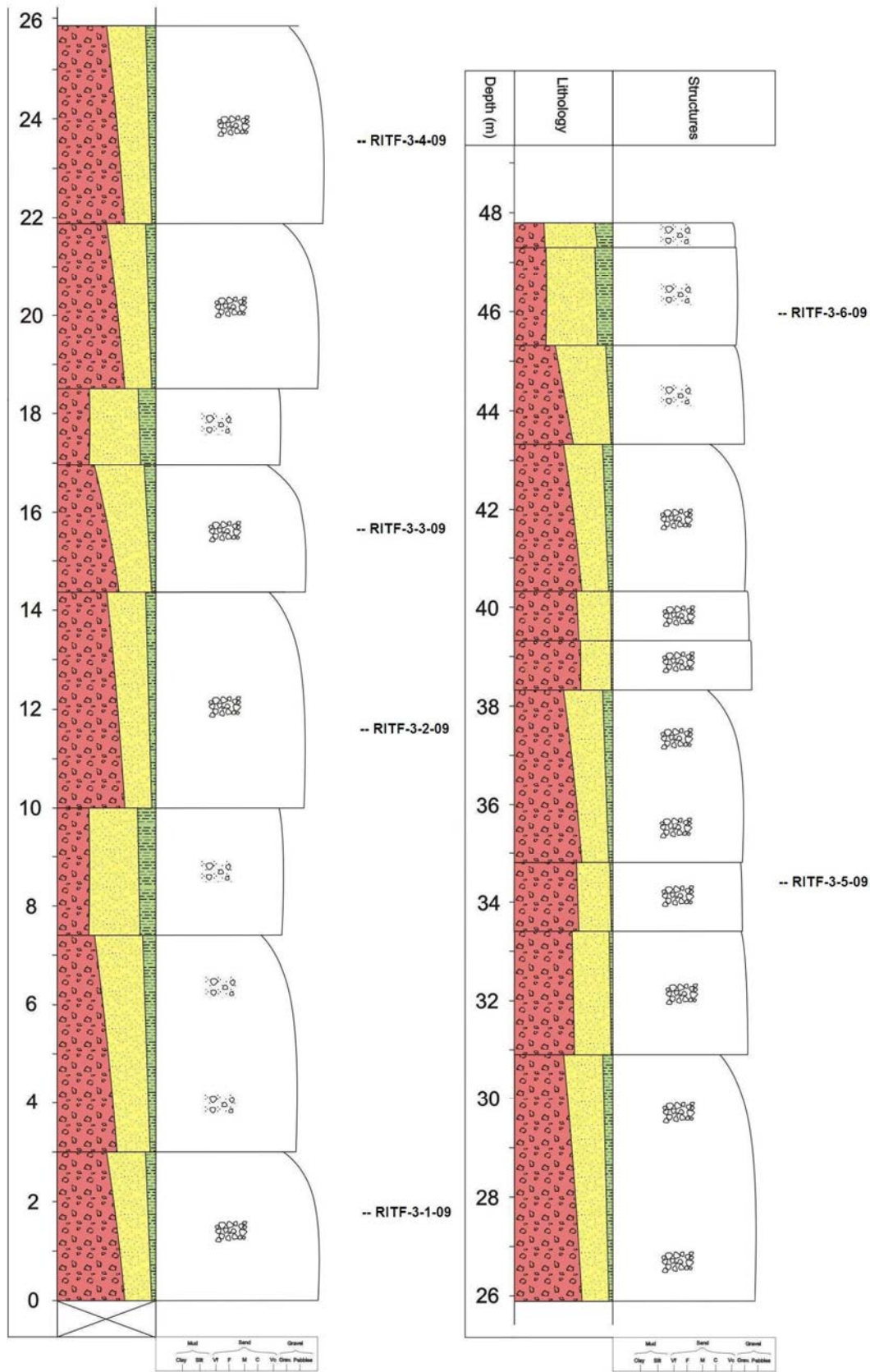


**Figure 9.** Overview of Ritland structure (the southern part), with approximate location of scanned outcrop sections (red lines: Ritland\_N, Ritland\_W and Ritland\_E) and scanner positions (yellow dots). In this thesis Lidar images from only one outcrop (Ritland\_W) will be described. Three sections (yellow squares) were picked out in the Svodene hill. The melt rocks (red square) are exposed within a small area, central in the structure.

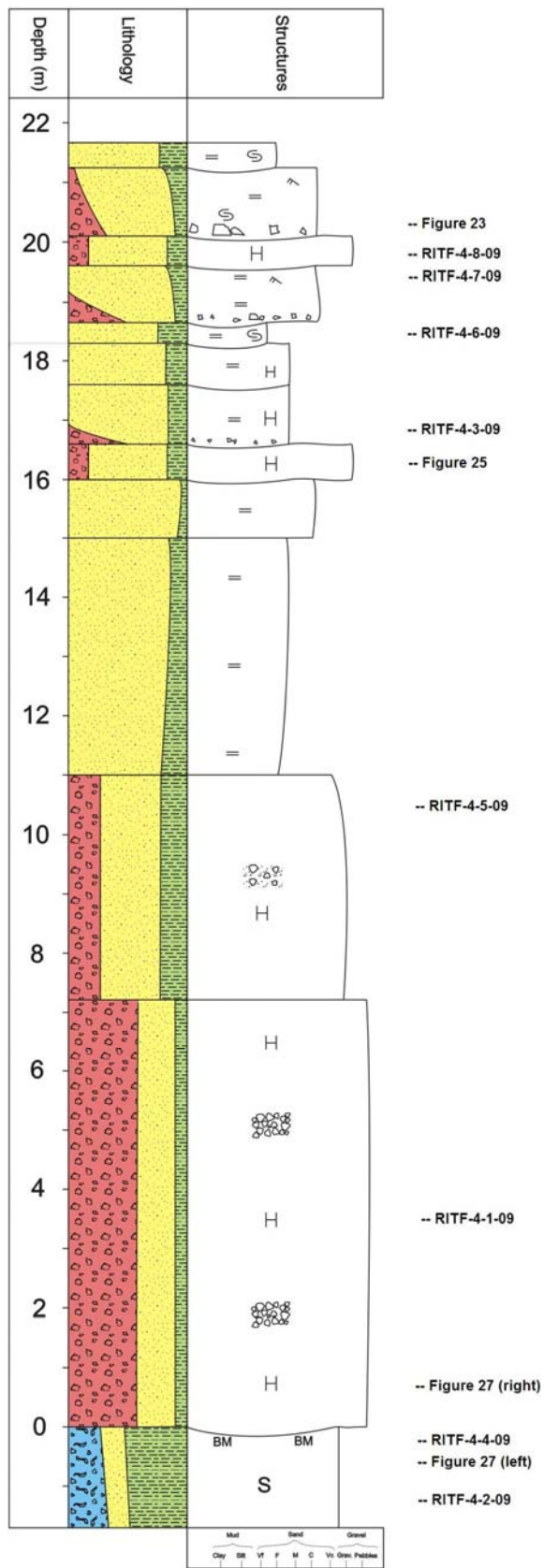


**Figure 10.** The detailed log RITF-1 from the lowermost section of the Svodene hill (location shown in Fig. 9), with the sample and photo names (the level they were taken at). This section consists of mostly sandstone units.

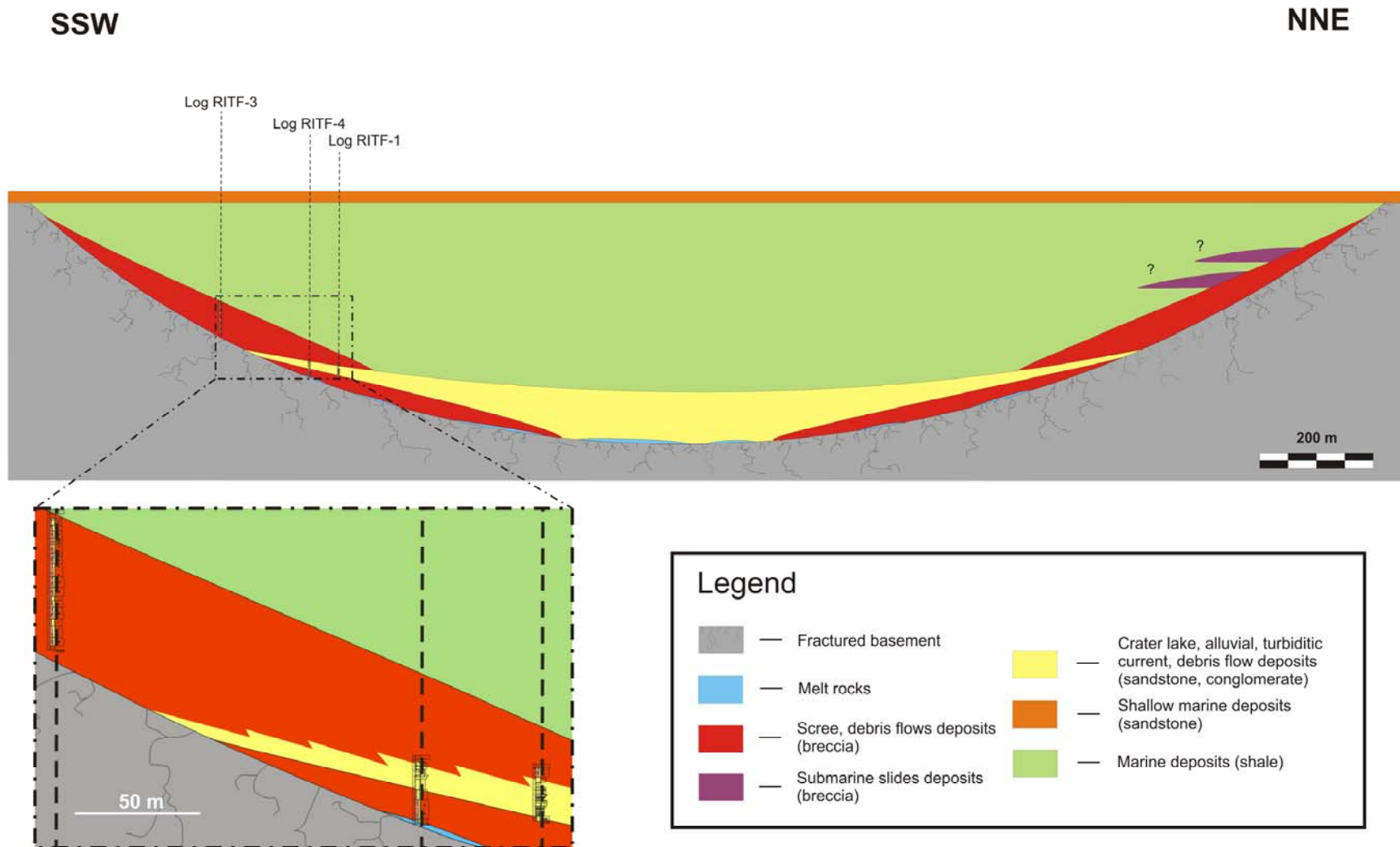




**Figure 11.** The detailed log RITF-3 (location shown in Fig. 9) with the sample and photo names (the level they were taken at). This section consists of only breccias. The section has been split up two logs.



**Figure 12.** The detailed log RITF-4 which follows sediments across the suevite and conglomerate, the western side of the Svodene Hill (Fig. 9), with the sample and photo names (the level they were taken at).



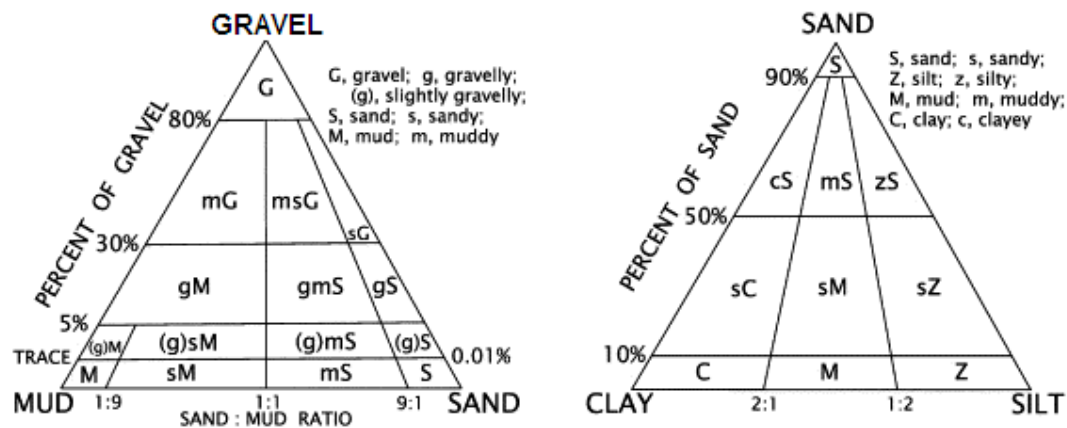
**Figure 13.** The figure shows the crater infill, based on the stratigraphical relation between the three sections. The three logs has been related together using data from: the GPS (horizontal position), the Lidar instrument (vertical position) and other methods used in the field. The suevite “patches” (blue) are covered by breccia at the base (red). Subsequently the crater center is with sandstone (yellow), which interfingering with sedimentary breccia (red) at crater margins. Everything is covered by shale (green).



## 5.2 Facies description

Facies is a distinctive rock unit that forms under certain conditions of sedimentations, e.g. a sedimentation on the beach (Reading, 1996). Facies has been identified using field logs, pictures and thin sections to determine lithology, texture and structures. Finally, particular facies have been grouped into different facies associations, representing certain depositional environments (as described in Chapter 6.3) (Fig. 15). Boundaries between facies associations were distinguished by abrupt change in deposition environment (e.g. the boundary between the conglomerate – a mass flow, and a laminated sandstone – static conditions in a relatively deep-water reservoir; Fig. 18C and 25).

The clastic sedimentary rocks has been classified on the basis of their grain size, using the Wentworth grain-size scale (Wentworth, 1922). The siltstone is a rock with the grain size  $\frac{1}{256} - \frac{1}{16}$  mm, and the sandstone with the grains size  $\frac{1}{16} - 2$  mm. In addition the sedimentary rocks with particles bigger then 2 mm ( $>10\%$  in the rock) are classified as conglomerate or breccia, according to sediment facies recognized in the deep sea (modified from Stow, 1985; Pickering and Stow et al., 1986).



**Figure 14.** Triangular diagrams of: (left): gravel, sand and mud; (right): sand, silt and clay (from Folk, 1974).

Several rock types has been recognized in the crater infill. The the base for the classification of sediments were the triangular diagrams (Folk, 1974) :

- Breccia – is a rock composed of angular to subangular clasts ( $>20\%$  the volume of a rock) in a matrix. The sizes of clasts are usually larger than cobbles (64 mm – 256 mm). Depending on the amount of a matrix breccias can be subdivided into clasts supported (clasts are in distinct contact with each other, supports each other) and matrix supported (clasts are floating in matrix);

- Conglomerate – sedimentary rocks (there are matrix and grain/clast supported types) that contain a substantial fraction (at least 30 %) of gravel size (>2 mm) particles (Boggs, 2006). Clast have rounded shapes within fine-grained matrix;
- Conglomeratic sandstone – this rock contains 5-30 % gravel to sand and 90-100 % sand to mud;
- Sandstone – the sedimentary rock contains 0-1 % gravel to sand and 90-100 % sand to mud;.
- Suevite – is an allochthonous breccia, where angular rock fragments of different sizes and lithologies are floating in a fine-grained clastic matrix (French et al., 1997). Dark fragments of melted rocks (up to few centimeters) occurs in the suevite.

12 facies has been recognized (Tab. 1) by using the logs and other additional observations (thin sections, photographs etc.). These facies will be described in details in the following chapter.

**Table 1.** Summarization of sedimentary facies in all three sections from the Svodene hill.

Facies No.	Facies	Grain size	Structures	Presence in the log	Depth (m)	Figures
<i>I</i>	Conglomerate	Medium sand to cobbles	Poorly sorted, matrix supported, subrounded clasts within laminated sand-size matrix	RITF-3	18,55 – 17,00; 10,00 – 7,35;	-
				RITF-4	20,10 – 19,40; 16,60 – 16,00	18A; 18C, 23
<i>IIa</i>	Sedimentary breccia	Medium sand to boulders	Clast supported, angular clasts, some matrix (medium sand) around clasts	RITF-3	43,40 – 18,55; 17,00 – 10,00; 3,00 – 0,00	21B
<i>IIb</i>	Sedimentary breccia	Medium sand to cobbles	Matrix supported, subangular clasts, fine layering by matrix	RITF-3	45,35 – 43,40; 7,35 – 3,00	20A; 20B; 20C; 21C
				RITF-1	18,25 – 14,80; < 0,00	-
				RITF-4	11,00 – 7,20	19C?
<i>III</i>	Soft sediment deformed sandstone	Fine sand	Homogenous sandstone, convolute lamination	RITF-4	21,70 – 21,25; 18,65 – 18,30	18B
<i>IV</i>	Conglomeratic sandstone	Fine sand to pebbles	Parallel laminated sandstone, with decreasing number of clasts towards the top, around clasts presence of sediment deformation, ripples	RITF-4	21,25 – 20,10; 19,40 – 18,65; 17,65 – 16,60	18A
<i>V</i>	Massive sandstone	Fine sand to medium sand	Parallel laminated sandstone	RITF-4	18,30 – 17,65; 16,00 – 11,00	19A
				RITF-1	14,80 – 8,80; 7,70 – 5,70	16C
<i>VI</i>	Low angle cross-stratified sandstone	Fine sand	Carbonate cemented sandstone, low angle cross-stratification (~9°)	RITF-1	8,80 – 7,70	16B, 22
<i>VII</i>	Parallel-bedded sandstone	Silt to medium sand	The alternation of parallel laminated sandstone: from coarsening upwards to fining upwards sequences, mudflakes (1-3 mm thickness), ripples, scour and fill	RITF-1	5,70 – 0,00	16D, 17A, 17B, 17C
<i>VIII</i>	Breccia at the base	Coarse sand to boulders	Clast supported, angular to subangular clasts	RITF-4	7,20 – 0,00	19C
<i>IX</i>	Suevite	Very fine sand to pebbles	Melted particles, angular lithic fragments (pebble-size), within matrix	RITF-4	< 0,00	19D, 19C

Facies description:

- I*      **Conglomerate** – the facies occur in the log RITF-4 (Fig. 12), two conglomerate units (levels in Tab. 1) and two units in the log RITF-3 (Tab. 1 and Fig. 11) with bright colour of a matrix. The clasts floating in a sandy matrix have more rounded shape than these in the RITF-3. The conglomerate beds have a deposition inclination of 20-22 degrees. The conglomerate units interfinger and have visible erosional contact with surrounding sandstone units (Fig. 18A and 23). The facies forms channel-like structures (few meters wide, with thickness up to 60 cm), from W to E along the strike of the beds (Fig. 26). Large angular clasts (up to 30 cm) sit on the top of these conglomerates, stuck together (Fig. 23). The clasts are granite-gneissic rock fragments. The clasts are usually medium- to coarse-foliated and largely recrystallized, consist of quartz, feldspar and minor amount of micas, chlorite;
- IIa*    **Sedimentary breccia (polymictic, homogenous)** – twelve intervals have been recognized in the log RITF-3 (Tab. 1 and Fig. 11) as clasts supported breccia with angular clast in size up to boulders (some of them have more than 2 m). The clasts are densely packed. The breccia units commonly are fining upwards, larger clasts are at the base of unit (Fig. 20A), no more internal structures have been seen. The clasts are granite-gneissic rock fragments and exhibit jigsaw puzzle patterns. The clasts consist of quartz, feldspar and minor amount of micas, chlorite (Fig. 20C). The breccias form wedge-shape beds interfinger with sandstone (Fig. 13). The breccia beds have depositional inclination up to 25 degrees, gradually decreasing to the crater center;
- IIb*    **Sedimentary breccia (polymictic, homogenous)** – matrix-supported breccia with clast-size up to 70 cm. A larger amount of matrix (Fig. 21B). The breccias form wedge-shape beds interfinger with sandstone (Fig. 13). The breccia beds have depositional inclination up to 25 degrees, gradually decreasing to the crater center. Lamination within a matrix have been recognized (Fig. 43). The matrix has a grey to pink colour (Fig. 42 and 43). Two intervals of this facies have been recognized in the log RITF-3 (Tab. 1 and Fig. 11), one interval in the log RITF-1 (Fig. 10) in a contact with a sandstone and the last interval in the log RITF-4 (Fig. 12) between a sandstone and the breccia at the base. The clasts are granite-gneissic rock

fragments, and are usually medium- to coarse-foliated and largely recrystallized, consist of quartz, feldspar and minor amount of micas, chlorite;

- III Soft sediment deformed sandstone** – fine grained laminated sandstone (laminae from 0,6 cm to 0,8 cm in thickness) where horizons with convolute lamination occurs (Fig. 18B). There are two 0,5 m thick intervals of this sandstone in the log RITF-4 (Tab. 1 and Fig. 12) where the erosional surfaces occurs, at the base and top (Fig. 18B);
- IV Conglomeratic sandstone** – this facies represents fine-grained, laminated sandstone (laminae thickness from 0,6 cm to 0,9 cm) with some clasts (up to pebble-size) at the bottom of units (Fig. 23, a conglomeratic sandstone overly the conglomerate unit). The clasts are granite/gneissic rock fragments. The conglomeratic sandstone occurs in the log RITF-4 (Fig. 12). There are three visible intervals (levels in Tab. 1), which cover the conglomerates (facies *I*). The conglomeratic sandstone beds have depositional inclination of 20 degrees, gradually decreasing to the structure center. The sheet like beds interfinger with sandstone located below. Erosional base is characteristic for this facies. Observed sedimentary structures include convolute lamination and ripples (Fig. 23; directions of transport – Fig. 26).
- V Massive sandstone** – the massive sandstone units with faint lamination (Fig. 19A). Grain-size is from fine sand to medium sand. This facies occurs in the log RITF-4 (Tab. 1 and Fig. 12) and RITF-1 (Tab. 1 and Fig. 10). It is hard to see any other structure;
- VI Low angle cross-stratified sandstone** – this facies is fine-grained sandstone which contains carbonate cement. Small-scale trough cross-bedding occurs in this facies (Fig. 16B and 22). Erosional surfaces are visible at the bottom and top of units (Fig. 22). This facies is located in section one, visible in the log RITF-1 (Tab. 1 and Fig. 10). The facies has thickness of 1 m, and the unit pinch-out to the crater rim (Fig. 22);
- VII Parallel-bedded sandstone** – this facies has been recognized in the RITF-1 (Tab. 1 and Fig. 10) as very well laminated sandstone (laminae thickness from 0,2 cm to 0,8 cm; Fig. 17C). The sandstone beds have a deposition inclination of 10-15 degrees. Grain-size is from silt to medium sand. We can differentiated two internal units: one is coarsening upwards (5,70 m – 2,65 m), from silt to very fine grain-size, and the other is fining upwards (2,65 m

– 0,00 m), fine sand to medium sand. In both occur ripples, scour and fill (directions of flow – Fig. 26) and mud-flakes layers (1-3 mm thickness).

**VIII Breccia at the base** – facies represents clasts-supported breccia. The breccias form wedge-shape beds interfinger with the melt rocks (Fig. 27). The breccia beds have depositional inclination much smaller than the sedimentary breccias (*Ila* and *Ilb*) up to 10-12 degrees, gradually decreasing to the crater center. The sizes of the largest clasts are smaller than the largest clasts in breccias of facies *Ila*, and does not exceed 50 cm. The clasts have angular to subangular shapes. The clasts are of the same lithologies as the basement gneisses (Riis et al., 2009). They are usually medium- to coarse-foliated and largely recrystallized, consist of quartz, feldspar and minor amount of micas, chlorite. The clasts exhibit jigsaw puzzle patterns (Fig. 19C). There is very little amount of matrix (dark colour) between clasts (less than 15%). This facies occurs in the log RITF-4 (Fig. 12) where it overlies the suevitic rocks;

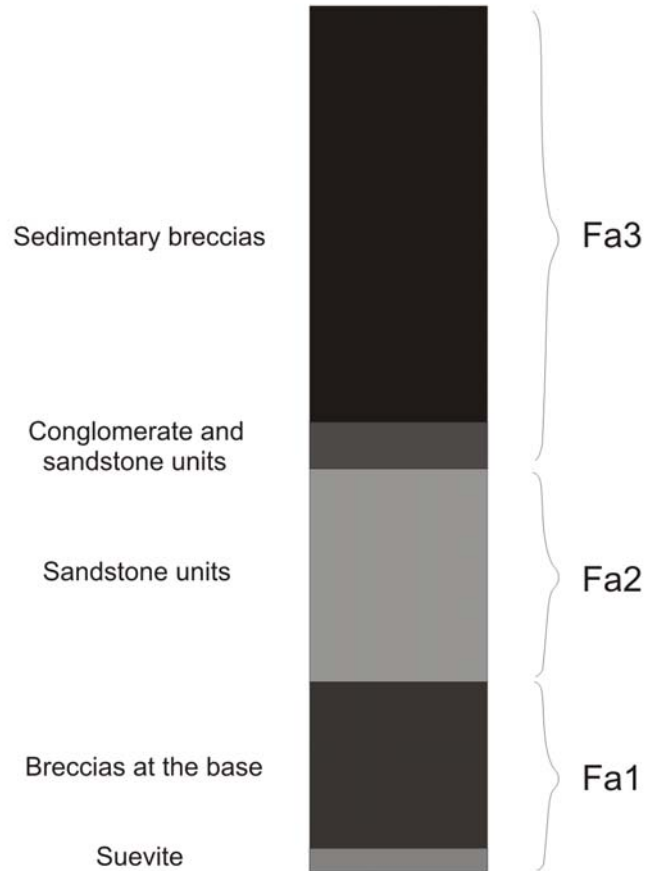
**IX Suevite** – occurs in the log RITF-4 (Tab. 1 and Fig. 12). This facies follows on top of crushed basement, but the basement contact has so far not been located. The melt rocks form lens-shape beds. The suevites (melt rocks) are dark grey to black and fine-grained. Characteristical by twisted and elongated melt fragments and angular clasts occur within the very fine-grained matrix (Fig. 19D). The melt-bearing impactites are exposed within a small area, central in the structure (Fig. 9). Within this area the outcrops indicate a rather thin (few meters), but at least for some distance (less than 200 meters), continuous unit (Kalleson, 2010). At the top of this facies there is a thin layer of darker material with black matrix. The suevite is eroded at the contact with the overlying breccias (Fig. 27, right).

### 5.3 Facies associations

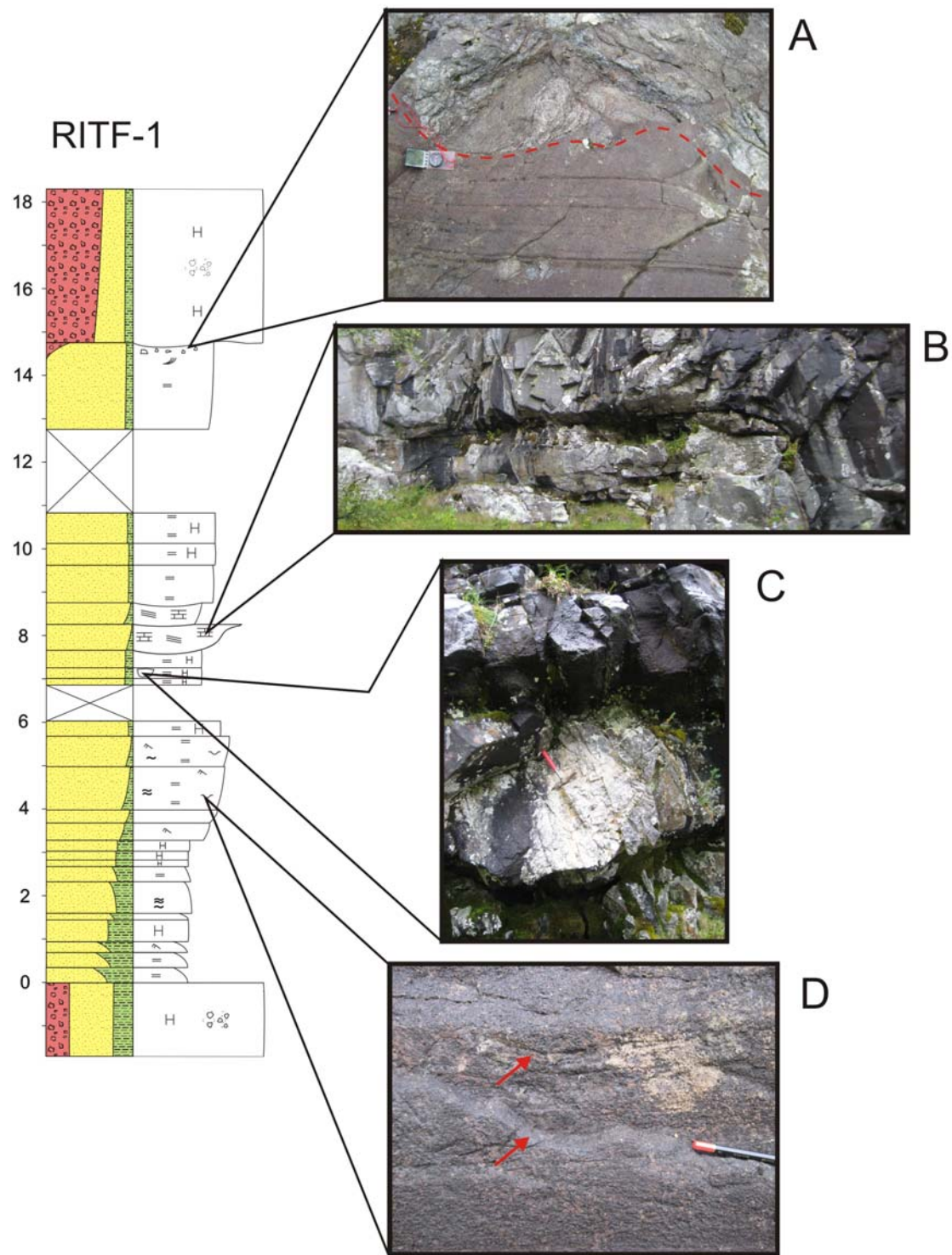
Facies which are environmentally related have been grouped into facies associations. The relation between facies associations, as well as facies themselves, will help in building depositional models. The subdivisions in facies associations are based on stratigraphical position (Fig. 15).

- **Facies association 1** – Sedimentary breccia (*Ila*), Sedimentary breccia (*Ilb*), conglomerate (*I*), Soft sediment deformed sandstone (*III*), Conglomeratic sandstone (*IV*);

- **Facies association 2** – Massive sandstone (V), Low angle or cross-stratified sandstone (VI), Parallel-bedded sandstone (VII);
- **Facies association 3** – Suevite (IX), Breccia at the base (VIII).

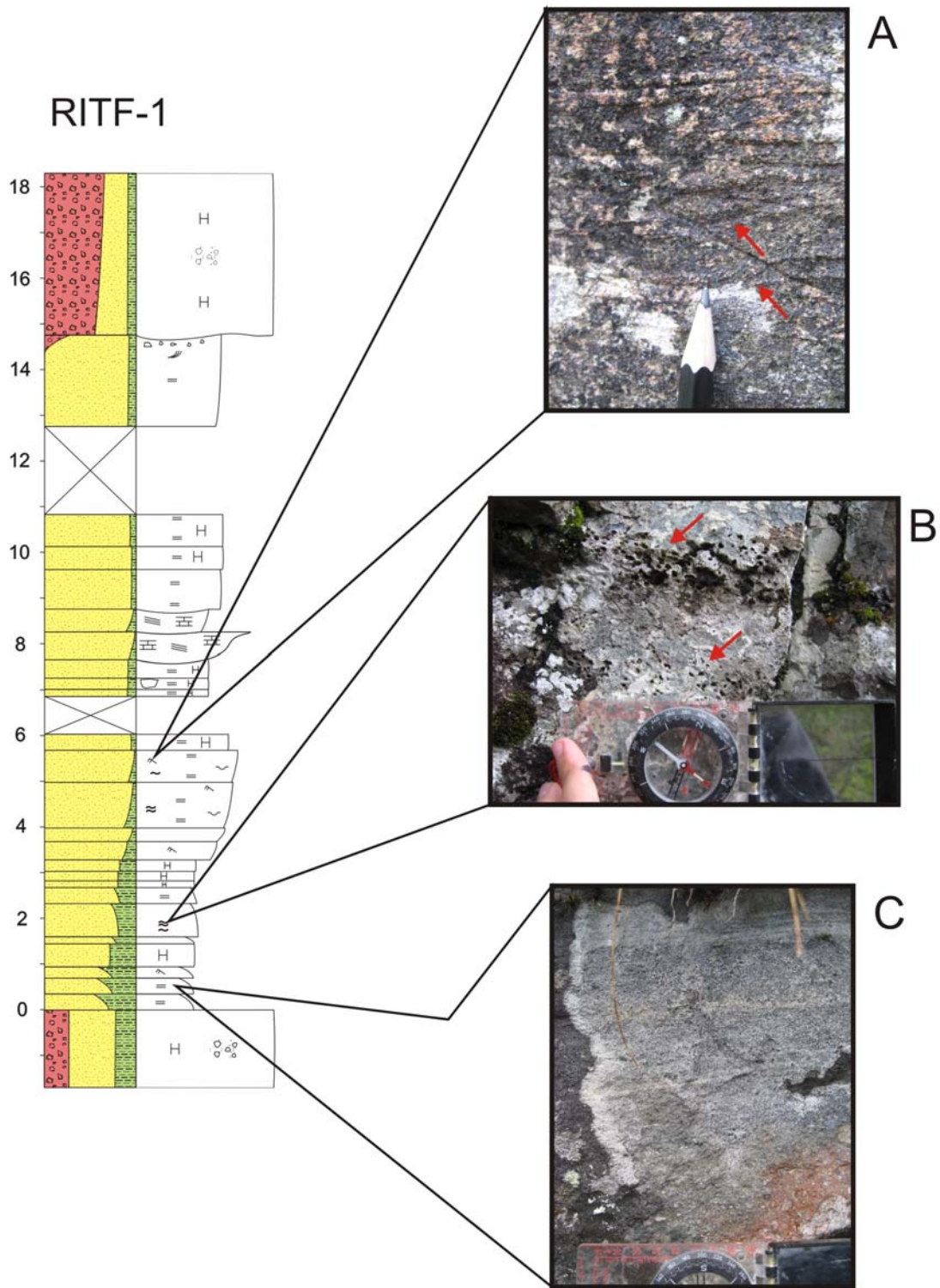


**Figure 15.** The simplified column showing the stratigraphical relation between the facies and the three facies associations of the Svodene hill. The main facies are: *suevite* (melt rocks), *breccias at the base*, *sandstone units* (parallel-bedded sandstone, low angle cross-stratified sandstone, massive sandstone), *conglomerate and sandstone units* (conglomerate, conglomeratic sandstone, soft sediment deformed sandstone), *sedimentary breccias* (interfingering beds of clast and matrix supported). The maximum stratigraphic thickness observed is almost 200 m along the rim of the crater (Riis et al., 2008).

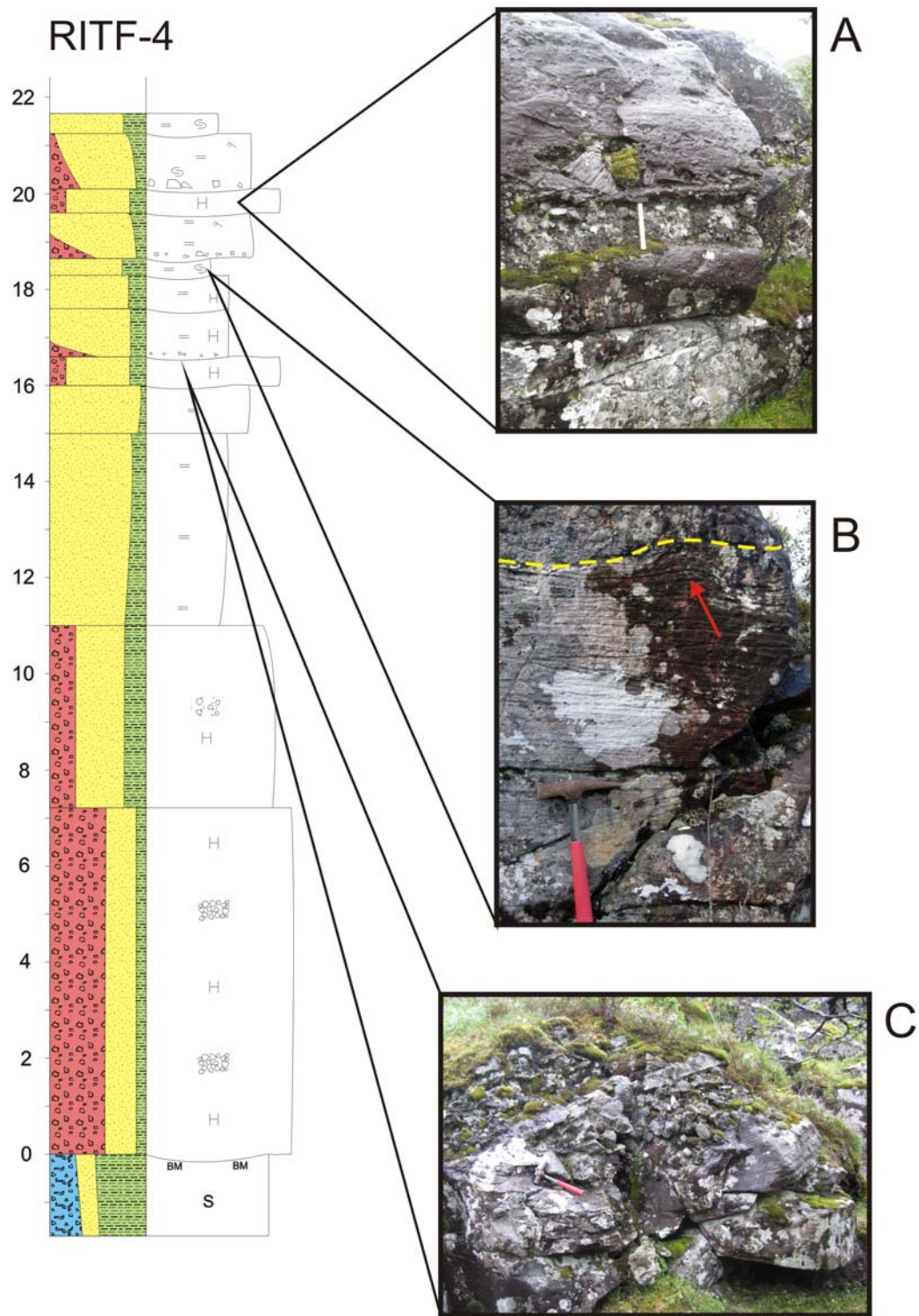


**Figure 16.** Photos from section (RITF-1). A) massive sandstone with faint lamination (below red, dash line) overly by sedimentary matrix-supported breccia (above red, dash line); B) Low angle cross-stratified sandstone within laminated sandstone, with visible basal erosion (see more in Fig. 22); C) a big clast of diameter 50 cm, in the sandstone bed; D) scour and fill structure (marked by red arrows) in coarsening-upwards sandstone unit.



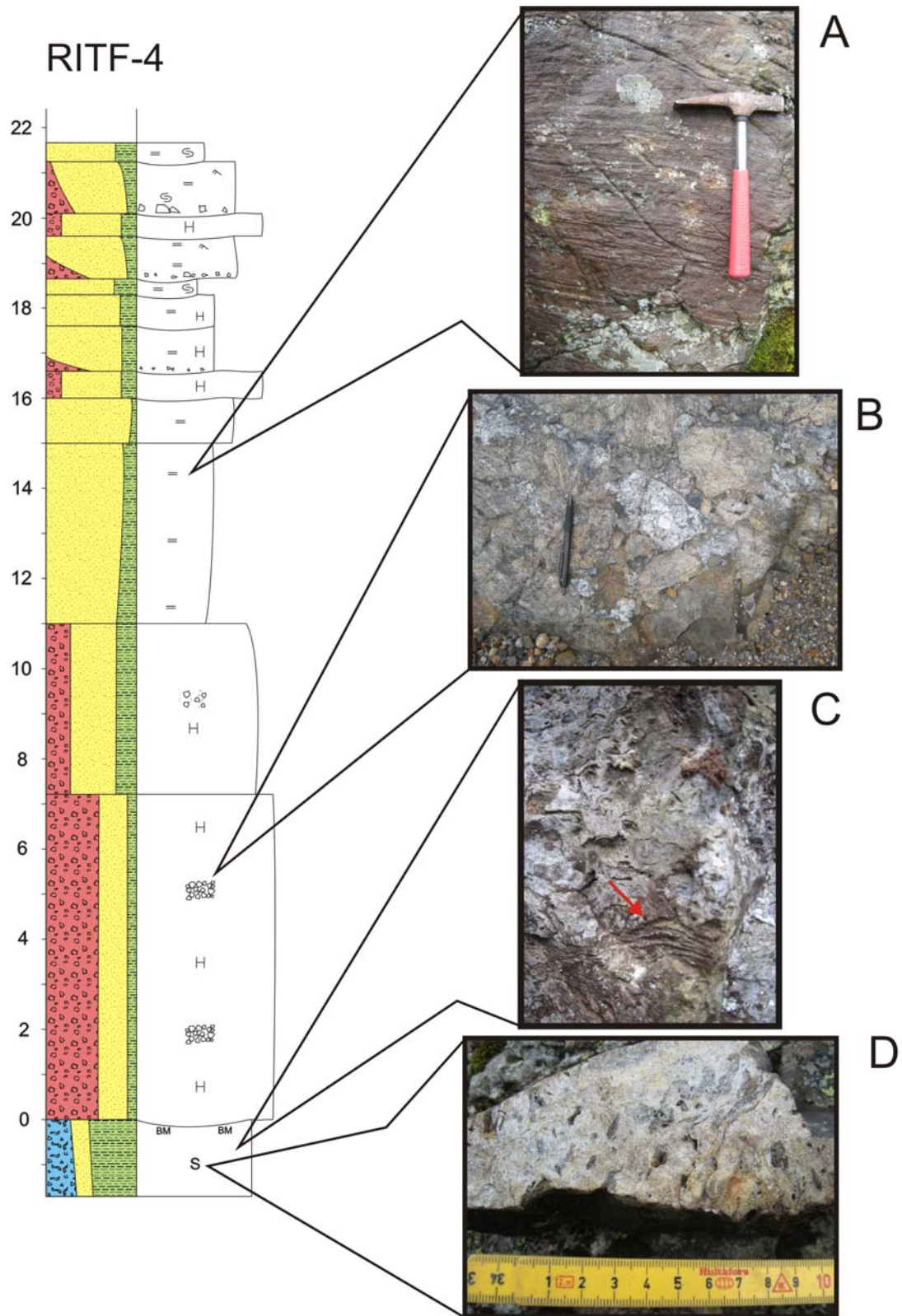


**Figure 17.** Photos from section (RITF-1). A) ripples (marked by red arrows) in a coarsening-upwards unit.; B) strings of mudflake (marked by red arrows) in fining-upwards unit; C) fining-upwards sandstone with faint parallel lamination.

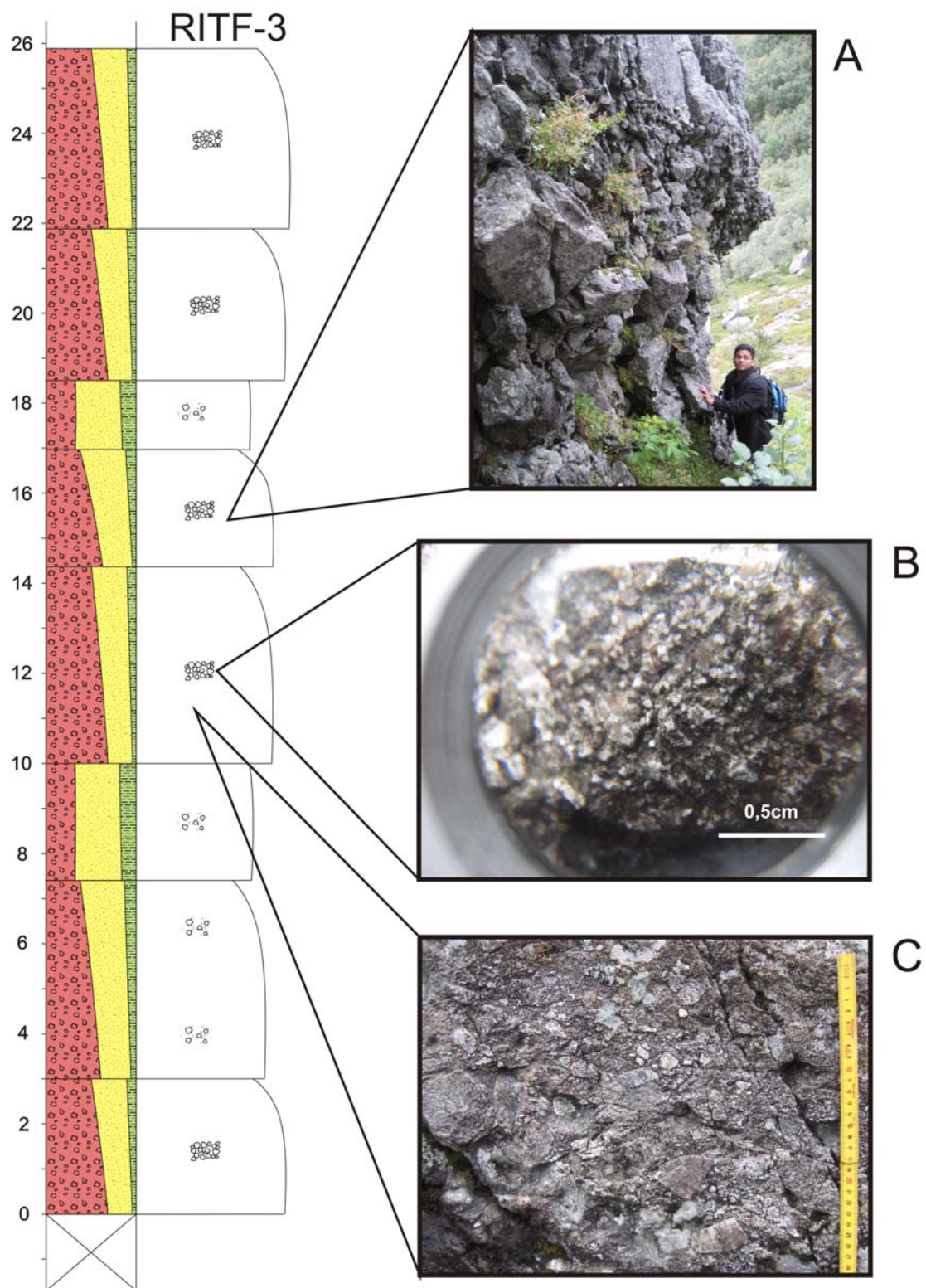


**Figure 18.** Photos from section (RITF-4). A) a conglomerate unit (hammer position) between sandstone beds. Larger clasts sit on conglomerate bed. Basal erosion visible between each unit; B) convolute lamination (red arrow) in stratified sandstone unit; the erosional surface visible (yellow dash line); C) conglomerate eroding into sandstone (see also Fig. 25).



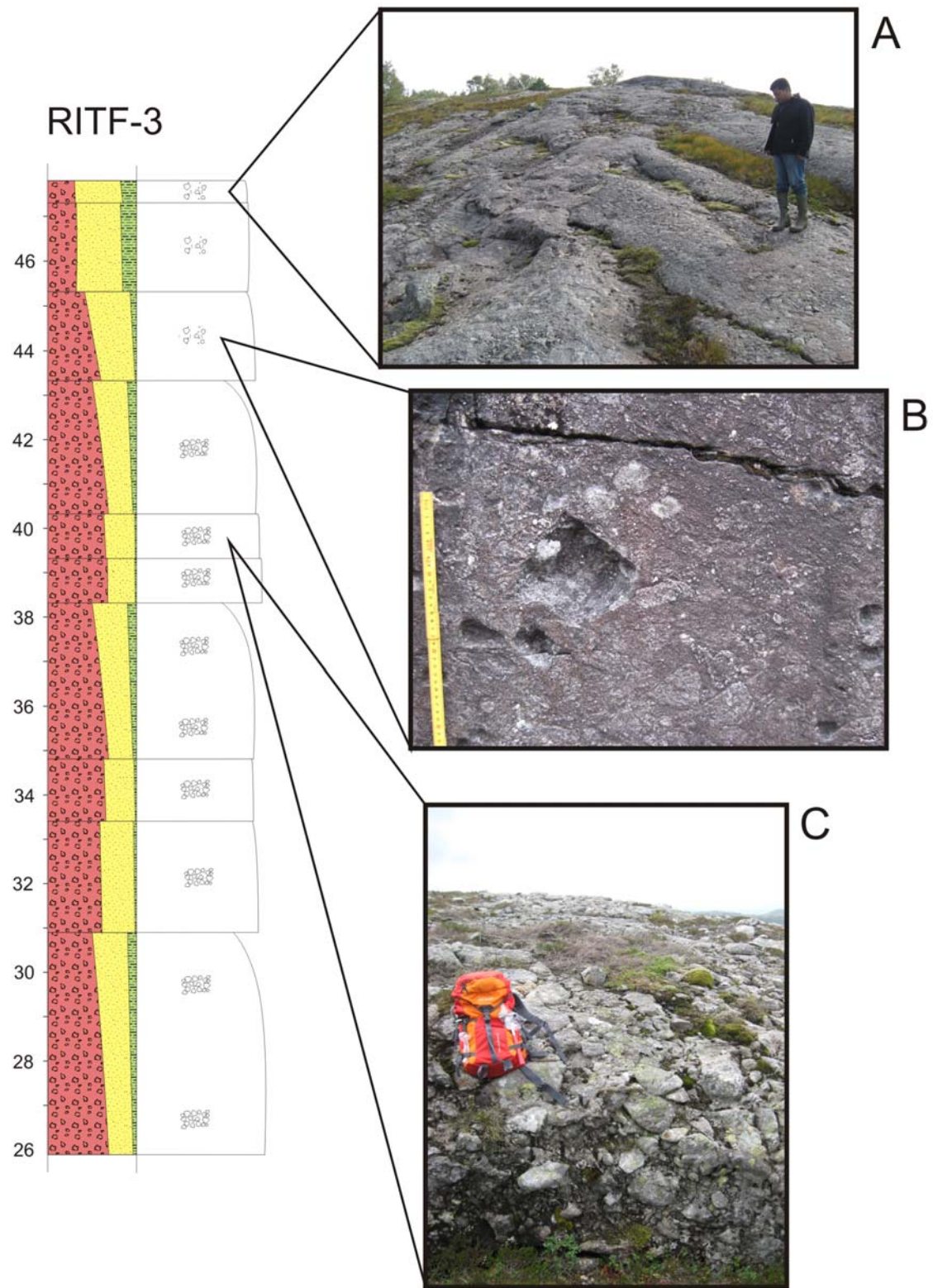


**Figure 19.** Photos from section (RITF-4). A) sandstone with visible faint lamination; B) clast supported breccia, with minor amount of matrix; C) weathered surface of suevite exhibit the stratified flow pattern (red arrow); D) the suevite with several melt slivers.

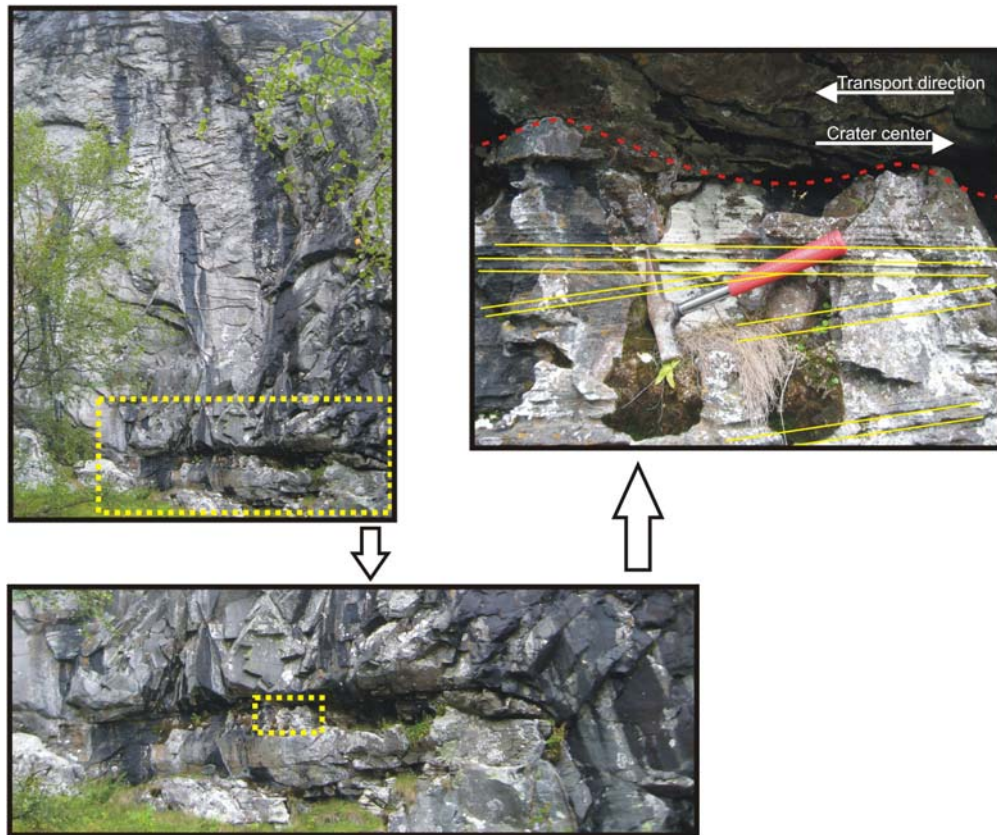


**Figure 20.** Photos of section (RITF-3). A) grain supported, coarse breccia; B) angular grains of matrix of clast supported breccia (photo taken through hand lens); C) clast supported breccia.

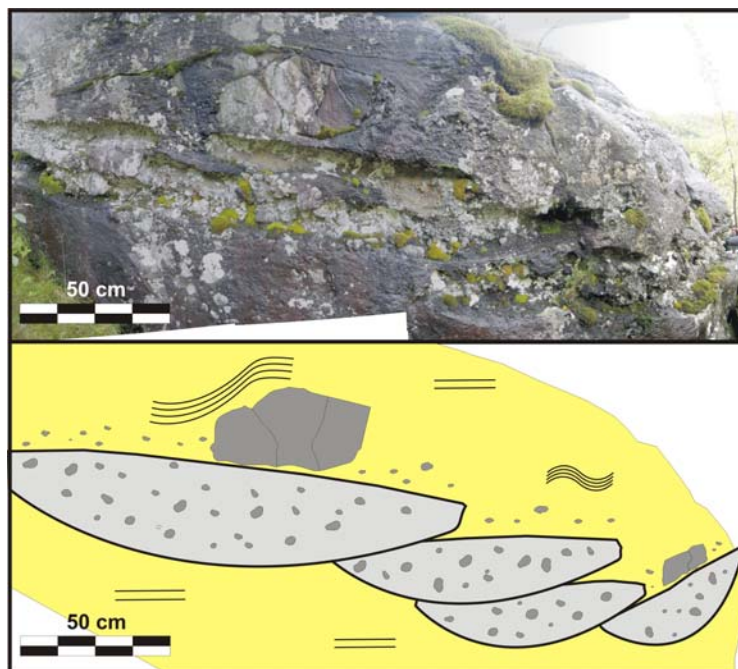




**Figure 21.** Photos of section (RITF-3). A) matrix supported breccia at the top of the Svodene hill; B) matrix supported breccia. A few clasts have been eroded from the rock face, appearing as open pits; C) clast supported breccia.



**Figure 22.** Low angle (9 degrees) cross-stratified, calcite cemented sandstone in the RITF-1 (see in Fig. 9 and 10). In upper-right photo erosional base (red, dash line), cross-stratification (yellow lines) are visible, with possible transport direction.

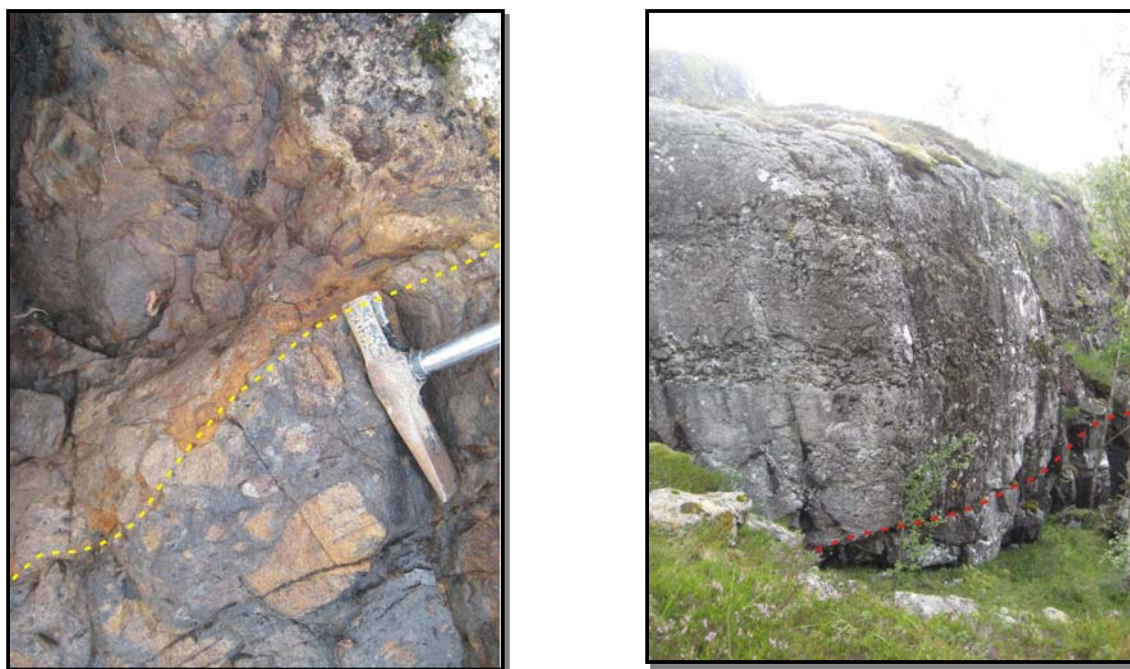


**Figure 23.** Conglomerate units in the RITF-4 (Fig. 9 and 12), between sandstone beds. Upper photo is a panoramic photo of debris flows channels, and a simplified sketch of the photo below. Larger clasts are situated on the top of conglomerates. The lamination of sandstone surrounding the conglomerate units is parallel, but also can be disturbed.



### 5.3.1 Facies association 1

This association consists of two facies which cover the crushed basement, along the crater floor: suevite and breccias at the base (Fig. 12 and 15). The suevite is exposed in the central are of the structure (Fig. 9). Within this area the outcrops indicate a rather thin (few meters), but at least for some distance (less than 200 meters), continuous unit (Kalleson, 2010). The outcrop appears as dark, greyish brown colour at weathered surface. The partly bedded pattern of melt fragments appears at weathered suevite surfaces. The clast-supported breccia appears as one thick bed (about 7 m thick in the RITF-4) where clast-size does not exceed one meter. The suevite is found in patches along the crater floor. It has been hard to localize the transition zone between suevite and overlying breccia. One site has been found where clast supported breccia directly cover melt rocks (Fig. 24, right). The top part of the melt rocks unit is eroded and reworked. In the other place, 1-2 meters below, suevite is seen mixed in the breccia (Fig. 24, left). The contact between suevite or breccia at the base and crushed basement has not been seen in the field. There are some sedimentary structures in these facies e.g. flow structure in the suevite (Fig. 19C).

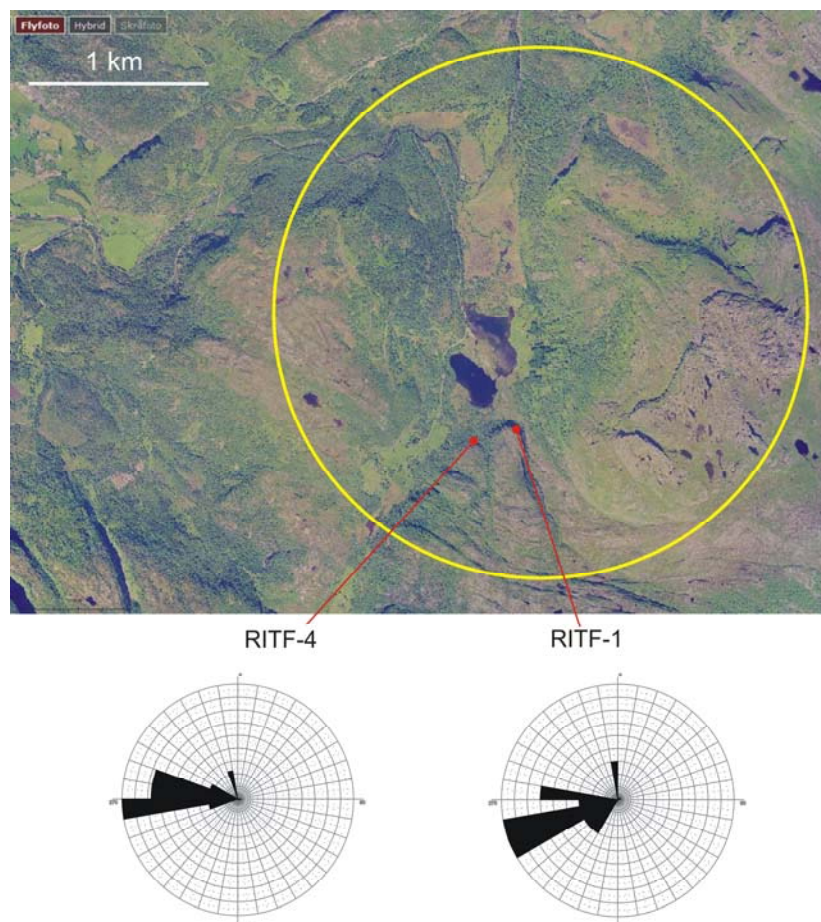


**Figure 24.** Photo (left) shows the boundary (yellow, dash line) between suevite (above yelllow line) and postimpact sediments (below yellow line). Characteristic flow structures in suevite above the hammer head, and slightly wavy shape of the boundary between the two facies are visible.. Photo (right) indicates another border (red, dash line) between suevite (below red line) and braccias (above red line). This two places on photos are separated by 1 m in stratigraphic column. The positions of photos are marked in Figure 9 and 12, in the RITF-4.

### 5.3.2 Facies association 2

The facies association includes the sandstone units in the RITF-1 and the RITF-4, with total thickness of 15 metres in both cases (Fig. 15). The massive sandstone (RITF-4: 18,30 m – 17,65 m; 16,00 m – 11,00 m and RITF-1: 14,80 m – 8,80 m; 7,70 m – 5,70 m) displays an erosional contact with breccia/conglomerate (facies association 1) above (Fig. 26 and 27). The individual beds represent thick, laminated sandstone units. Average grain-size is medium sand. A large clast (~30 cm in diameter) was found in one of the sandstone beds (RITF-1: 7,00 m – 7,35 m; see Fig. 16C). The low angle, cross-stratified sandstone (RITF-1: 8,80 m – 7,70 m) is well carbonate cemented. The carbonate cemented sandstone pinch-out to the crater rim and is increasing in thickness towards the crater center (Fig. 22). The parallel-bedded sandstone displays coarsening upwards development (RITF-1: 5,70 m – 3,30 m) and fining upwards development (RITF-1: 3,30 m – 0,00 m). The fining upwards units have grain-size from silt to very fine sand, and the coarsening upwards units have grain-size from fine sand to medium sand. Ripples (Fig. 17A), mudflakes (Fig. 17B), scour and fill (Fig. 16D) are present in both. Strikes from different sandstone beds and sedimentary structures, from facies association 1 and 2, are presented in Figure 25 and Appendix 1. The conglomerate beds and sandstone beds in the RITF-4 have strike lines along the W-S axis. The sedimentary structures in the RITF-4 have slightly different trend, with strikes from  $260^{\circ}$  to  $290^{\circ}$ . The sandstone beds in the RITF-1 have strikes from  $210^{\circ}$  to  $230^{\circ}$ . Strikes of the sedimentary structures range from  $230^{\circ}$  to  $250^{\circ}$ , and some have strike  $280^{\circ}$ - $290^{\circ}$ .





**Figure 25.** An aerial photo with crater margins marked by yellow circle. Red dots show places where measurements of strikes have been taken (26 - the total number of measurements, see Appendix 1). Below the photo rose diagrams with measurements taken from the RITF-1 and RITF-4.

### 5.3.3 Facies association 3

Thick packages of breccia, conglomerates and sandstones from the upper succession of the Svodene hill (Fig. 15). The top most part is covered by three matrix supported breccia beds (between 43,30 m and 47,85m) which overlie clast supported breccia (Fig. 11 and 21). The two conglomerate beds was recognized in the RITF-3 (18,55 m – 17,00 m; 10,00 m – 7,00 m). They are typically preluded by units of matrix supported breccia. The thickness of the breccia beds varies from one meter up to five-six metres. Beds dip (around 24 degrees) downslope towards the crater center. Matrix of the conglomerate is brighter grey than the matrix within breccia. In both matrix-supported breccia and conglomerates from the RITF-3 matrix lamination occur. A transition zone between matrix-supported breccia into sandstone is indicated in the log RITF-1 (at 14,75 m depth; Fig. 10).

Another unit in this facies association consists of intercalated conglomerate and sandstone beds (see the log RITF-4, Fig. 12). The two conglomerate beds (20,10 m – 19,40 m;

16,60 m – 16,00 m; in the RITF-4) each have thicknesses of 50 cm. The layers contain typically subangular clasts within fine-grained matrix. Matrix has very bright grey colour. Large clasts (up to 30 cm) sit on these beds (Fig. 23). Conglomerates are surrounded by conglomeratic sandstone beds (21,25 m – 20,10 m; 19,40 m – 18,65 m; 17,65 m – 16,60 m). The boundaries between them are sharp (erosive). The sandstone is finally laminated and convolute lamination occurs along the base of each bed. There are thin beds of soft sediment deformed sandstone (21,70 m – 21,25 m; 18,65 m – 18,30 m). All of these beds are characterized by erosional surfaces. This sequence ends up at place where conglomerate is dipping into the sandstone. This transition zone starts another facies association (No. 2).



**Figure 26.** Left: The breccia (above line)-sandstone (below line) contact zone marked by the author (red, dash line). This is the boundary between facies association 2 and facies association 3 (see also Fig. 10 and 15)

**Figure 27.** Right: The conglomerate (above line)-sandstone (below line) zone marked by red dash line, an erosional surface. The sandstone bed gently deeping (10 degrees) towards the crater center, and overlying conglomerate eroding into this sandstone (dip-22 degrees). This is the boundary between facies association 2 and facies association 3 (see also Fig. 12 and 15)



## 6. Mineralogical and petrographical description

In the following chapter mineralogical and petrographical descriptions are presented, based on thin section studies and bulk mineral analysis by XRD.

### 6.1 Thin section analysis

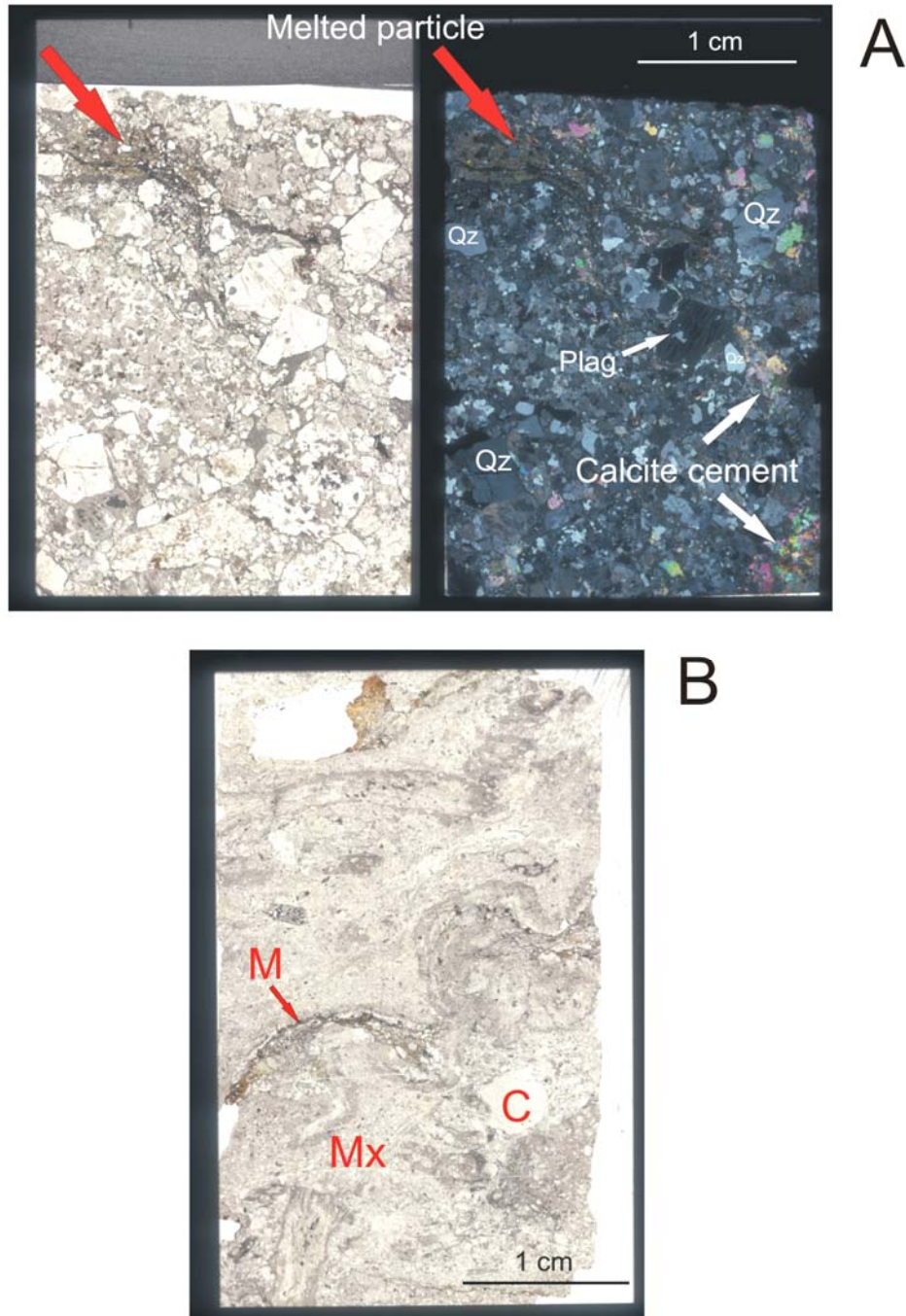
This chapter will present results from basic approaches to the quantitative analysis of thin sections: visual comparison of petrographical properties and point counting (the results from point counting of minerals are presented in Appendix 3), and their petrographical

properties. A complete sample list of thin sections with description and the results of point counting are presented in Appendix 4, and their position within the stratigraphic succession (logs) are in Figure 10, 11 and 12.

#### **6.1.1 Thin section analysis of samples from facies association 1**

Three thin sections from this facies association have been studied. The samples taken from suevite (the samples: RITF-4-2-09 and RITF-4-4-09) and are characterized by angular clasts of quartz, plagioclase and gneissic rock fragments within very fine-grained matrix (Fig. 28B). The matrix colour is light grey but from the sample from uppermost part of suevite is of black colour (*black matrix*). The brownish shard shape particles of altered melt (glassy or recrystallized particles, 0,2 mm – 0,8 mm in size) are floating within the matrix (Fig. 28B). The samples taken from the melt rocks display the flow texture. The biotite flakes and fine-grained aggregates are partially replaced by chlorite (from green to blue colour). A minor amount of calcite cement occurs in the sample (RITF-4-2-09, see Appendix 3). Some accessory minerals have been found (zirkon, epidote).

The thin section of breccia (the sample RITF-4-1-09) contains angular to subangular grains (up to 4-5 mm in size) of quartz, plagioclase and gneissic rock fragments (Fig. 28A). There is a small amount of very fine-grained matrix between clasts. A brownish melted particle has been found (Fig. 28A; the type as in the suevite). In the thin sections of the breccias significant amount of calcite cement are visible (almost 8 %). Just a few heavy minerals were observed. The metamorphic mineral occurs in several samples (chlorite, actinolite). Actinolite needles are up to 2 mm long.



**Figure 28.** Thin section photos from facies association 1: A) plane polarized light view (left) and crossed polarizers view (right) of breccia at the base (the sample RITF-4-1-09). Red arrows indicate the brownish shard shape particles (melt?); B) plane polarized light view of the sample RITF-4-2-09. The suevite consists of matrix (Mx), shard shape particles of altered melt (M), the rock fragments (C).

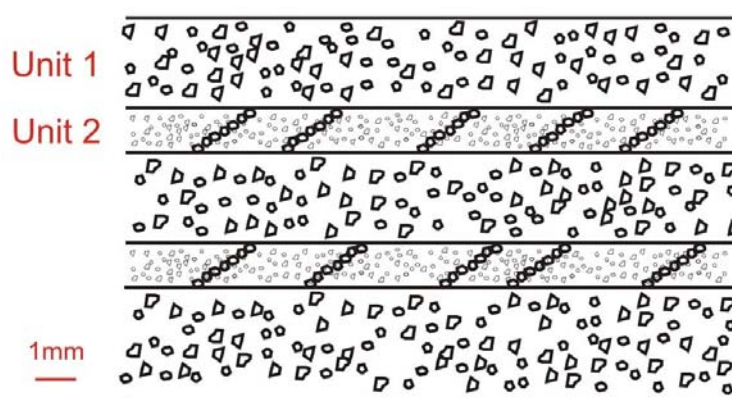
### 6.1.2 Thin section analysis of samples from facies association 2

Eight thin sections from this facies association (FA2) was studied. The fining upwards sandstone developments (the samples: RITF-1-1-09 and RITF-1-2-09) have angular grains in



sizes from silt to very fine sand (0,04 – 0,1 mm). Smaller grains are elongated. The grain contacts seem to be regular. Grains are tightly compacted with clay cement between. The sandstone is well sorted. Distinct parallel lamination is visually apparent (thickness of laminae 2 mm) (Fig. 31A). There is larger amounts of quartz in this sandstone than in coarsening-upwards successions, in this facies association (quartz/feldspar ratio is 0,5). The quartz grains are mostly monocrystalline. Biotite is the most abundant of the micas, but muscovite is also present. Some of the biotite flakes has been replaced by chlorite.

The coarsening upwards sandstone developments (the samples: RITF-1-6-09 and RITF-1-7-09) is seen in the thin sections as a fine laminated sand (Fig. 30B). The sample can be subdivided into two layers (Fig. 29). Layer 2 represents a very fine sand laminae (<1-2 mm) and consists of a thin, from fine- to medium- size sand beds (>5-8 mm), sometimes alternating with mud laminae. A few mm of cross-lamination is developed in layer 1. Larger grains in layer 1 are floating within a matrix. In both layers the sorting is good. The quartz/feldspar ratio is 0,35.

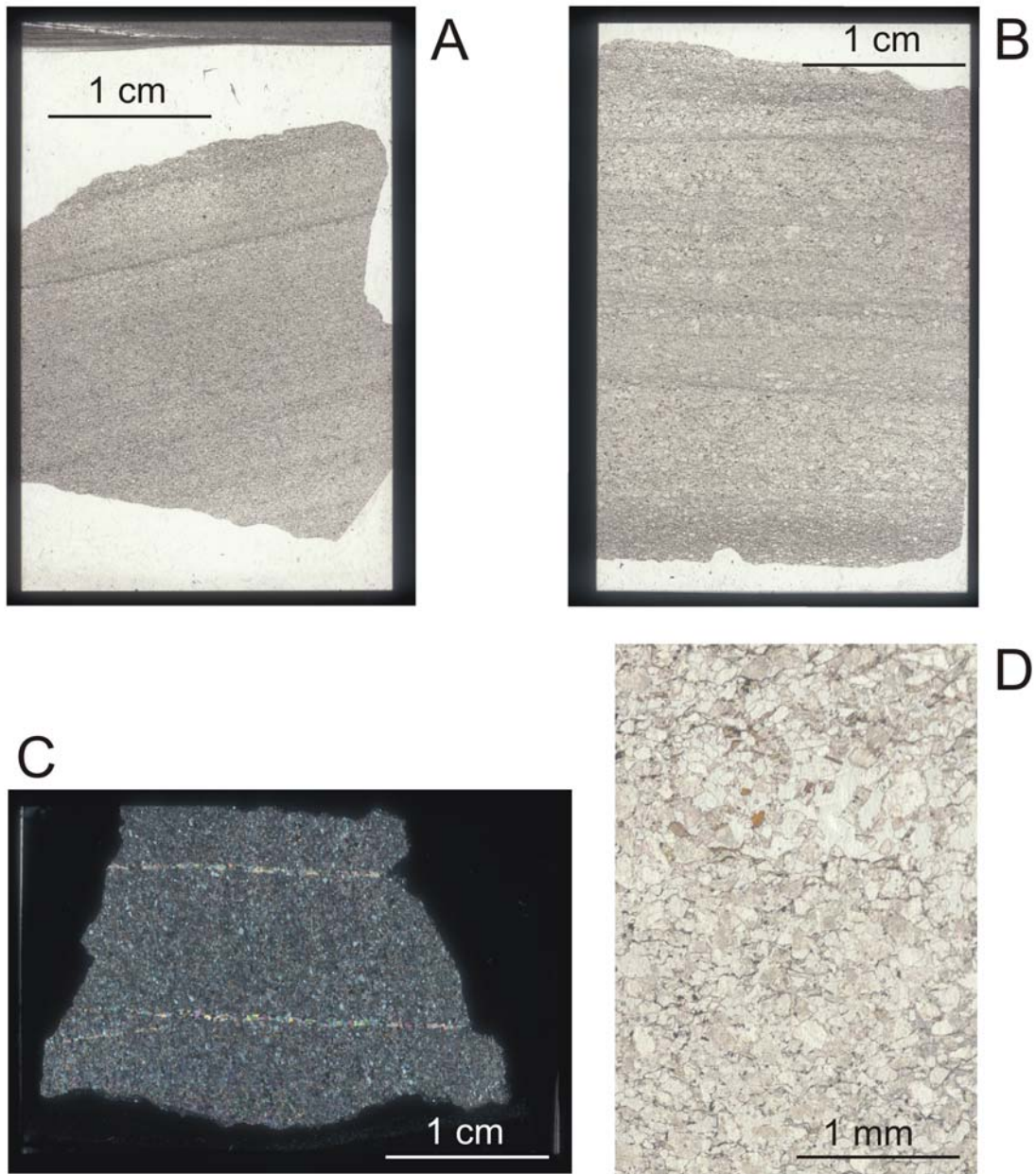


**Figure 29.** Sample from the coarsening upwards sandstone development (the sample RITF-1-6-09) with ripple drift lamination.

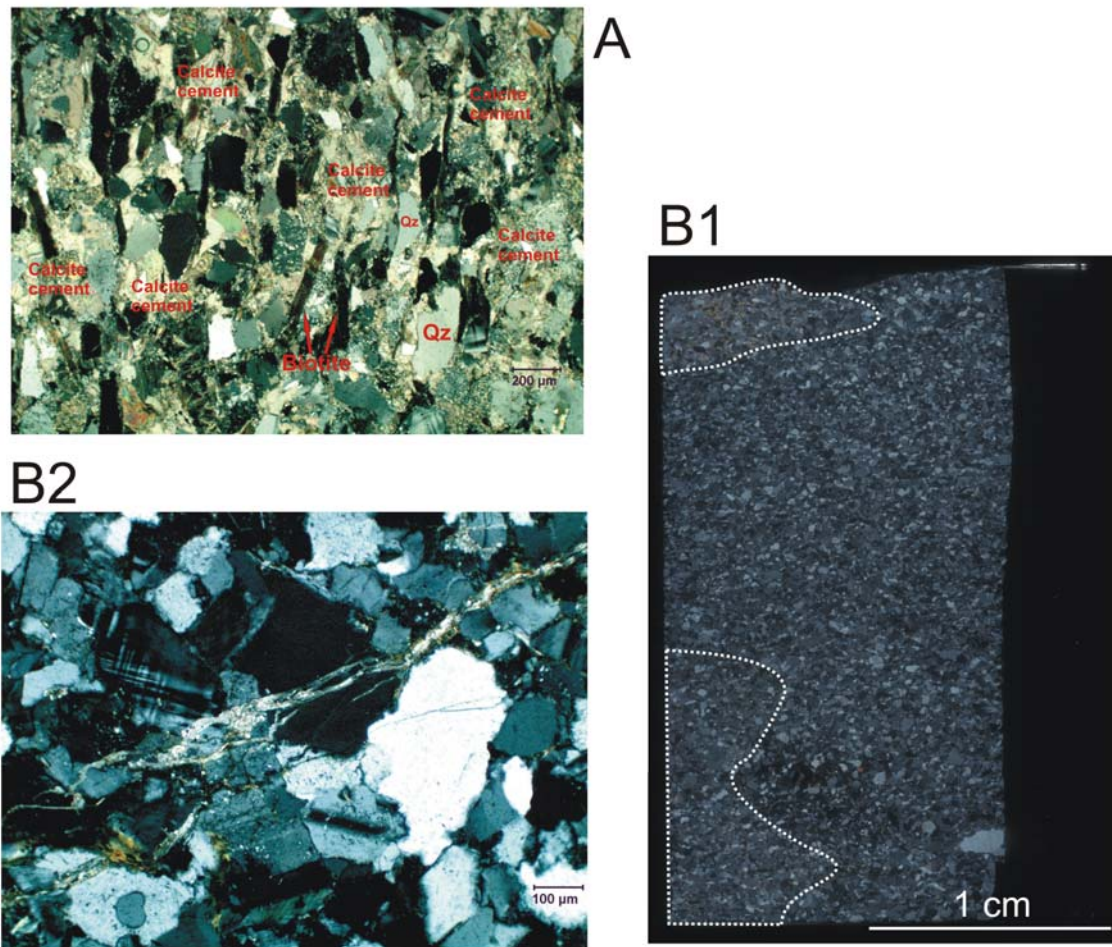
The two samples from the low angle cross-stratified sandstone (the samples: RITF-1-3-09 and RITF-1-4-09) are different from the rest. Mainly due to a very high calcite cement content. Microscopically, this rock is composed of sparitic calcite cementing (45–52 % of total), feldspar (plagioclase and K-feldspar – 28-34 % of total) and quartz (10-14 % of total). Subrounded clasts of mainly monocrystalline quartz and feldspar occur. The sandstones are fine to very fine in average size (~0,15 mm) and moderately sorted. The framework grains display a floating grain-fabric, indicating an early stage of cementation or a non-prevalence of deep burial (Pettijohn et al., 1987). Significant amount of biotite occur in the sample (8 % of total). The biotite grains are elongated and have preferential orientation, perpendicular to

calcite fractures (Fig. 31A). The same pattern is seen in other mineral grains such as quartz. The biotite flakes are partially replaced by chlorite. Calcite fracture filling structures appear in the sample (Fig. 30C). Grains are deformed by these structures. No fossil fragments have been observed.

The thin sections of the massive sandstone beds (the samples: RITF-1-5-09 and RITF-1A-1-09) display grain-supported texture. The grains have angular to subangular shape, with an average grain-size of medium sand (~0,25 mm). The biggest grains have size 0,85 mm. This sandstone is poorly sorted and has good/moderate porosity (Fig. 30D). Minor patches of calcite cement occur in one sample (Fig. 32/B1). Carbonates are connected with open fractures, presently not filled with cement, although in the other sample, from the same facies, fractures are filled with calcite (Fig. 31/B2). Minor amount of accessory minerals (e.g. zirkon) have been found (<1 % of total).



**Figure 30.** Thin section photos from facies association 2: A) the sample RITF-1, the fining upwards sandstone development exhibit very fine laminae (plane polarized light view); B) plane polarized light view of the sample RITF-1-6-09, the coarsening upwards sandstone development; C) crossed polarizers view of the sample RITF-1-3-09, the calcite cemented sandstone, the two parallel fractures filled with calcite are visible; D) the sample RITF-1A-1-09 of the massive sandstone.



**Figure 31.** Thin section photos from facies association 2: A) crossed polarizers view of the calcite cemented sandstone (the sample RITF-1-4-09). The elongated grains exhibit preferential orientation; B1) crossed polarizers view of the sample RITF-1A-1-09. The massive sandstone with areas of calcite cement (indicated by the white, dash line; B2) the sample RITF-1-5-09 of the massive sandstone. The fracture is filled with calcite.

### 6.1.3 Thin section analysis of samples from facies association 3

Nine of the studied thin sections belong to facies association 3. Four samples studied from the RITF-3 (the samples: RITF-3-2-09, RITF-3-3-09, RITF-3-4-09 and RITF-3-6-09) have angular to subangular shape of clasts and poor sorting. The matrix is characterized by angular grains and moderate to good sorting. The matrix grains are from medium sand to coarse sand. In thin sections grains of quartz (mostly monocrystalline), plagioclase, microcline and gneissic rock fragments were found. Fractures occur in larger clasts/grains and some minor fragments have been detached (Fig. 32/A2). In the sample RITF-3-3-09 significant amounts of calcite cement occur (11% of total; see Fig. 32/A1). Larger biotite flakes are visible in the thin section. These are bent and deformed between other clastic grains. Sericite aggregates have replaced plagioclase during sericitization (Fig. 32C). Some accessory

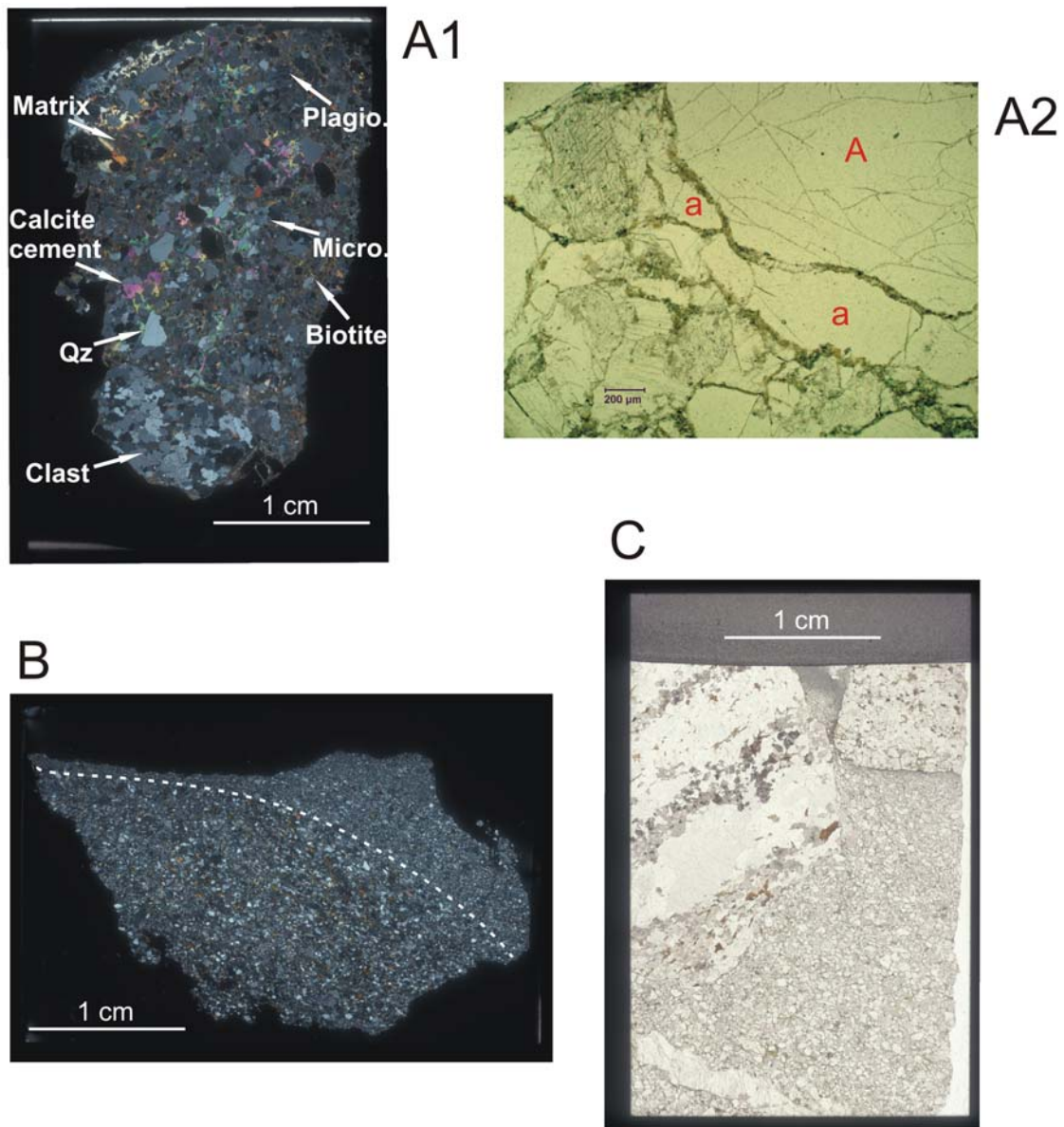


minerals have been found (e.g. zirkon, epidote). Low-grade metamorphic minerals occur in minor amount (<5 % of total): chlorite, actinolite, stilphnomelane.

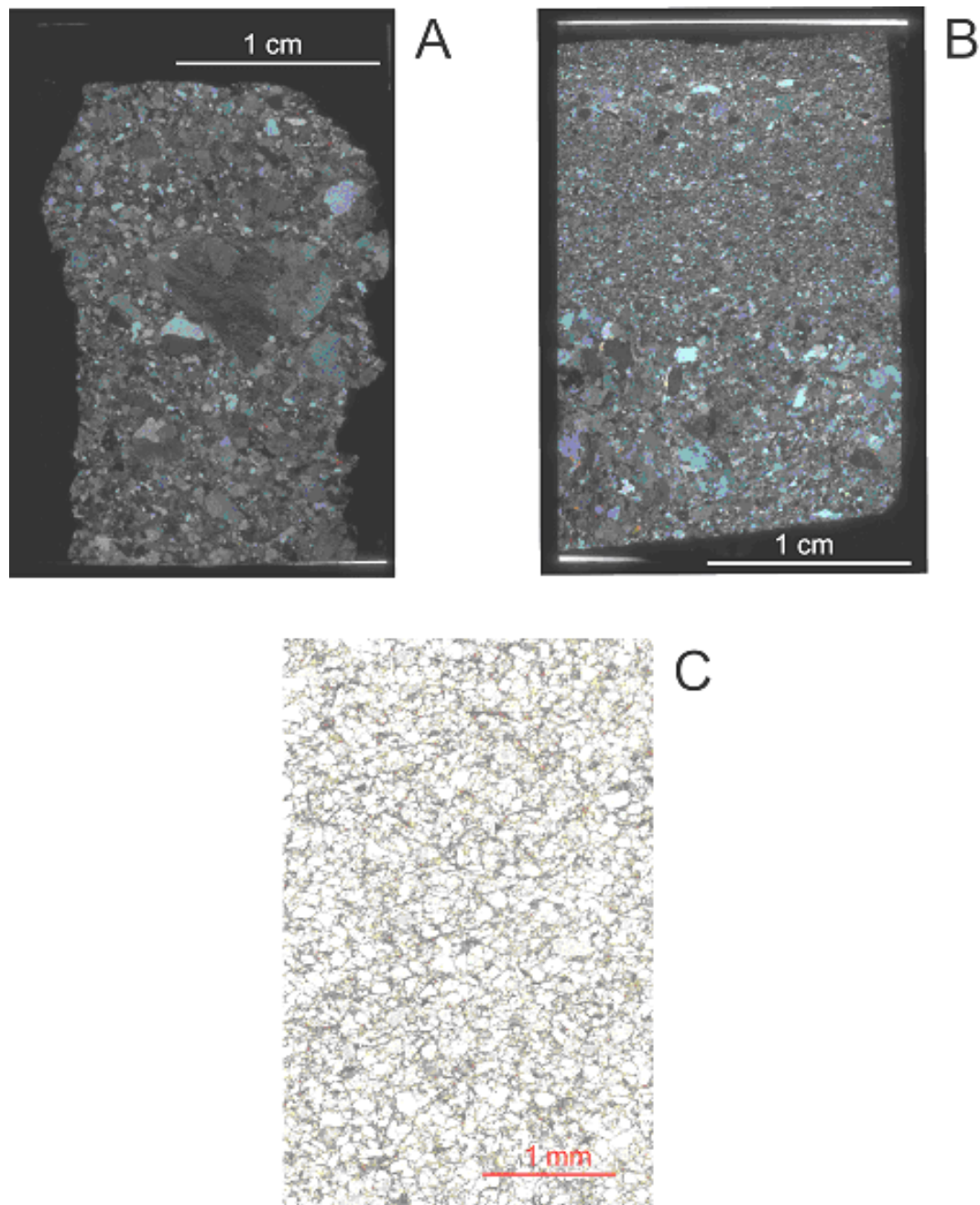
The conglomerate from facies association 3 (the sample RITF-4-8-09) consist of subangular grains within moderate sorted matrix. The matrix is laminated with fining upwards development (Fig. 33B). Average grain-size is 0,1-0,18 mm. The abundance of feldspar is much larger than quartz; the quartz/feldspar ratio is 0,25. Significant amount of biotite occur in the conglomerate units (up to 20 % of total). Biotite flakes are elongated and oriented parallel to the bedding plane. The mineral characteristics indicate the greenschist facies (chlorite, actinolite). Sericite has replaced plagioclase.

The conglomeratic sandstone beds (the sample RITF-4-7-09) consist of grains with average size of 0,2 mm. The grains have angular to subangular shape. It is a grain supported sandstone with angular clasts (Fig. 33A). The grains are 0,2 mm in size and poorly sorted. Strong compaction occur. Minor amount of carbonate cement was found in the sample. Biotite flakes occur in big number (12 % of the total). Some of them have gradually replaced by chlorite. The quartz grains are normally monocrystalline.

The sandstone beds, where convolute lamination occur (the sample RITF-4-6-09), display elongated with grain-size of 0,15-0,2 mm. The sorting is very good (Fig. 33C). Matrix has brown colour. There is significant amount of biotite/chlorite in the sample (22 % of total). Actinolite needles occur (up to 3 mm). The quartz abundance is relatively high compared to the other samples in facies association 3 (quartz/feldspar ratio ~0,7) and quartz grains are mostly monocrystalline.



**Figure 32.** Thin section photos from facies association 3: A1) crossed polarizers view of the sedimentary breccia (the sample RITF-3-3-09); A2) plane polarized light view of the sample RITF-3-3-09. The smaller fragments (a) are detached from the fractured, bigger fragment of the rock (A); B) crossed polarizers view of the sample RITF-3-6-09. The matrix supported breccia. The two layers with different grain-sizes: medium sand (below white, dash line) and fine sand (above white, dash line); C) plane polarized light view of the sample RITF-3-2-09 from the sedimentary breccia. The two bigger clasts at the top of the photo within the matrix. The feldspar grains in the clasts are partially replacated by sericite (the strings cavities in the clast – in the upper left corner).



**Figure 33.** Thin section photos from facies association 3: A) crossed polarizers view of the conglomeratic sandstone, poorly sorted (the sample RITF-4-7-09); B) crossed polarizers view of the conglomerate (the sample RITF-4-8-09), with moderate sorting; C) plane polarized light view of the sample RITF-4-6-09, the soft sediment deformed sandstone with good sorting.

## 6.2. X-ray diffraction analysis

X-ray diffraction analysis (XRD) was used to qualitatively and semi-quantitatively determine the mineral content in the bulk. The semi-quantification is based on the bulk runs and the contents on selected peaks. The peak area derives from summing the counts above the background within the interval determined by peak borderlines. A complete sample list of of

XRD bulk data is presented in Appendix 2 and Figure 35. In addition, their position within the stratigraphic succession (logs) are indicated in the sections: RITF-1 (Fig. 10), RITF-3 (Fig. 11) and RITF-4 (Fig. 12).

### **6.2.1 Facies association 1**

Two rock types with different properties: breccia and suevite have been grouped in FA3, this great difference in composition is reflected in the XRD analysis. The sample taken from the breccia (the XRD sample RITF-4-1-09) consists of feldspar, which is the most abundant mineral in the bulk 65 XRD%, calcite 8,5 XRD%, chlorite 7,5 XRD% and quartz 7 XRD%.

The XRD results from melt rocks analyses (the XRD samples: RITF-4-2-09 and RITF-4-4-09) are totally different from all the others (Fig. 37). The quartz/feldspar ratio stand at the level of 0,41 (Fig. 34). A significant content of dolomite 5,5-8,5 XRD% has been detected. Calcite is also present in one sample – 5,5 XRD%. The biotite and chlorite content is varying between 4-17 XRD% (biotite) and 1-7 XRD% (chlorite).

### **6.2.2 Facies association 2**

Four different types of sandstones (see Fig. 15) will be discussed in this chapter: fining upwards sandstone (the XRD samples: RITF-1-1-09 and RITF-1-2-09), coarsening upwards sandstone (the XRD samples: RITF-1-6-09 and RITF-1-7-09), the low angle cross-stratified sandstone (the XRD samples: RITF-1-3-09 and RITF-1-4-09) and the massive sandstone (the XRD samples: RITF-1-5-09, RITF-1A-1-09 and RITF-1A-2-09).

The quartz content in the fining upwards sandstone units is even higher than in coarsening-upwards one. The quartz contributes to 13-15 XRD% of the total. It is the highest amounts of quartz in all samples studied (Fig. 37). Feldspar is still dominating with an average 58 XRD%. Biotite display low contribute (1-3 XRD%) but chlorite content is significant varying between 6-13,5 XRD%. Actinolite is also active with an average 5 XRD% of the total.

The quartz content, in the sample from coarsening upwards sandstone, is from 6 to 11 XRD%. In these samples feldspar is the most abundant mineral, contributing with from 68 to 82 XRD%. High values of actinolite (an average 4 XRD%) and chlorite (5 XRD%) are present. Calcite content is very low compare to adjoining beds – below 1 XRD%.

The low angle cross-stratified sandstone has a different composition. In the samples calcite is the dominating mineral with value of 65 and 49 XRD% (Fig. 37). Feldspar

contribute with 23 and 35 XRD%, while the quartz content is 3 XRD%. Mica (mostly biotite) is making up 4,5 XRD%.

Feldspar is dominating in the massive sandstone, an average content of 77 XRD% of the total (Fig. 37). Quartz contribute with an average 7 XRD%. The chlorite content in these analyses is about 7 XRD%.

### **6.2.3 Facies association 3**

The XRD values of sample from the conglomerate (the XRD sample RITF-4-8-09 of the section RITF-4) are different. In this sample feldspar content is similar 72 XRD%, but with different proportion between K-feldspar and plagioclase (respectively 35 and 37 XRD%). The calcite content is making up 11 XRD% of the total. The quartz content contribute 4,5 % XRD%.

The two samples taken from conglomeratic sandstones (the samples: RITF-4-3-09 and RITF-4-7-09) contain an average feldspar content of 80 XRD% of the total (Fig. 37). Quartz contribute on the average 4 XRD%. From metamorphic minerals chlorite is dominating with an average 7,5 XRD% (Fig. 36).

The main two minerals in the soft sediment deformed sandstone (the XRD sample RITF-4-6-09) are feldspar (68 XRD%) and quartz (10 XRD%). Biotite contributes 4,5 XRD% of the total and chlorite twice as much.

The XRD results from the sedimentary breccias (the XRD samples: RITF-3-1-09, RITF-3-2-09, RITF-3-3-09, RITF-3-4-09 and RITF-3-5-09 of the section RITF-3) are different due to clasts content in the bulk. The most abundant mineral is feldspar. Samples have average feldspar content of 74 XRD% of the total (Fig. 37). Biotite content is varying between 28 XRD% (matrix poor sample) and 3 XRD% (matrix rich sample). Quartz is also varying between 9 XRD% (more matrix in breccia) and 4 % (less matrix in breccia). In one of the samples calcite is contribute with 13 XRD% of the total (more matrix in sample). The rest of samples do not display significant amount of this mineral.

In the matrix supported breccia (the XRD sample RITF-3-6-09) on the top of the succession of the section RITF-3 K-feldspar dominate almost 57 XRD%. The second most abundant mineral in the bulk is plagioclase which has 21 % XRD of the total. The quartz contribute with 11 XRD% of the total. The mica content in this sample is very low, less then 0,5 XRD%). The same with calcite which contribute with 1 % of the total. Metamorphic minerals are abundant in the sample but only actinolite has significant amount 5 XRD% (Fig. 36).

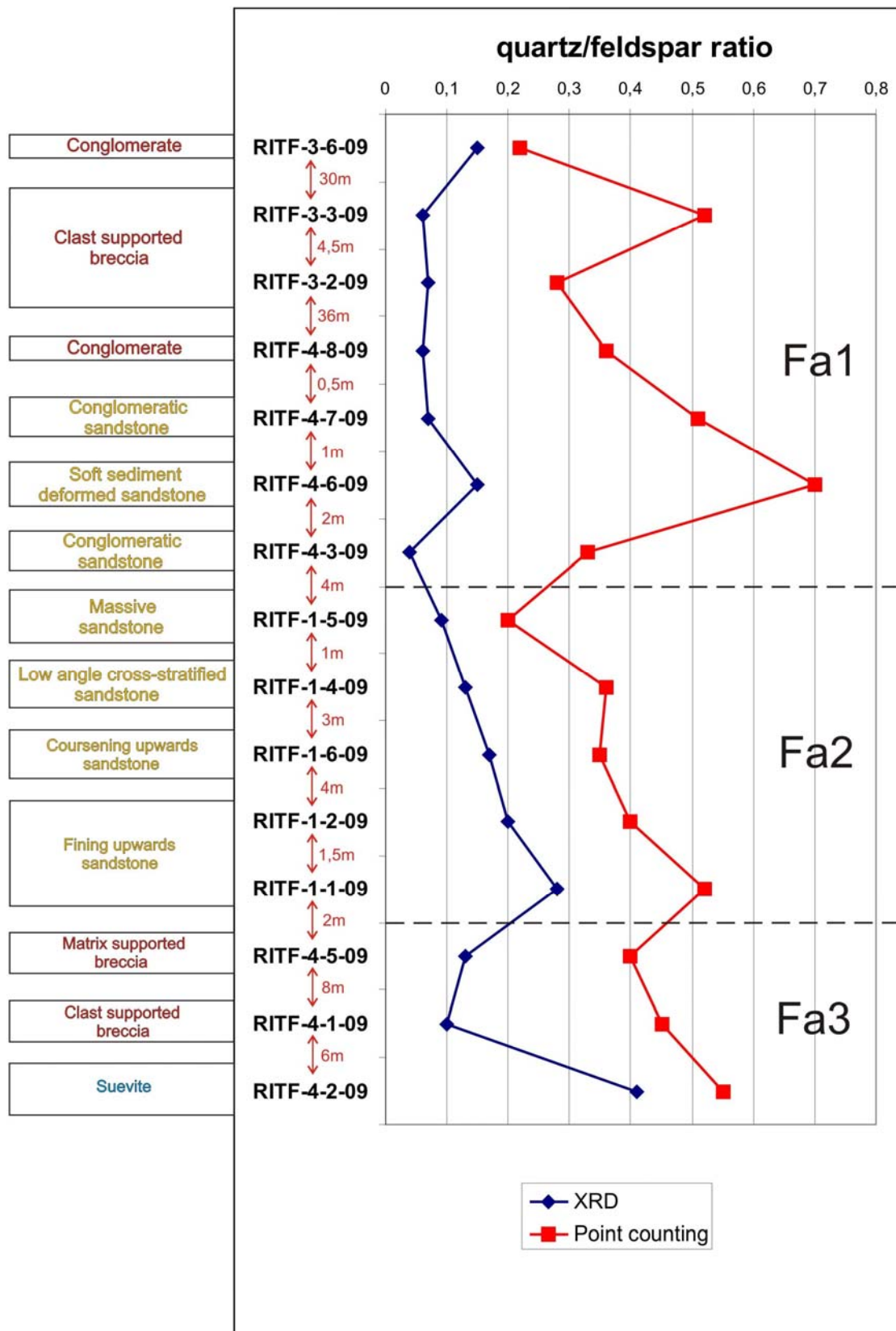
In the samples analyzed from this facies association pyrite contribute with low value (less than 0,5 XRD%). The feldspars dominate in all analysed samples. Chlorite content is highest in the samples from deeper in stratigraphic column. In the two samples (sedimentary breccia – RITF-3-3-09 and conglomerate – RITF-4-8-09) significant calcite content appear (~10 XRD% of the total).

The quartz/feldspar ratios have been calculated from both results of XRD analyses and thin sections point counting. The blue curve (XRD analyses) follows the trends of the red curve (point counting) but they display different values/levels. Several factors influence on this among others:

- in the XRD analyses not the highest intensity of quartz was used (35 % - in this peak mineral phase onlapping does not occur);
- samples taken for XRD analysis contained more clasts (enlarge number of feldspar);
- in the X-ray diffraction method the quantitative information of the feldspar content in the bulk is highly disturbed by different minerals peaks onlapping;
- in thin section some of feldspar twinning could be recognized as quartz grain;
- the matrix composition cannot easily be recognized by microscopic investigation of a thin section due to optical resolution.

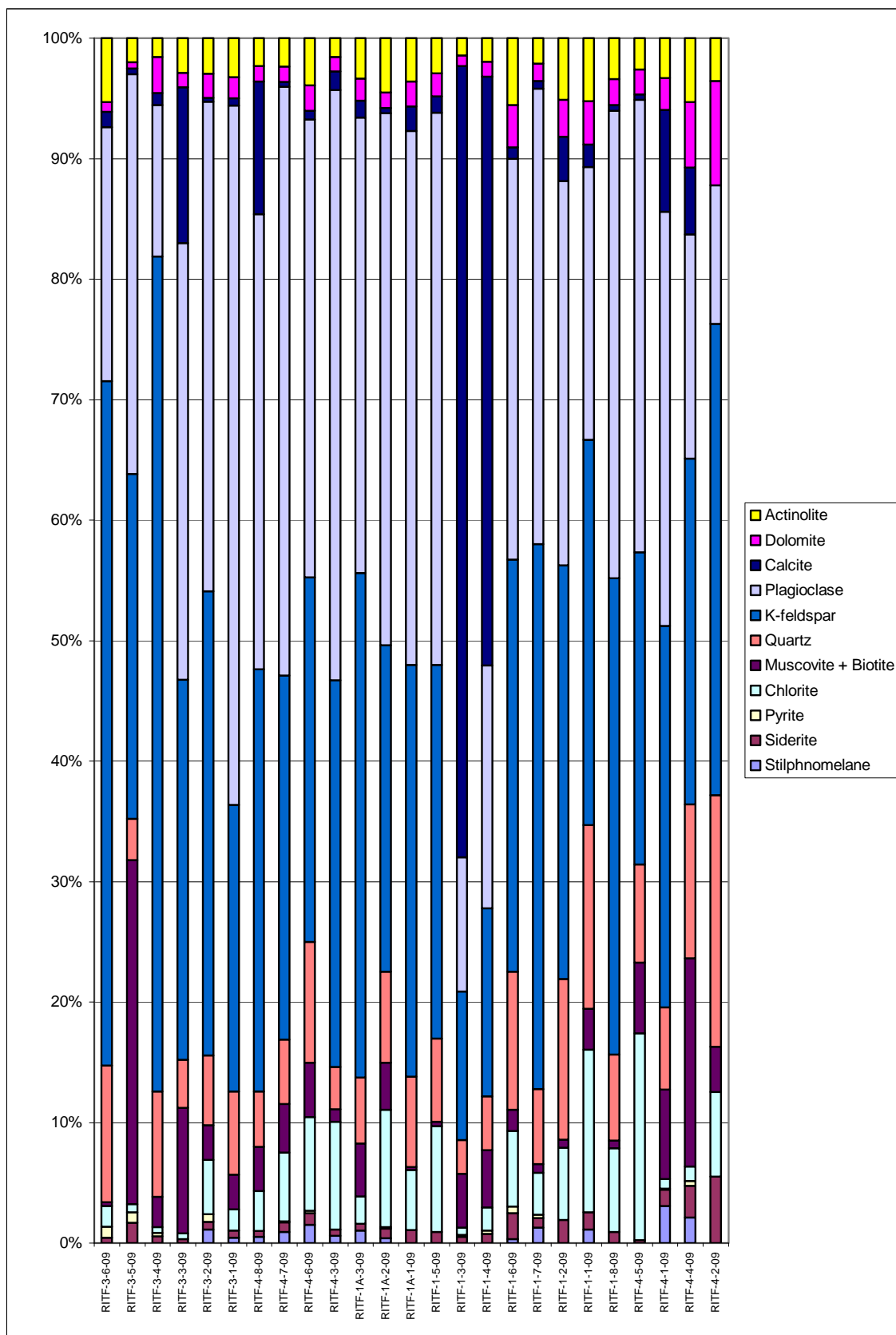
Quartz/feldspar ratios show some variable trends in the facies associations (Fig. 34). The trend in the FA3 is slightly varying to constant (seen in XRD analyses). The FA1 and FA2 show the upwards decreasing quartz/feldspar ratio (seen in both XRD analyses and thin section point counting). On the boundaries between facies associations abrupt changes in the quartz/feldspar ratios are visible. According to the XRD analyses the quartz/feldspar ratio reach the highest value in the suevite and the lowest in the conglomeratic sandstone, conglomerate and breccia (all from the facies association 1). Point counting shows the highest quartz/feldspar ratio in the soft sediment deformed sandstone (facies association 1) and suevite (facies association 3). The lowest values for this method are in the massive sandstone (FA2) and conglomerate (FA1).

In all samples the XRD analyses show the metamorphic minerals (chlorite, actinolite and stilpnomelane) content is upwards decreasing in the stratigraphical column (Fig. 36). The quartz content reveal the same trend in the stratigraphical column, but the biotite content is upwards increasing (Fig. 37).

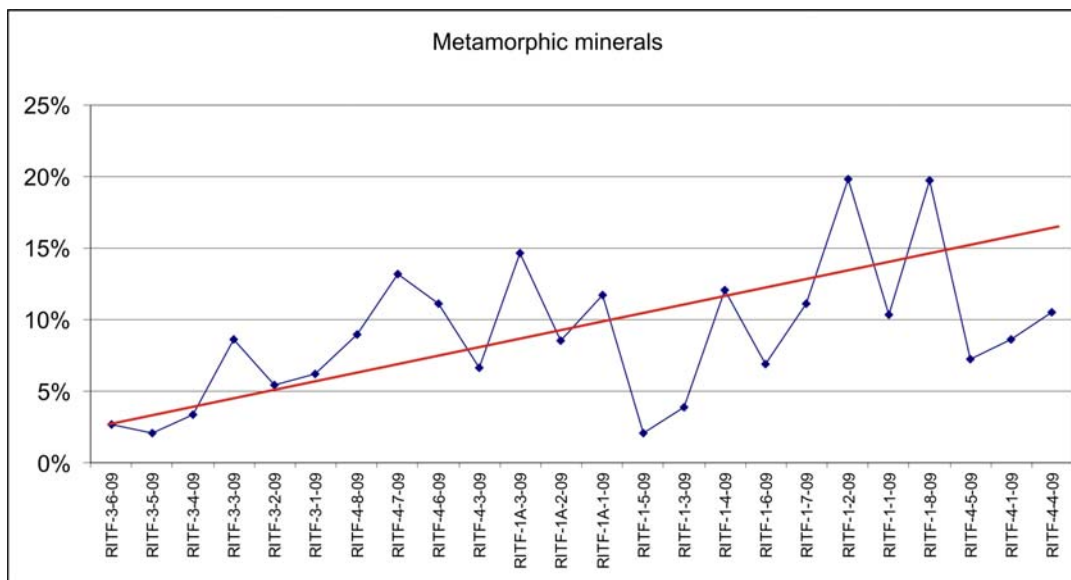


**Figure 34.** The graph shows quartz/feldspar ratios calculated from both results of XRD analyses and thin sections point counting. The vertical column with facies is a composite simplified stratigraphical column. The red arrow between the sample names indicates an interval.

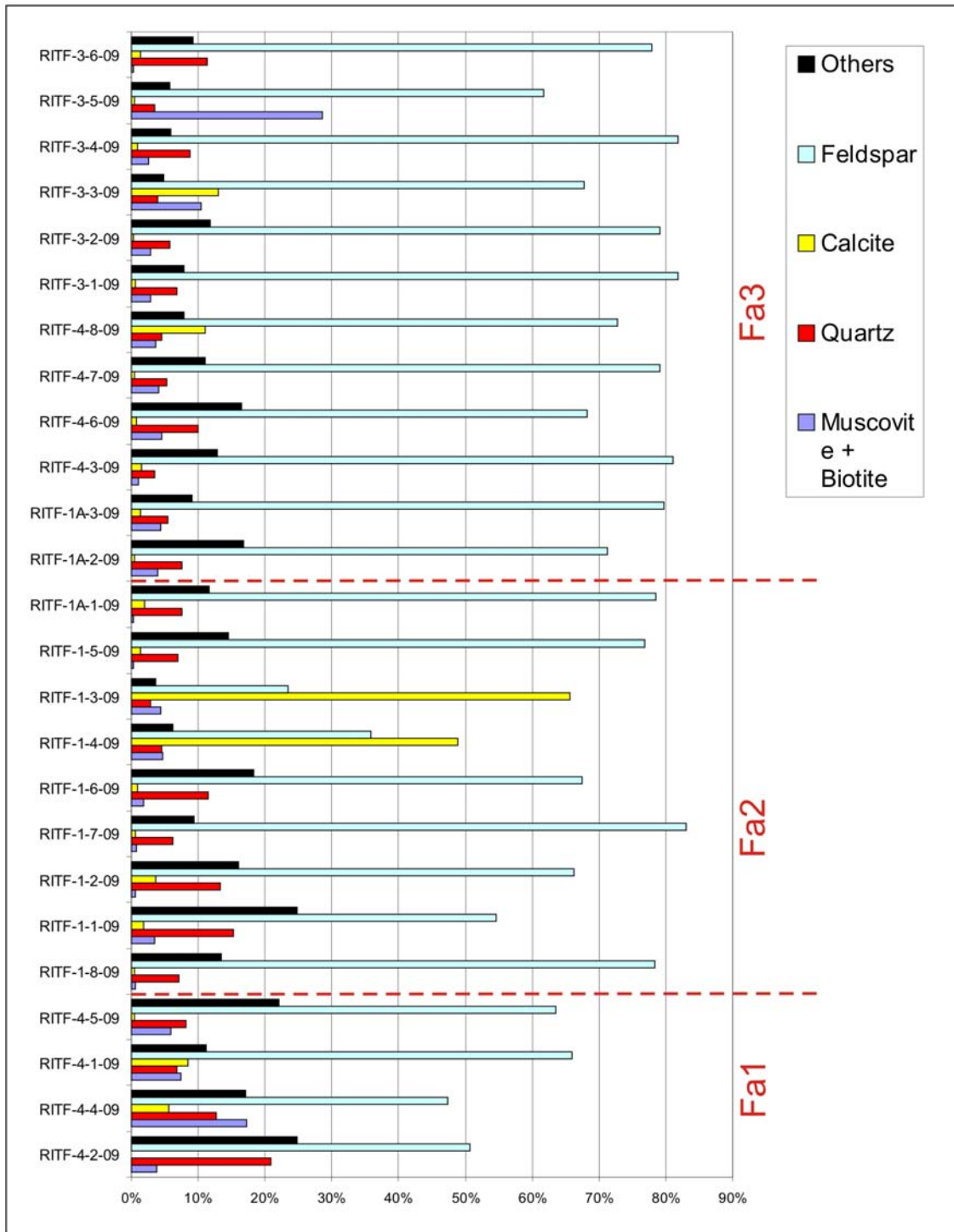




**Figure 35.** All minerals from bulk analysis (from all three sections: RITF-1, RITF-2 and RITF-3).



**Figure 36.** Blue curve: the total amount of the metamorphic minerals (chlorite, actinolite and stilpnomelane) of all samples (XRD%). Red line: a trend line (the average amount of the metamorphic minerals in the bulk). The x-axis represents a stratigraphical column (from left to right).

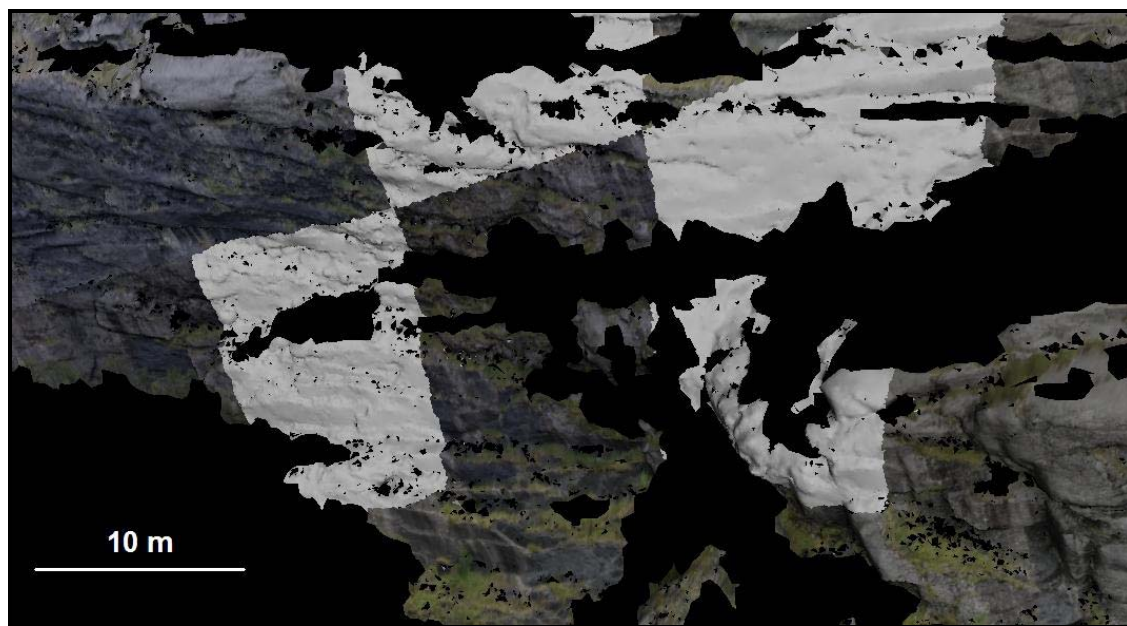


**Figure 37.** The amounts of minerals of different lithologies in a stratigraphical column (XRD% of total). The facies are grouped into facies associations (red, dash line marks border between FA). The feldspar is K-feldspar and plagioclase, and other minerals represent stilpnomelane, siderite, pyrite, chlorite, quartz, dolomite and actinolite.

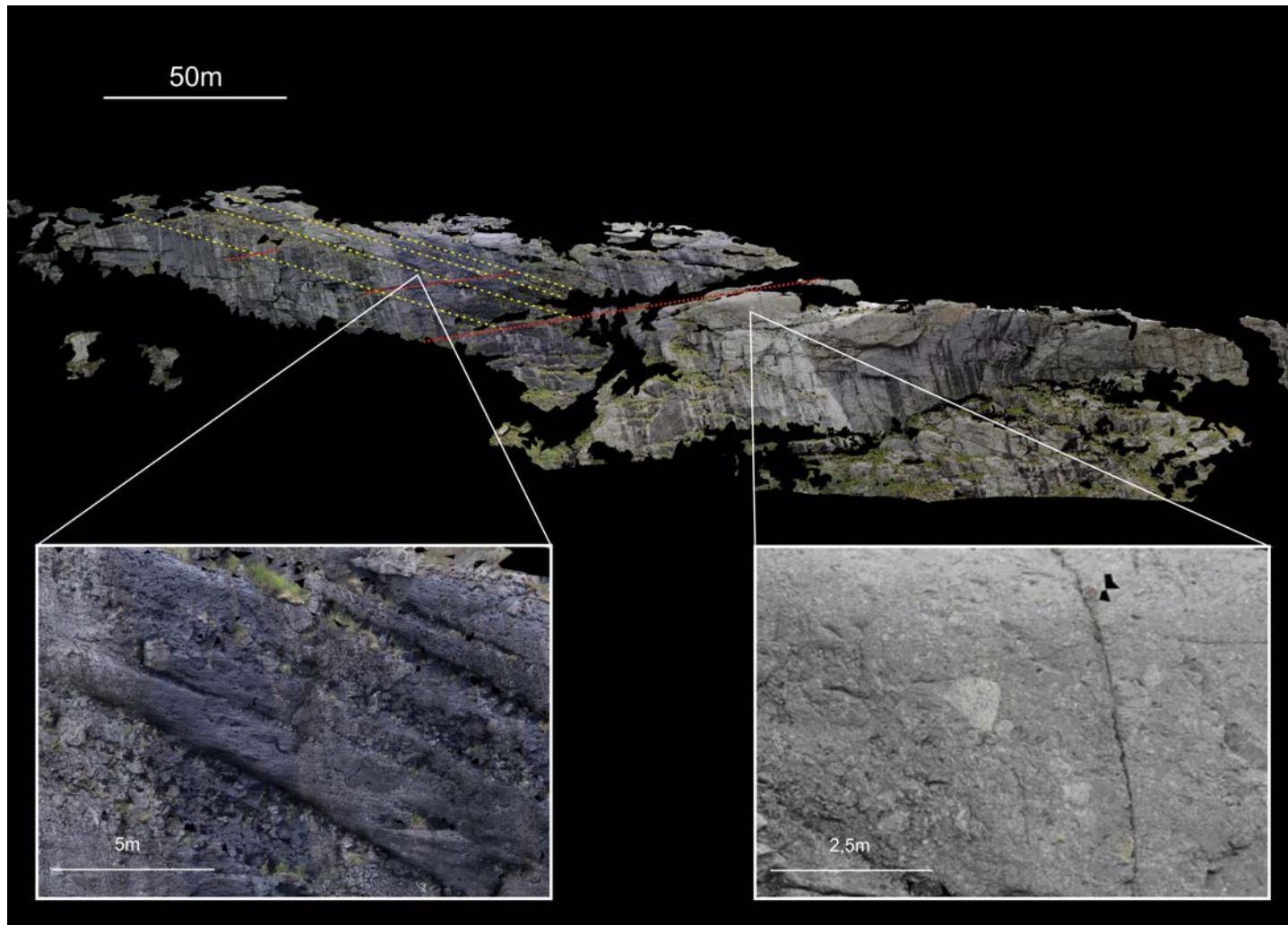
## 7 Lidar acquisition data

Lidar image visualization and interpretation was performed by applying the 3D visualization software (Buckley, 2008).

The Lidar image covers most of the outcrop of the west face of the Svodene hill (Fig. 9 and 38). The 3D model is a composition of the measured Lidar points (processed by software) and photo (taken by a camera) (Fig. 38). Due to shifting weather conditions, solar radiation at different angles of incidence, and wet rock walls the image consists of areas with different contrast indicating differences in composition. One of the most striking observations is that the upper part of outcrop (Fig. 39; above red, dash line) has weathered surface and the lower part (below red, dash line) is smooth. On the weathered surface breccia beds are visible but it is difficult to follow each bed laterally. There are bands on the wall crossing breccia beds at a low angle (red, dash lines). The bands are tens of centimeters to tens of metres in width. The bands occur only on weathered surface. Closer investigation of the 3D model brought more details about breccia deposits. In Figure 39 we can see poorly sorted sediment.



**Figure 38.** The 3D model of part of the outcrop (the Svodene hill). It is a mosaic of the plane of the rock outcrop (bright grey area) and photos. The surface model is constructed by applying a skin (photos taken by camera) over the Lidar points. The model shows weathered surface (coarse surface visible on the bright grey plane), and breccia beds (pointed in Fig. 39). Vegetation has green colour in the 3D model. Most of vegetation was cut out during processing (black area).

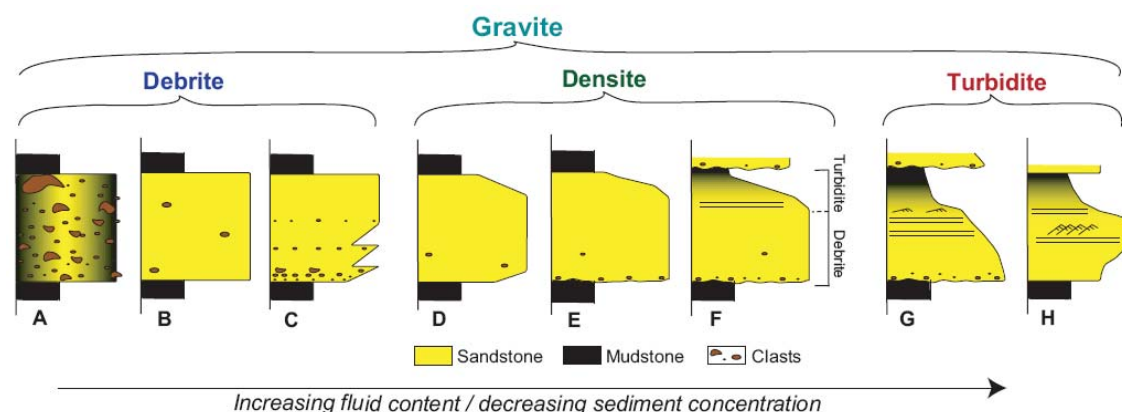


**Figure 39.** The 3D model (up) of the west face of the Svodene hill (see Fig. 9). The sediment beds are visible (dip direction – yellow, dash lines) and the bands (dip direction – red, dash lines). The weathered rock surface (lower left corner) and the smooth rock surface (lower right corner) both show poorly sorted breccia deposits.

## 8 Discussion of data and deposition models

The post-impact deposits in the Ritland impact structure refer to different sedimentation processes. Steep crater walls and large amounts of impact material favor gravity controlled sedimentation during the so-called impact modification stage. Subsequently, suspension deposition of fine-grained material took place, when water filled the crater.

In this study, gravity flows are classified according to Mulder and Alexander (2001), who took physical flow properties and sediment-support mechanism into consideration. Gani (2004) developed a classification based on four parameters: 1) sediment concentration, 2) sediment-support mechanism, 3) flow state and 4) rheology. According to this classification the gravite (all gravity controlled sedimentation processes) are subdivided to: debrite, densite and turbidite (Fig. 40). This classification will also help to describe different sedimentation processes, which took place in the Ritland structure.



**Figure 40.** The lithologic models for gravity flows deposits: (A): cohesive debrite; (B-C): non-cohesive debrites; (D-F): densites; (G): turbidite (Bouma sequence); (H): turbidite (deposit of hyperpycnal flow) (Gani, 2004).

In description and discussion of post-impact sedimentation it is important to define the impact location on land or in water. The Ritland crater was most likely a terrestrial impact structure (Riis et al., 2009). In the case of a marine impact we would expect larger amounts of clay or marine fossils. Discussions of several other marine impact structures, such as Mjölknir crater, Norway (Dypvik and Jansa, 2003; Dypvik et al., 2004; Dypvik et al., 2006); Kärđla crater, Estonia (Puura and Suuroja, 1991; Suuroja et al., 2001); Flynn Creek crater, USA (Schieber and Over, 2005) and Lockne crater, Sweden (Dalwigk and Örmö, 2001), include such evidences. No indentifications of clay/shales or fossils have been founded in impactite samples from the Ritland crater.

In case of marine impact a possible resurgence of seawater should in short time after impact break through the uplifted rim wall of the crater, trap and incorporate fractured lithologies from

the sea-floor (Dalwigk and Ormö, 2001). Such events favor extreme turbulence allowing for short term suspension transport of pebble-size particles (Nicols, 1999). Turbulence allow the coarser particles to settle early, and fine-grained material settled last (Boggs, 2006), we should expect graded top of breccia (Schieber and Over 2005) in the facies association 1, but it does not occur. The flash water flood should have left another imprint as resurged gullies<sup>6</sup> cut across the rim (Dypvik and Jansa, 2003). During the last fieldwork and previous (Riis et al., 2009) such erosional features were not found. Lack of these evidences makes the marine impact origin of the Ritland structure less likely. This needs more investigation.

## **8.1 Lower succession – suevite and breccia at the base**

The lower succession is deposited in the early stage of post-impact sedimentation, seconds after impact. This succession represents the facies association 1.

### **8.1.1 Suevite**

The suevite consists of melt fragments, angular-shaped clasts (gneissic rock fragments) within fine-grained matrix. The newly excavated rock fragments were trapped in melt material before its solidification. It indicates short and rapid process of deposition, mixing melts with material derived from crushed basement. The brownish shard shape particles of altered melt (Fig. 28B), recrystallized minerals and shock quartz (Fig. 3) indicate the target rocks experienced very high temperature and pressure due to the impact (Koeberl, 2006). The suevite contains relatively large amount of quartz in rock samples (Fig. 37), reflecting high temperature and high pressure alteration of rocks during impact (Grieve et al., 1996). Quartz is more resistant mineral to such extreme conditions than feldspar. This reflects relatively high quartz/feldspar ratio of suevite (Fig. 34).

The stratified flow patterns of melted rocks in the Ritland structure clearly appear at weathered suevite surface (Fig. 19D). The impact melt deposits on crater floor could be distributed as (1) smooth dark pools of material perched on terrace ledges and (2) lavalike flows with and without well-drained channels and levees (Kessler and Bedard, 2000). It is difficult to see these structures in the Ritland crater. Macroscopic flow features in the suevite indicate that the material was molten and behaved in a fluid manner at the time of emplacement (Howard and Wilshire, 1975). In cratering events decompression during the excavation stage, may allow opening of fractures within the crater floor and walls (Dressler and Sharpton, 1997), consequently molten material can use these fractures as channels or/and

---

<sup>6</sup> The resurged gullies are erosional features caused by the erosional force of the resurging sea water after the impact.



small depressions along with. Ballistically ejected material (melt rocks, rock fragments) from the crater along with material displaced by plastic flow towards the crater center may move like epiclastic volcanic debrites (Kessler and Bedard, 2000). Often impact melt rocks occur as bodies of rock crystallized from melt material in the form of sheet-like masses, in the crater center and on the crater terraces. This could refer to the Ritland structure where the melt rocks was found in few places as lenses of melt rock body (Fig. 44/1).

The suevite was eroded and reworked (at the top of the unit) by the overlying breccia (Fig. 27, right). Consequently the collapse time of the crater rim is short, compared to the rate of sediment accumulation (Settle and Head, 1979; Melosh and Ivanov, 1999). In other sites the boundary between suevite and post-impact sediments is unclear (Fig. 27, left). Impact melt solidification is a complex process (Koeberl, 2006). The studies of the Manicouagan melt sheet was aiming at better understanding of character and way of deposition of melt rocks (Onorato et al., 1978). According to this investigation the temperature drops down to liquidus in about 100 seconds. Thereafter impact melt viscosity increases, explaining why larger clasts may be trapped before they reach the melt pool base (Melosh and Ivanov, 1999). This how it looks like in the field, in the Ritland structure (Fig. 27, left). This phase of formation may define a reasonable time limit for crater collapse. From numerical calculations and laboratory experiments Melosh and Ivanov (1999) estimated time of gravity collapse to range from 10 to 30 seconds (for craters in diameter range 10 to 100 km). Comparing this estimate to time for melt solidification, it can be seen that the crater rim will have enough time to collapse. The absolute time of melt solidification is probably much longer – Melosh and Ivanov (1999) suggest several minutes. This information may be reflected field work observations in the Ritland structure, but additional suevite outcrops have to be found, in order to reconstruct the complete early post-impact processes of deposition. This can be problematic to resolve in Ritland, both sure points of the suevite can be covered by lakes, and that most of the facies was eroded. Suevite is less resistant to erosion than the Precambrian target rocks (Dressler and Sharpton, 1997).

### **8.1.2 Breccia at the base**

An allochthonous, clast supported breccia at the base represents the very first siliciclastic deposits in the Ritland impact structure. The dominance of angular, poorly sorted clasts of local origin and a relative high feldspar content relative reflects the short transport (Fig. 19C). In addition absence of clay minerals reflect freshly crushed and unweathered rocks making up the breccia at the base. Clasts composition in breccias of facies VIIIa is

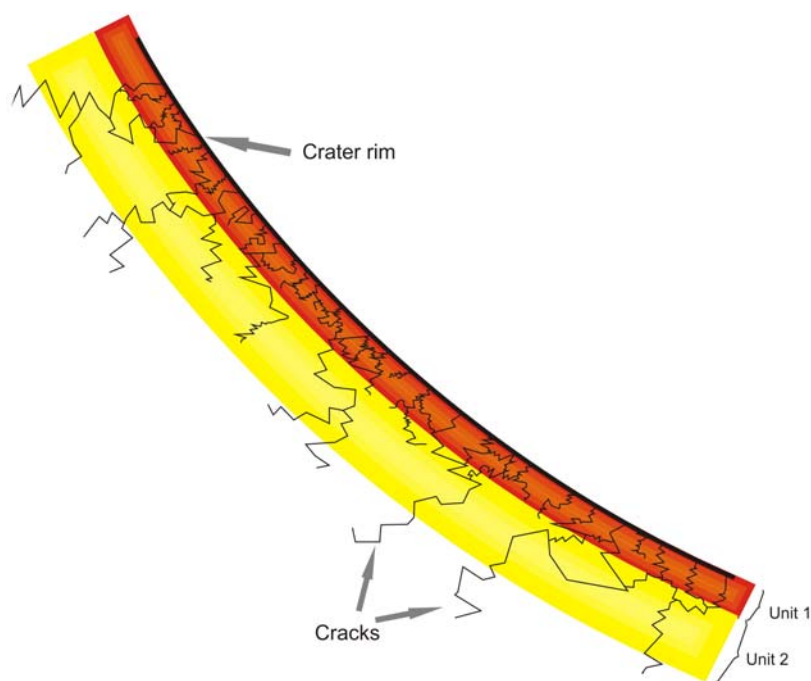
comparable to the crushed basement composition, showing that the main sediment source for these gravity flows deposits were the fractured bedrock (Fig. 37). The steepest part of the rim which collapsed into the crater bowl produces lenses of crushed rock (Fig. 44/2). Deposition of this facies most likely took place during subaerial conditions. The absence of red iron oxide staining in sediments, is integrated to be the result of rapid deposition from avalanches. The sediments were not exposed to weathering for a long time.

Most likely a few seconds after impact the steepest part of the rim collapsed into the crater, producing lenses of crushed rock (Melosh and Ivanov, 1999). The failure of the crater rim happened due to mechanical instability of the cavity walls under the influence of gravity (Quaide et al., 1965; Gault et al., 1975; Melosh, 1977). The crater rim slid down along owned failure surfaces, approximately parallel to the initial cavity rim (Settle and Head, 1979). The initial product of impact is a circular, bowl-shaped cavity with a depth/diameter ratio in the range from 1:5 to 1:4 (Melosh and Ivanov, 1999). Due to gravitational instability and collapse the crater suffered further modifications. These may include slumping of the crater walls as landslides, rock avalanches etc. Melosh and Ivanov (1999) claim wall slumping to be the main modification process for simple crater. According to Kessler and Bédard (2000) the rock avalanches are large rock masses moving rapidly downslope, generating poorly sorted deposits, of angular-shaped particles, a mixture of megablocks, boulders, gravel and cobble-size fragments. Smaller particles like sand and mud are present minor amount in these mixture. The field observations of the breccia at the base match to these characteristics.

This sedimentary breccia unit of material which moved in several direction, inward and outward, reflects sediment mixture of rock fragments and melt rocks. The suevite appears as minor patches in the terrain, and not covering whole crater floor (Fig. 13). In the Ritland structure suevite is interfingering with breccias at the base (Fig. 27). Melt rock may cover the crater basement and even fill fissure, cracks, pockets etc. Rock slides and avalanches may have eroded part of the melt, even before it has completely solidified. Reworked melt particles have been found in the breccia at the base (Fig. 28A). The reworked melt material distribution in the breccia lens suggests it being formed at the early stage during the crater rim failure (Grieve et al., 1977). The crater rim collapse produced several rock slides and rock avalanches prograding along crater floor and eroding the newly formed melt rock deposits. It can also indicate that the crater rim failure happened very fast after the impact, in order to mix breccia at the base with melted rocks.

The maximum clast-size of the breccia at the base (<50 cm; facies association 1, see Fig. 15) is smaller than the maximum clast-size of the sedimentary breccia (<2 m; facies

association 3, see Fig. 15). It may be explained by shock wave propagation in the target rocks after impact. Kinetic energy is spent ejecting material and forming accommodation space. The energy is transformed to the rock causing its melting and vaporizing (Melosh and Ivanov, 1999). Ejected material will fall down and even into the crater and its surroundings. In the field crushed basement looks heavily cracked. The energy of the shock waves decreases into basement and outwards away from the crater rim (French, 1996), therefore intensity of cracks increasing up to crater rim (Fig. 41). The most cracked part of crater rim collapse immediately. Moreover, there is a minor amount of matrix between clasts in the breccia at the base (Fig. 19C). This breccias (FA1) is displaced over wider areas than sedimentary breccia (FA1), and consequently the clasts are reworked to a larger degree.



**Figure 41.** A simplified sketch presents a fragment of the crater basement. The basement is subdivided into to units. Unit 1, closer to crater rim, has larger amount of fractures, cracks than unit 2. The first crater rim failure happened seconds after impact (unit 1). Subsequently several crater wall failures happened, over longer period of time than the first one. It is difficult to estimate dimension of each unit. Further investigation in needed.

In the Ritland impact structure hydrothermal alteration affected sediments to various degrees (Fig. 36). The highest value is seen in facies association 1 (suevie and breccia at the base). Biotite has been replaced by chlorite. The plagioclase is mostly strongly altered (sericitised). Some of the sediments have much carbonate in their matrices. It may be evidence that relatively warm fluids were percolating within the sediments (hydrothermal alteration). Many similar observations from impact structures have been described: the Gardnos crater in Norway (French et al., 1997); the Ries crater in Germany (Engelhardt,

1990); the Rochechouart structure in France (Bischoff and Oskierski, 1987); and others (e.g. Boer et al., 1996; McCarville and Crossey, 1996 In Dressler and Sharpton, 1997). Suevite exhibit signs of post-brecciation recrystallization. Such minerals like: epidot, actinolite, chlorite, stilpnomelane are characteristic for the low-graded metamorphism, so-called the greenschist facies. Greenschist facies results from low temperature, moderate pressure metamorphism. The trend in the post-impact succession of the Ritland structure is upwards decreasing (Fig. 36). It reflect a burial depth (temperature is higher with depth) and also the rock porosity (percolating water influences metamorphism; Chamberlain, 1989).

## **8.2 Middle succession – sandstone sub-unit**

The middle succession is build-up of the suspended sediment distribution in aquatic environment. This succession represents the facies association 2.

### **8.2.1 Parallel-bedded sandstone**

Facies VII is represented by several fining- and coarsening-upwards sandstone units. Grain sizes ranging from silt to medium grained. Arkosic sandstones are typically present in this facies, like most of the fine-grained deposits in the Ritland structure. The parallel bedding and parallel lamination, as well as ripple drift lamination indicate suspension flows. These features have been seen in the field and under a microscope (Fig. 17C, 29, 30A and 30B). Sandstone beds of facies VII are characterized by thin clay and silt laminae interfingering with the sand units. This shows short and quiet intervals of sedimentation out of suspension. Such sediments succession may represent turbidity current deposits (Stow and Shanmugan, 1980), however a complete Bouma sequences have not been observed. Repetitions of these sequences result in successions dominated by thick silt or sand laminae and thin silt or mud laminae. This is comparable to the facies distribution by turbidites, and analogous to the distribution of partial Bouma sequences described by Walker (1967) and others (Stow and Shanmugan, 1980).

The sedimentary structures (e.g. ripples, see Fig. 17A), internal lamination and migrating ripple lamination in the facies VII indicate periods of tractional movement during deposition of the coarser silt grains out of these suspension flows. The structures were controlled in part by the nature of flow deceleration (Banerjee, 1977).

The Ritland impact structure was a small sedimentation basin (~2 km in diameter). A space for development of the turbidity current was limited, but there are some examples of small depositional basins with fine-grained deposit. Turbidity deposits can be result of catastrophic events (e.g. the water resurge), example is known from Swiss lakes (Sturm and

Matter, 1978; Kelts and Hsü, 1980; Lambert and Giovanoli, 1988). The hyperpycnal turbidities deposited by quasi-steady turbidity currents (Alexander and Mulder, 2001) may develop on the steep crater lake margins. It could be continuity of the dense flow (the concentrated density flow). The quasi-steady hyperpycnal turbidity currents often develop in lakes (reported by Forel, 1885, 1892 in Lake Léman *In* Mulder and Alexander, 2001). This could happen in the Ritland crater filled with water.

The concentrated density flows travelled downslope in the Ritland structure along channels, soon after it past the somewhat depleted the base-of-slope the flow, continued as a true turbulent suspension flow (Mulder et al., 1998). Sediments then may have been deposited and preserved as coarsening-upwards sequences (Kneller, 1995). The coarsening-upwards succesions of facies VII may be related to the progradation of fan lobes and gradual channel filling and abandonment (Reading and Richards, 1994) The mineralogical content of the upward coarsening sandstones are similar to the upward fining sandstones (Fig. 37), with the exception of slightly higher quartz content in the fining-upwards succesion, reflecting further reworking of material. It most likely show that these two deposits (both facies VII) were derived from the same source. The transition from the concentrated density flows into turbidity currents may have taken place on the crater lake margins.

In one of the samples from the parallel-bedded sandstone of facies VII the ripple drift cross-lamination have been observed (Fig. 29). These structures are similar to the low-relief bedforms produced experimentally in sands (McBride et al., 1975). They have been termed “fading ripples” since they fade out laterally into muddy troughs. Migration of the coarse silt ripples over the muddy troughs have produced a somewhat irregular or lenticular interlamination of silt and mud. When the flow velocity decreased climbing ripples developed. Climbing ripples are common sedimentary structures of hyperpycnal turbidities (Mulder and Alexander, 2001). Low-relief, long-wavelength ripples are a third type of cross-lamination present. The appears as thinly interlaminated and slightly inclined mud/silt layers (Fig. 29). This is similar to the lamination produced experimentally by McBride et al. (1975) in sands, although the mechanism may not be the same.

Crater Lake (USA) may represent a depositional analogue of a impact structure with approximate diameter 10 km. Nelson et al. (1986) described thin, fine-grained sediments on the crater floor. These turbidites deposits on the basin floor were suggested to have developed from debris flows, flowing down the steep rim of crater lake. Many debris flows chutes cutting through the Crater Lake rim. These channels are supplied and partially covered by unsorted material from rockfalls and debris flows. Underwater investigations showed these



subaerial channels to continue below water as pathways for sediment-gravity flows. These observations may also explain a shift in depositional processes in the Ritland structure, from debris flow into turbidity current. Conglomerate units of facies I (Fig. 23) could be a downslope-migrating debris flows which transformed into density flow or/and turbiditic current. Mulder and Alexander (2001) theoretically, and Hampton (1972) experimentally, described such transformations of density flows into turbidity currents. Facies I most likely represents sediments deposited when the water broke through the crater rim. Then water-saturated sediments started to flow down-slope, as they entered water level of lake the flow was disrupted and become turbulent (Middleton, 1966). Hampton (1972) described debris flow generating turbidity currents. He claimed the transition from debris flow to turbidity-current flow to take place by dilution of sediments from the front of the debris flow. The sediments are thrown into turbulent suspension, and mix with water to form a turbidity current. This may also have been the case at Ritland, where conglomerate units of facies I are found close to the steep crater rim (RITF-4, see Fig. 13), while closer to the crater base, fine-grained sediments were seen. The conglomerate units (RITF-4, see Fig. 23) strikes and strikes of other sedimentary structures, e.g. ripple (Fig. 26) indicate the direction of the flow towards the place where fine-grained sediments were deposited (RITF-1, see. Fig. 13).

The mud flakes conglomerates seen in some of sandstone beds (Fig. 17B) may have several explanation e.g.: (1) row of mud flakes, probably remnants of the eroded mudstone division; (2) syneresis cracks, which are shrinkage crack formed under the water in clayey sediments (Tanner, 2003); (3) the interstratal cracking; (4) cracking caused by earthquakes.

Other sedimentary structures are seen in this facies e.g. a scour and fill structures formed as a result of scour by currents and subsequent backfilling as current velocity decreases (Shepard, 1969). Convolute lamination is most common in turbidity current deposits (Hampton, 1972), but in the sandstones of facies VII convolute lamination does not occur.

### **8.2.2 Low angle cross-stratified sandstone**

The low angle cross-stratified sandstone are different than surrounding sediments, in respect of both mineral composition and sedimentary structures. Low angle (in this case 9 degrees) cross-stratification could be formed during high-water, where the edges of sandflats may be reworked by wave action, resulting in redeposition of low angle cross-stratified sandy sediments along coastal areas of the lake (Goldring and Bridges, 1973). Horizontal lamination and very low angle cross bedding, which is not burrowed, are common features of the back shore, beach crest, and fore shore deposits (Bernard et al., 1958). Evidence of basal erosion

(Fig. 22) may indicate changing water level (low- and high-stand) or erosion caused by the sedimentological processes activity.

Samples from the cross-stratified sandstone contain close to 50% of calcite (Fig. 37). The origin of the large amounts of the carbonate cement is problematic. Almost 50% of calcite in the rock samples may suggest early diagenese.

The cross-stratified sandstone with calcite cement may represents a cemented carbonate beach (Binkley et al., 1980). Calcite is the most commonest lacustrine carbonate mineral (Reading, 1996). Deposition of chemically formed sediments is particularly common in closed lakes (Binkley, 1964). The newly formed Ritland crater was most likely an isolated lacustrine environment. The pH lake depends on factors such as: a contribution from drainage-basin run-off, aerosols and the balance between evaporation and precipitation (Kelts, 1988). Relatively high pH conditions can be achieved by evaporative concentration of waters derived from the chemical weathering of many common rock types (after Eugster, 1970; Livingstone and Melack, 1984). White et al. (1999) experimentally proved that vital amounts of calcite can be expelled from the fresh granitic rocks due to weathering. One of the example is Lake Chad in Africa. Dissolved ions are derived from the weathering of granitic rocks (Maglione, 1980). This may favor the beach sediment cementation.

Many authors (e.g. Binkley and Wilkinson, 1980; Vieira, Sial and De Ros, ????) describe a beachrock cementation. They proposed few mechanisms favor such cementation: evaporation of ground water in arid climates (Ginsburg, 1953; Russel, 1962) or degassing of carbone dioxide from ground water (Hanor, 1978 *In* Binkley and Wilkinson, 1980). Carbonate precipitation may also be caused by heating lake water, leading to carbonate supersaturation (Brunskill, 1969). Guerra and Sial (????) claim “High temperatures and rates of evaporation on the beach evidently create ideal environments for inorganic carbonate precipitation just below the sediment/water interface”.

Beach rock cementation demand special conditions both geochemical and sedimentological. The clastic sediments supply has to be low, then chemical processes predominate. Carbonates precipitation may takes place. A rapid and constant sedimentation in the first phase of deposition, where steep crater walls and large amount of newly excavated impact material favor gravity-controlled sedimentation, prevented chemical processes in the Ritland structure.

In the massive sandstone (facies V), overlying the calcite cemented sandstone (see Fig. 10), fractures filled with calcite were found (Fig. 31/B2). Carbonates have also been found in other facies (in suevite – Fig. 28A, in sedimentary breccia Fig. 32/A1), but in minor amounts

(Fig. 37). Calcite cementation may take place during all stages of lithification from early to late once and deep burial. To achieve this e.g. pore water highly oversaturated in calcium carbonate, preferable high porosity and permeability successions, increase in temperature, and decrease in carbon dioxide partial pressure (Friedman, 1964). Carbonate cement from the burial alteration consists of coarse mosaics of calcite and bladed prismatic calcite (Boggs, 2006). It reflects the petrographical properties of samples from the facies VI (Fig. 31A). In the Ritland case the carbonates source could be younger sediments, deposited above (e.g. Silurian-Devonian). A large amount of carbonates were deposited in shallow seas covering “Norway” during the Cambrian-Silurian, when life on the Earth has exploded (Ramberg eds., 2008). During burial history calcite from the Silurian-Devonian sedimentary rocks was dissolved, subsequently migrating through fracture networks to the rocks buried below.

A further detailed petrographic and isotopic analysis of the sandstone with calcite cement has to be done to determine the origin of these deposits and to identify processes responsible for their early? diagenetic alteration.

### **8.2.3 Massive sandstone**

The massive beds are well laminated sandstone (Fig. 19A). These beds are massive and very thick, comparing to the others (RITF-4, see Fig. 12). The massive sandstones appear comparable to the dense flows deposits (Gani, 2004). The dense flows (after Allen, 1997) are intermediate flow types between debris flow and turbidity current. Various flow names have been proposed in explaining the depositional mechanism of dense flow deposits (Fig. 42). Mulder and Alexander (2001) described them as the concentrated density flows, where flow is sufficient to allow particle fall-out within the flow, in order to sort sediment during the flow. These flows are more diluted than the hyperconcentrated flows (grain flow). Mulder and Alexander (2001) emphasize that it is difficult to differentiate the deposits of hyperconcentrated and concentrated density flow (dense flow according to Gani, 2004). They should be different, but one may evolve into the other with distance and height. According to Mulder and Alexander (2001) the concentrated density flows may be subdivided into surge, surge-like and quasi-steady concentrated density flows. The quasi-steady density current (dense flow according to Gani, 2004) is a term used by Kneller and Branney (1995). The quasi-steady density flows deposits characterize thick divisions of massive (unstratified) sand, generally lacking normal grading. In these massive beds the traction structures does not occur (Kneller and Branney, 1995). The description of concentrated density flows deposits fits well with the thick and massive sandstone beds of facies V in the Ritland structure.

Succession of gravity flows were carrying downslope the Ritland crater a huge amount of sediments into the crater lake. The concentrated density flow impacted into a fresh water body forming a dense underflow current (a hyperpycnal current). The rapid flow expansion and convection of fresh water (low-density) resulted fast decline in transport and rapid sediment deposition (Kneller and Branney, 1995; Mulder and Alexander, 2001). These currents have short run-out distances from the stream mouth, but their deposits can be thicker than the current length (Kneller and Branney, 1995). The massive sandstone units found in the Ritland structure may represent deposit of such currents. A rapid current deposition leads to forming water escape structures (Kneller and Branney, 1995). The structures were not found in the massive sandstone in Ritland.

Increasing fluid content ↑	Rheology	Flow Type		Deposits		Dominant sediment support mechanism
	Newtonian fluid	<b>Turbidity current</b> (mostly turbulent)	Subcategories: - Low-concentration (<1%) & muddy (e.g., fluid mud ?) - Low-concentration (0.2-3%) & medium-grained (Hyperpycnal flow: Mulder et al., 2003) - Low-concentration & fine-grained (Stow & Shanmugam, 1980) - Medium-grained classic (Bouma, 1962)	<b>Turbidite</b>	<b>Gravite</b> (Gani, 2003)	Fluid turbulence
	Variable (Partly non-Newtonian fluid, partly Newtonian fluid)	<b>Dense flow</b> (partly laminar, partly turbulent)	Variously named as: - High-density turbidity currents (Lowe, 1982) - Sandy debris flows (Shanmugam, 1996) - Slurry flows (Lowe & Guy, 2000) - Concentrated density flows (Mulder & Alexander, 2001) - Liquefied flows /fluidized flows	<b>Densite</b> (This study)		Dispersive grain pressure, fluid turbulence, escaping pore fluid, matrix strength
	Non-Newtonian dilatant fluid	<b>Debris flow</b> (mostly laminar)	Non-cohesive debris flow (e.g., grain flow)	<b>Debrite</b>		Dispersive grain pressure
	Bingham plastic		Cohesive debris flow			Matrix strength
	Bingham plastic	Slide and slump				Slide and slump deposits

**Figure 42.** Classification of sediment gravity flows with a nomenclature for the flow types and their deposits. Direction of increasing fluid content reflects the down-slope development of sediment gravity flows (Figure from Gani, 2004).

A large object, boulder is present in one of the bed of facies V (Fig. 16C). In debris flows large clasts may be pushed along by density flow (Johnson, 1970). Such process may explain the position of the large clast, stuck within the sandstone unit of facies V. This boulder was found along the strike of the conglomerate channel, consequently Johnson's description may be answer the problem of this isolated boulder within the sandstone. Another explanation is a large, single clast may slides downslope, from e.g. rock avalanche talus into fine-grained deposit, being preserved as olistolith, isolated within basinal sandstone (e.g. Anadon, Cabrera et al., 1991; Tiercelin, Soreghan et al., 1992; Renaut and Tiercelin, 1994).

The steep crater slope favor rapid transfer sediments to the basin floor. The large boulder is located quite steep at the rim, not far from rock avalanche deposits above.

The middle sedimentary succession is associated with the upper succession. Quartz/feldspar ratios show some variable trends in the facies associations (Fig. 34). The trend in the FA3 is slightly varying to constant and FA2 show the upwards decreasing quartz/feldspar ratio (seen in both XRD analyses and thin section point counting). These changes reflect transition of rock avalanches (sedimentary breccia) into debris flows (conglomerate) in the Ritland structure (Hampton, 1972). Fine-grained, laminated sandstones from the middle succession were generated by conglomerates (Mulder and Alexander, 2001)(Fig. 44/3). Material was subsequently reworked during succession of different gravity flows. More resistant to erosion quartz has higher amount further from crater margin, in fine-grained sediment deposited from suspension.

### **8.3 Upper succession – conglomerate sub-unit and sedimentary breccia**

The upper succession is build-up of the rock slides and rock avalanches in topographically high elevations along the crater rim. This succession represents the facies association 3.

#### **8.3.1 Conglomerate**

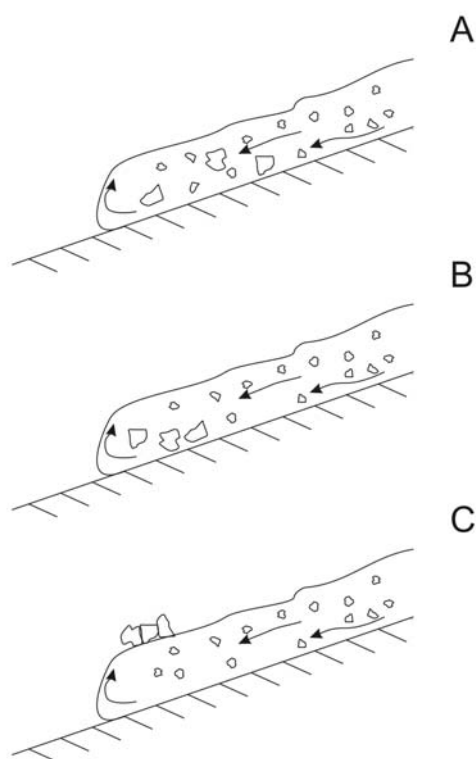
Conglomerates which contains subrounded cobbles in laminated matrix (Fig. 18A and 18C). The clasts within matrix have subrounded shape. This facies contains 5 % of a matrix (Appendix 3). Conglomerates display erosional contact towards underlying sandstone units (Fig. 25).

This facies is characterized by poor sorting with rare, if any, coarse-tail grading, sharp upper boundary and boulder projecting through the top (Fig. 18A and 23). In the field the conglomerate units look like “frozen” packages of poorly sorted clasts within the matrix (Fig. 23). The conglomerates correspond to deposition description of cohesive debris flow (Mulder and Alexander, 2001; Gani, 2004). Debris flow are controlled by frictional force which is connected to a pore pressure. The frictional flow needs sufficient amount of clay or steeper slope to generate flow. Conglomerate of facies association 3 contains minor amount of clay minerals (Fig. 35), but a surprisingly small amount of clay, less than 10 % of the total solids, is sufficient for complete support of sand-size material in a debris flow (Hampton, 1970, 1972). In addition granular solids within the flow collide with one another producing a dispersive pressure (Bagnold, 1956 *In* Hampton, 1972). All these factors help to support grains, in order



to keep debris flow movement. During debris flow progradation the shear stress decreases against the yield strength of the base of the flow due to the gravity force. The mass stops and “freezes” (Mulder and Alexander, 2001).

Large angular, clasts (up to 30 cm) sit on the top of conglomerates, stuck together (Fig. 23). The clasts are granite-gneissic rock fragments. Due to the cohesive behavior of the flow these clasts could ‘ride’ on a debris flow carpet (Kalleson et al., 2008). Another explanation is the physics of debris flow. The front of debris flow proceeds in “rolling” motion (Iverson, 1997). Large clasts within debris flow are transported in front due to increase of frictional strength (Mulder and Alexander, 2001). Larger clasts “stucked” in the front could be uplifted and settle on the top of the flowing debris flow (Fig. 43). Jahns (1949) and Johnson (1970) performed similar observations.



**Figure 43.** The figure shows how larger clasts within debris flow behave. Due to increase of frictional strength the front of debris flow proceeds in rolling motion (A). Larger clasts are “pushed” into the front (B), subsequently uplifted at the debris flow “back” (C).

Samples taken from the conglomerates of facies mineralogical composition reflecting the local bedrock (Fig. 35), in addition coarse-grained particles of feldspar and quartz have angular shape indicating short transport distance for these particles.

According to Iverson (1997) “debris flows occur when masses of poorly-sorted sediment, agitated and saturated with water, surge down slopes in response to gravitational attraction”.

During transgression the incoming water ran down the crater rim, causing further collapse. Flash water may erode gullies in the crater wall. Continuous flow of water into the crater could widen and deepen these inlets, leading to repeated rim collapse and renewed activity in the gullies. Enormous amount of debris spread out downslope, farther to the crater center (Kalleson et al., 2008).

### **8.3.2 Conglomeratic sandstone**

The conglomeratic sandstone characterizes lack of grain size grading (Fig. 33A) or bed forms, convolute lamination was found at the contact with conglomerate bed (Fig. 23). The conglomerate sandstone units consist of grains in average size of 0,2 mm. Grains have angular to subangular shape, weakly sorted. This facies has higher content of matrix (10 %) than conglomerate of facies I (Appendix 3). The shift from matrix supported conglomerates (facies I) to the conglomeratic sandstones (facies IV) may correspond to change from cohesive to noncohesive flow (Gani, 2004). This textural description of conglomeratic sandstone in Ritland matches to the sediments carried/deposited by hyperconcentrated density flows – non-cohesive flow (Mulder and Alexander, 2001; Gani, 2004).

In hyperconcentrated flows convolute lamination occurs in the conglomeratic sandstones. Facies IV is associated with conglomerate beds (Fig. 13 and 23). The sandstone of facies III could be deposited by the density flow, transformed earlier from debris flow.

Hyperconcentrated density flows deposits represent none-graded or normally graded gravel or gravelly sand or thick stratified sand deposits (cf. Pierson and Scott, 1985; Best 1992), possibly containing collapse and deformation structures (Lowe and Guy, 2000). This descriptions fit well to the conglomeratic sandstone of facies IV.

### **8.3.3 Soft sediment deformed sandstone**

The soft sediment deformed sandstone is stratified sandstone, waning flow deposit (Fig. 12 and 18B). This medium grained sandstone display a convolute lamination. When coarse-grained material of the debris flows settle down, a stream flow may continue from upper part of the debris flow deposits, partly reworked the upper part.

The convolute lamination may be caused by plastic deformation of partially liquefied sediment soon after deposition (e.g. Siebe, Komorowski and Sheridan, 1992). This may

formed a convolute lamination in newly deposited package of sediments. Boggs (2006) suggested “the axes of some convoluted folds have a preferred orientation which commonly coincides with the paleocurrent direction, suggesting that the process that produces convolutions occurs during deposition”. The axes of the convoluted fold in sandstone of facies III ( $225^0$ ) is different then the axes of overlying conglomerate units ( $265-270^0$ ) (Fig. 26). It may be represented by many separate depositional systems with different direction of deposition in the Ritland structure.

#### **8.3.4 Matrix supported sedimentary breccia**

The matrix supported breccia (facies IIb) is composed of subangular to subrounded grains derived from the crystalline basement, with higher content of matrix than clast supported breccias (facies IIa). This change occurs as the result of the apparent mechanical formation of matrix due to clast crushing and grinding of angular granitic boulders during downslope avalanche movement (Kessler and Bédard, 2000). Prograding rock fall not only slide or fall but also flow (Heim, 1932). Many authors describe process of transition from rock avalanche into debris flow (Hsü, 1975; Kessler and Bédard, 2000; Hungr and Evans, 2004). Facies IIa represents shift from rock avalanche into debris flow.

In both matrix- and clast-supported breccia matrix lamination occur (Fig. 32B). Water filling the structure during transgression carried fine-grained material, percolating porous rock avalanche deposits. A rockslide mass may disintegrate and develop to become a rock avalanche, with initial volume increase (Hungr and Evans, 2004). The volume increase could range from 7 % to 26 % (Hungr, 1981). The newly created pore space could then be filled up by subsequent mass flows deposits. The microscopic investigation of matrix sample from the rock avalanche deposits reveals features indicating specific flow pattern in the matrix (Fig. 32B). The incoming water during transgression favors the sheet flood transport sediment in suspension and as bedload. This could trigger debris flows and turbidity currents (Rahn, 1967). The loose rock debris of the rock avalanche deposits were infilled by fine-grained material, and form discrete lobe, a so-called sieve deposit (Hooke, 1967). Such lobes can have sharply defined downstream margins, as well tend to develop during the earliest stages of a transgression (Wasson, 1974).

#### **8.3.5 Clast supported sedimentary breccia**

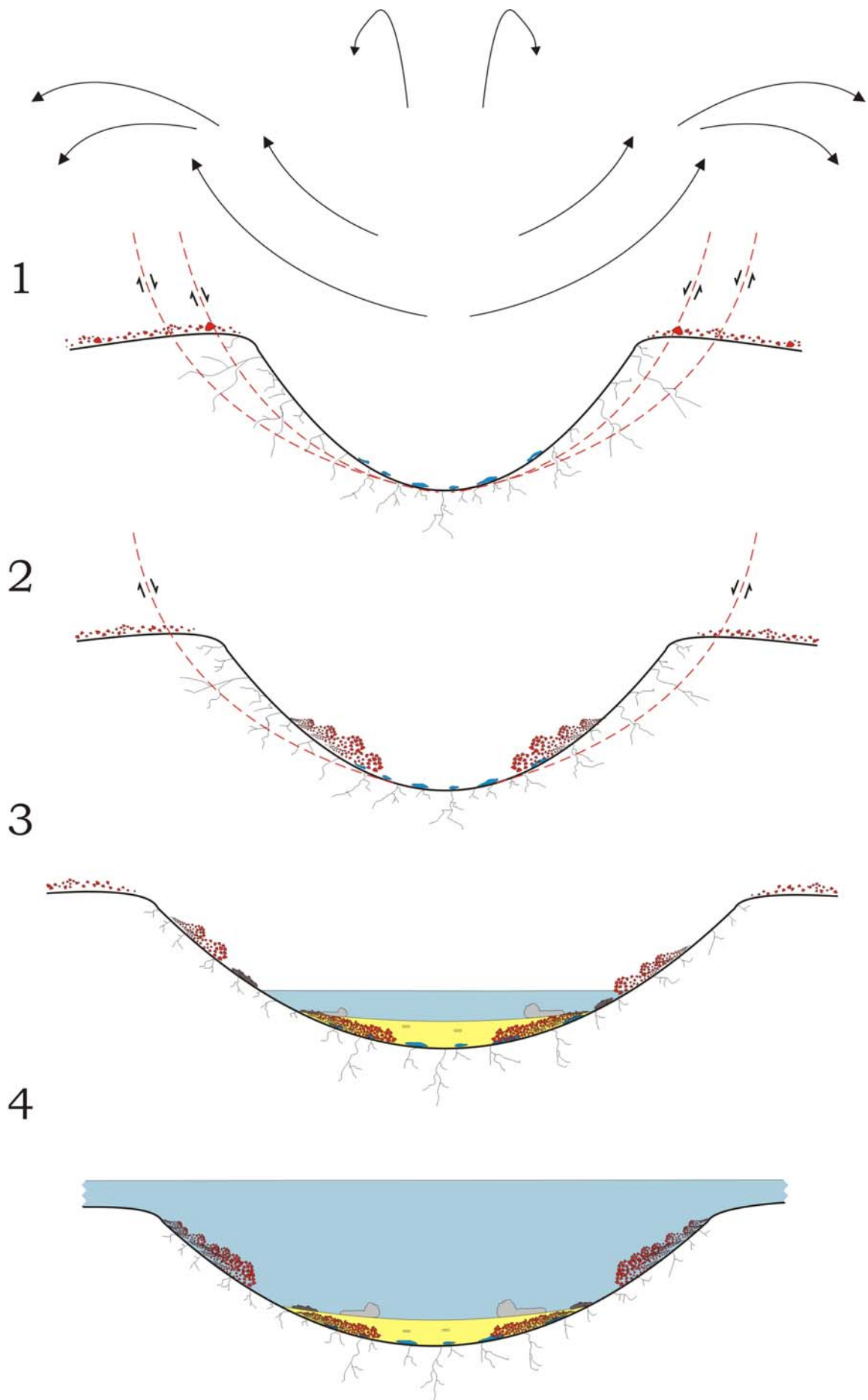
Breccias of facies IIa have angular matrix grains and subangular to subrounded clasts, with minor amount of matrix. It indicates a short-distance transport. The clasts consist of the

as the basement lithologies. These breccias have similar composition and morphology to the breccia at the base (facies VIII).

The absence of clay minerals shows that breccia at the base is freshly crushed and consists of unweathered rock. Deposition of this facies took place most likely in subaerial conditions. Absence of iron oxides is the result of rapid deposition of the rock avalanche deposits. The rock avalanches according to Kessler and Bédard (2000) are large rock masses moving rapidly downslope, generating poorly sorted deposits. The clasts are angular-shaped particles as a mixture of megablocks, boulders, cobble-size fragments and gravel. Clast supported breccia may represent rock avalanche deposit. Breccias of facies IIb could be formed during transgression, when vast amount of water put pressure on the uplifted crater rim, causing its collapse. The wide distribution of avalanche deposit reflects several local avalanches, developing a moreover continuous apron (Kalleberg, 2008).

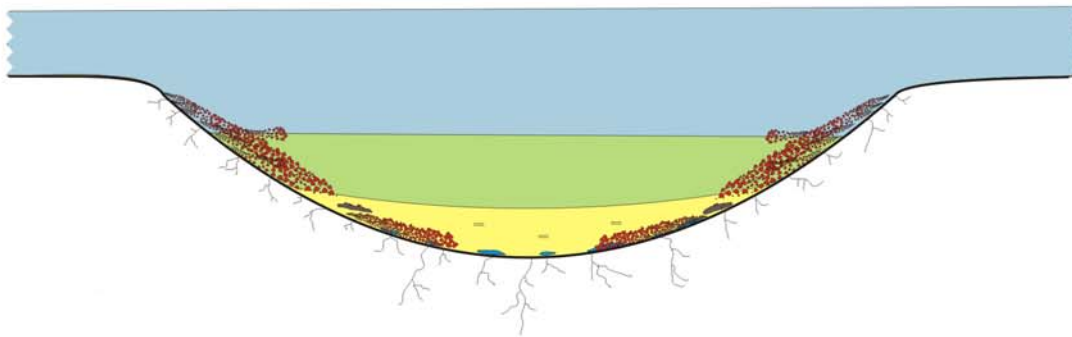
Quartz/feldspar ratios in the FA3 is slightly varying to constant. Rock avalanche deposits built up the upper succession. Clast supported breccia interfinger with matrix supported breccia. These two facies are differentiated in the XRD analysis data (Fig.37). Breccias with larger amount of matrix contain more biotite (samples: RITF-3-5-09 and RITF-3-3-09). The 3D models show succession of these two different breccias in the Svodene hill, in Ritland (Fig. 38 and 39). In upper part of outcrop clast supported breccia seems to have weathered surface. The matrix supported breccia have smooth surface, seen in outcrop. It can be related to different matrix cementation. These breccia beds dipping at angle 24 degrees, towards crater center.

The deposition model of complete post-impact sedimentation in the Ritland structure is presented in Figure 44.

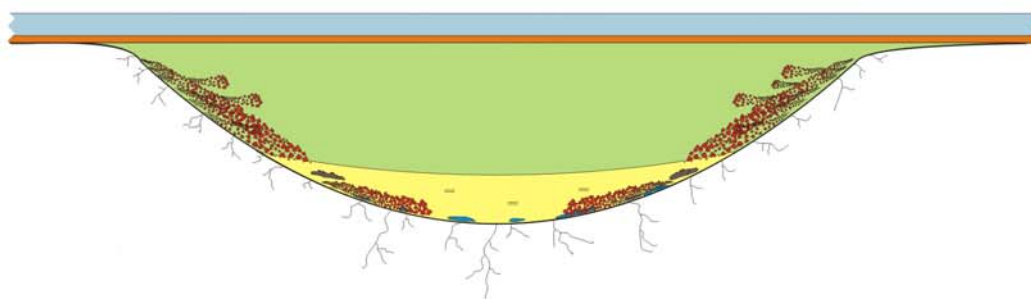




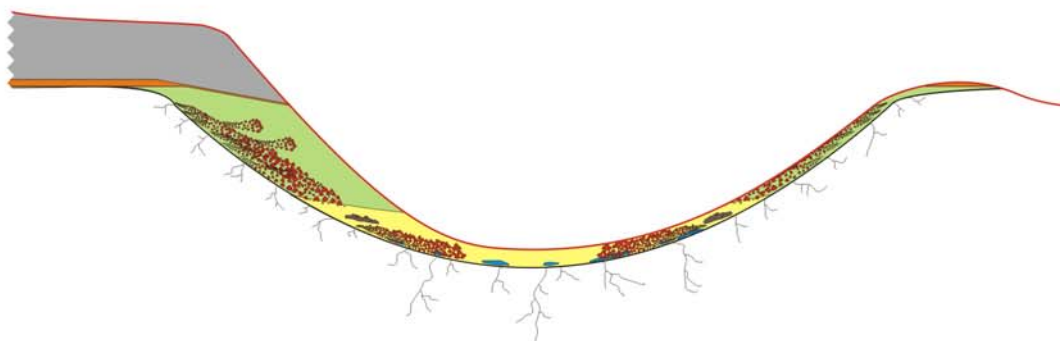
5








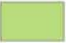







6



7



## Legend

- |   |                        |   |   |
|---|------------------------|---|---|
|  | Melted rocks (suevite) |  | Crater lake, alluvial, turbiditic current, debris flow deposits |
|  | Turbidities            |  | Shallow marine deposits   |
|  | Rock avalanche deposit |  | Deep marine deposits  |
|  | Debris flow deposit    |  | Water   |
|  | Clasts                 |  | Caledonian nappes   |
|  | Lamination             |   |   |
|  | Erosional surface      |   |   |
|  | Failure surface        |   |   |

**Figure 44.** The deposition model of post-impact sedimentation in the Ritland structure reveals a shifting depositional environments. 1) During the excavation stage development of melt took place, at the crushed basement. Seconds after impact the newly excavated material was moving outwards and inwards from the crater. At the end of stage transient cavity reached maximum extent, and uplifted crater rim was developed; 2) At the begin of the modification stage steep crater walls collapsed along failure planes – red, dash lines (up to 100 sec when it happened) producing rock slides and rock avalanches; 3) Crater lake formation, successive rim failures produced more rock avalanches, generating conglomerates. Cohesive flows along crater rim were transformed into non-cohesive flows in aquatic environment, as a result sediments from suspension were deposited; 4) Water covered whole structure during transgression. Incoming water triggered crater rim collapses. Rock avalanche succession was repeated, with the next generation of other gravity flows (e.g. debris flow). Sand-enriched density flows then dominated in the water-filled crater basin; 5) Shales, representing the reestablishment of quite conditions, were depositing. Single rock avalanches eroded into the fine-grained sediment; 6) The water level may slightly drop. A package of shallow marine sandstone was deposited; 7) Crater infill suffered several uplifts. During Caledonian orogeny thrust nappes covered sediments in the structure. Finally, due to glaciations part of crater infill was eroded by glacier.

## 9 Conclusions

A fresh impact structure forms an extreme depositional succession. The sedimentary succession in the Ritland structure reveals a shifting depositional environments. Enormous amount of excavated impact rocks have been transported and deposited by various deposition processes. In the impact process the accommodation space was created in seconds. Just after a bolide 100 metres in diameter hit the peneplain the kinetic energy was transferred into the basement. This stage of impact structure development is called the contact/compression stage.

During the successive stage, the excavation stage, development of melt took place at the crushed basement. Seconds after impact the newly excavated material was moving outwards and inwards from the crater. At the end of this stage transient crater reached maximum extent, and uplifted crater rim was developed.

At the begin of the last stage of crater-forming – the modification stage – steep crater walls collapsed after approximately 100 seconds after impact, producing rock slides and rock avalanches. “Pyroclastic rain” and rim collapse were the first processes which fed the crater space. Material stored on and along a slope was moving down due to gravity. Steep crater walls favor gravity-controlled sedimentation. The very first gravity-controlled sedimentary processes like rock avalanches, were triggered by the crater rim failure. This marks the start of the crater fill. Gravity-flow deposits were mixing with melt rocks and ejecta falling into the crater.

After a relatively long period of time (years, dozens of years) the crater lake was formed due to precipitation and groundwater percolation from the crushed basement. Low angle

cross-stratification may form during high-water, where the edges of sandflats were reworked by wave action, resulting in redeposition of low angle cross-stratified sandy sediments along coastal areas of the lake. Successive rim failures produced rock avalanches generating conglomerates. Cohesive flows (debris flows) along crater rim were transformed into non-cohesive flows in an aquatic environment, as a result sediment were deposited from suspension. Turbidity currents generated by debris flow were present in the small basin, in the Ritland impact structure.

During the Cambrian transgression the crater was filled up with sea water. Incoming water breached the crater wall, initiating series of rock avalanches and debris flows. Sand-enriched density flows then dominated in the water-filled crater basin.

Shales, representing the reestablishment of quiet conditions, were deposited in the Ritland crater. Single rock avalanches eroded into the fine-grained sediment. The water level may slightly drop, then a package of shallow marine sandstone was deposited overlying shale succession.

During burial history the sedimentary infill of the crater was affected by a low-grade metamorphic conditions. Products of low-grade alteration are present in sediments in Ritland (e.g. actinolite, chlorite). Most likely carbonates present in crater infill have late diagenetic origin. The source of carbonates could be in younger sediments (e.g. Silurian-Devonian). During burial history carbonates from the Silurian-Devonian sedimentary rocks were dissolved, subsequently migrate through fracture networks to the rocks buried below.

Since Paleozoic times, crater infill has suffered several uplifts. During Caledonian orogeny thrust nappes covered crater infill. Finally, due to glaciations part of crater infill was eroded by glaciers.

## REFERENCES

- Atkinson H.H., Tickell C., and Williams D.A., 2000, Report of Task Force on Potentially Hazardous Near Earth Objects, British National Space Centre, London, accessed on: 15th April 2010:  
<http://www.nearearthobjects.co.uk>
- Alvarez, L.W., Alvarez, W., Asaro, F., and Michel, H.V., 1980, Extraterrestrial cause for the Cretaceous–Tertiary extinction, *v. 208*, p. 1095–1108.
- Bagnold, 1957 *In* Hampton, M.A., 1972, The role of subaqueous debris flow in generating turbidity currents, *Journal of Sedimentary Petrology*, *v. 42*, p. 775-793.
- Bellian, J.A., Kerans, C. and Jennette, D.C., 2005, Digital Outcrop Models: Applications of Terrestrial Scanning Lidar Technology in Stratigraphic Modeling, *Journal of Sedimentary Research*, *v. 75*, p. 166-17.
- Bernard, H. A., Major, C. F. and Parrott, B. S., 1999, Shell report: sand facies and their environments in NV Gulf of Mexico, Search and Discovery Article, GEOLOGICAL MISCELLANEOUS.
- Bhattacharya, J.P., and MacEachern, J.A., 2008, Hyperpynal Rivers and Prodeltaic Shelves in the Cretaceous Seaway of North America, Search and Discovery Article.
- Bingen, B., Nordgulen, Ø., and Viola, G., 2008, A four-phase model for the Sveconorwegian orogeny, SW Scandinavia, *Norwegian Journal of Geology*, *v. 88*, p. 43-72.
- Binkley, K.L., and Wilkinson, B.H., Owen, R.M., 1980, Vadose beach rock cementation along a southeastern Michigan marl lake, *v. 50*, no. 3, p. 0953-0962.
- Boggs, S., Jr., 2006, *Principle of Sedimentology and Stratigraphy*, Pearson Education, Inc., New Jersey, pp. 623.
- Bohor, B.F., Foord, E.E., Modreski, P.J., and Triplehorn, 1984, D.M., Mineralogic Evidence for an Impact Event at the Cretaceous-Tertiary Boundary, *Science*, *v. 224*, p. 867–869.
- Brown, P., Spalding, R.E., ReVelle, D.O., Tagliaferri E., and Worden, S.P., 2002, The flux of small near-Earth objects colliding with the Earth, *Nature* *v. 420*, p. 294-296.
- Buckley, S.J., Howell, J.A., Enge, H.D., and Kurz, T.H., 2008, Terrestrial laser scanning in geology: data acquisition, processing and accuracy considerations, *Journal of the Geological Society*, *v. 165*, p. 625-638.
- Buckley, S.J., Vallet, J., Braathen, A., and Wheeler, W., 2008, Oblique helicopter-based laser scanning for digital terrain modelling and visualisation of geological outcrops. *International Archives of the Photogrammetry, Remote Sensing and Spatial Information Sciences*, *v. 37*, p. 493-498.
- Dressler, B.O., Sharpton, V.L., 1997, Breccia formation at a complex impact crater: Slate Islands, Lake Superior, Ontario, Canada, *Tectonophysics*, *v. 275*, p. 285-311.

- Dressler, B.O., Reimold, W.U., 2001, Terrestrial impact melt rocks and glasses, *Earth-Science Reviews*, v. 56, p. 205-284.
- Dypvik, H., Jansa, L.F., 2003, Sedimentary signatures and processes during marine bolide impacts: a review, *Sedimentary Geology*, v. 161, p. 309-337.
- Dypvik, H., Sandbakken, P.T., Postma, G., Mørk, A., 2004, Early post-impact sedimentation around the central high of the Mjølnir impact crater (Barents Sea, Late Jurassic), *Sedimentary Geology*, v. 168, p. 227-247.
- Dypvik, H., Smelror, M., Sandbakken, P.T., Salvigsen, O., Kalleson, E., 2006, Traces of the marine Mjølnir impact event, *Paleogeography, Paleoclimatology, Paleoecology*, v. 241, p. 621-636.
- Earth Impact Database, accessed on: 15th April 2010,  
<http://www.unb.ca/passc/ImpactDatabase/>
- Folk, R.L., 1974, *Petrology of Sedimentary Rocks*, Hemphill Publishing Co., 182pp.
- Fossen et al., 2008 *In* Ramberg, I.B., Bryhni, I., Nottvedt, A. & Rangnes, K. (eds), 2008, *The Making of a Land: Geology of Norway*, Geological Society of Norway, 640pp.
- French, B.M., Koeberl, Ch., Gilmour, I., Shirey, S.B., Dons, J.A. and Naterstad, J., 1997, The Gardnos impact structure, Norway: Petrology and geochemistry of target rocks and impactites, *Geochimica et Cosmochimica Acta*, v. 61, p. 873-904.
- French, B. M., 1998. *Traces of Catastrophe: A Handbook of Shock-Metamorphic Effects in Terrestrial Meteorite Impact Structures*. Lunar and Planetary Institute, Houston, pp. 120.
- Gani, M.R., 2004. From Turbid to Lucid: A Straightforward Approach to Sediment Gravity Flows and Their Deposits. *The Sedimentary Record*, v. 2, no. 3, p. 4-8.
- Goguel and Pachoud, 1972 *In* Hungr, O., Evans, S.G., 2004, Entrainment of debris in rock avalanches: An analysis of a long run-out mechanism, *Geological Society of America Bulletin*, v. 116, p. 1240-1252.
- Grieve, R.A.F., Pesonen, L.J., The terrestrial impact cratering record, *Tectonophysics*, v. 216, p. 1-30.
- Grieve, R.A.F., Langenhorst, F., Stöffler, D., 1996, Shock metamorphism of quartz in nature and experiments: II. Significance in geoscience, *Meteoritic & Planetary Science*, v. 31, p. 6-35
- Grieve, R.A.F., 1997, Extraterrestrial impact events: the record in the rocks and the stratigraphic column, *Paleogeography, Paleoclimatology, Palaeoecology*, v. 132, p. 5-23.
- Hampton, M.A., 1972, The role of subaqueous debris flow in generating turbidity currents, *Journal of Sedimentary Petrology*, v. 42, p. 775-793.



- Hanor, 1978 *In* Binkley, K.L., and Wilkinson, B.H., Owen, R.M., 1980, Vadose beach rock cementation along a southeastern Michigan marl lake, v. 50, no. 3, p. 0953-0962.
- Heim, 1932 *In* Hsü, K.J., 1975, Catastrophic debris streams (sturzstroms) generated by rockfalls, Geological Society of America Bulletin, v. 86, p. 129-140.
- Henningsmoen 1952, Bruton and Harper 2000 *In* Riis, F., Dypvik, H., Krøgli, S.O., Nilsen, O., 2009, The Ritland impact structure, SW Norway, Meteorite and planetary sciences.
- Hildebrand, A.R., Penfield, G.T., Kring, D.A., Pilkington, M., Camargo, A., Jacobsen, S.B., and Boynton, W.V., 1991, Chicxulub Crater: A possible Cretaceous/Tertiary boundary impact crater on the Yucatán Peninsula, Mexico, *Geology*, v. 19, p. 867-871.
- Howard, K.A., and Wilshire, H.G., 1975, Flows of impact melt at lunar craters, *J. Re. U.S. Geol. Survey* 3, p. 237-251.
- Hsü, K.J., 1975, Catastrophic debris streams (sturzstroms) generated by rockfalls, Geological Society of America Bulletin, v. 86, p. 129-140.
- Hungr, O., Evans, S.G., 2004, Entrainment of debris in rock avalanches: An analysis of a long run-out mechanism, Geological Society of America Bulletin, v. 116, p. 1240-1252.
- Kalleson, E., Dypvik, H., Naterstad, J., 2008, Postimpact sediments in the Gardnos impact structure, Norway, *The Geological Society of America*, v. 437, p. 19-41.
- Kessler, L.G., Bédard, J.H., 2000, Epiclastic volcanic debrites-evidence of flow transformations between avalanche and debris flow processes, Middle Ordovician, Baie Verte Peninsula, Newfoundland, Canada, *Precambrian Research*, v. 101, p. 135-161.
- Kneller, 1995 *In* Mulder, T., Alexander J., 2001, The physical character of subaqueous sedimentary density flows and their deposits, *Sedimentology*, v. 48, p. 269-299.
- Koeberl, C., 2007, The geochemistry and cosmochemistry of impacts, *Treatise on Geochemistry*, v. 1, p. 1-52.
- Langenhorst, F., Deutsch, A., 1993, Orientation of Planar Deformation Features (PDFs) in quartz, *In* Lunar and Planetary Inst., Twenty-Fourth Lunar and Planetary Science Conference, p. 849-850.
- Maglione, 1980 *In* Reading, H. G., 1996. *Sedimentary Environments: Processes, Facies and Stratigraphy*. Blackwell Science Ltd, Oxford, pp. 407-516.
- Margolin, P., 2000, The Making of Lunar Explorers, *Newsmagazine of the Earth Sciences*, the American Geological Institute: 9th April 2010.  
<http://www.geotimes.org/aug00/lunarfeature.html>
- Mather, P.M., 2004, Computer processing of remotely-sensed images : an introduction, Chichester Edition: 3rd ed. Pages: XVII, p. 281-292.

- McBride et al., 1975 *In* Stow, D.A.V., and Shanmugan, G., 1980, Sequence of structures in fine-grained turbidites: comparison of Recent deep-sea and ancient flych sediments: *Sed. Geol.*, v. 25, p. 23-42.
- Meert, J.G, Torsvik, T.H., 2004, Paleomagnetic Constraints on Neoproterozoic 'Snowball Earth' Continental Reconstructions, Jenkins, G.S., McMenamin, M.A.S, McKey, C.P., and Sohl, L., (Editors), *the Extreme Proterozoic: Geology, Geochemistry, and Climate*, American Geophysical Union Geophysical Monograph v. 146, p. 5-11.
- Melosh, 1989 *In* Hildebrand, A.R., Penfield, G.T., Kring, D.A., Pilkington, M., Camargo, A., Jacobsen, S.B., and Boynton, W.V., 1991, Chicxulub Crater: A possible Cretaceous/Tertiary boundary impact crater on the Yucatán Peninsula, Mexico, *Geology*, v. 19, p. 867-871.
- Melosh, H.J., Ivanov, B.A., 1999, Impact crater collapse, *Annual Review of Earth and Planetary Science*, v. 27, p. 385-415.
- Middleton, 1966 *In* Hampton, M.A., 1972, The role of subaqueous debris flow in generating turbidity currents, *Journal of Sedimentary Petrology*, v. 42, p. 775-793.
- Mulder, T., Alexander J., 2001, The physical character of subaqueous sedimentary density flows and their deposits, *Sedimentology*, v. 48, p. 269-299.
- Nelson, C.H., Meyer, A.W., Thor, D. and Larsen, M., 1986, Crater Lake, Oregon: A restricted basin with base-of-slope aprons of nonchannelized turbidites, *Geology*, v. 14; no. 3; p. 238-241.
- Nordgulen and Andresen, 2008 *In* Ramberg, I.B., Bryhni, I., Nottvedt, A. & Rangnes, K. (eds)., 2008, *The Making of a Land: Geology of Norway*, Geological Society of Norway, 640pp.
- Onorato, P.I.K., Uhlmann, D.R. and Simonds, C.H., 1978, The thermal history of the Manicouagan impact melt sheet, Québec, *J. Geophys. Res.* 83 p. 2789-2798.
- Petschick, 2001, *Manual: Macdiff 4.2.5*.
- Pohl, J., Stöffler, D., Gall, H., Ernestson, K., 1977, The Ries impact crater, *Impact and Explosion Cratering*, p. 343-404.
- Puura, V., Suuroja, K., 1992, Ordovician impact crater at Kärđla, Hiiumaa Island, Estonia, *Tectonophysics*, v. 216, p. 143-156.
- Rahn 1967 *In* Reading, H. G., 1996. *Sedimentary Environments: Processes, Facies and Stratigraphy*. Blackwell Science Ltd, Oxford, pp. 407-516.
- Reading, H. G., 1996. *Sedimentary Environments: Processes, Facies and Stratigraphy*. Blackwell Science Ltd, Oxford, pp. 407-516.

- Riis, F., Dypvik, H., Krøgli, S.O., Nilsen, O., 2009, The Ritland impact structure, SW Norway, *Meteorite and planetary sciences*.
- Settle, M., Head III, J.W., 1979, The role of rim slumping in the modification of lunar impact crater, *Journal of Geophysical research*, v. 84, p. 3081-3096.
- Shoemaker, E. M., 1963, Impact mechanics at Meteor Crater, Arizona. In: Middlehurst, B. and Kuiper, G. P. (eds) *The Moon, Meteorites, and Comets — The Solar System*, University of Chicago Press, p. 301–336.
- Stow, D.A.V., and Shanmugan, G., 1980, Sequence of structures in fine-grained turbidites: comparison of Recent deep-sea and ancient flysch sediments: *Sed. Geol.*, v. 25, p. 23-42.
- Stow, 1985; Pickering, Stow et al., 1986 *In* Reading, H. G., 1996, *Sedimentary Environments: Processes, Facies and Stratigraphy*, Blackwell Science Ltd, Oxford, p. 407-516.
- Stöffler, D., Bischoff, A., Buchwald, U., and Rubin, A.E., 1988, Shock Effects in Meteorites, in J.F. Kerridge and M.S. Matthews (eds.), *Meteorites and the Early Solar System*, Univ. Arizona Press, Tucson, p. 165-205.
- Sturm and Matter, 1978; Kelts and Hsu, 1980; Lambert and Giovanoli, 1988 *In* Reading, H. G., 1996. *Sedimentary Environments: Processes, Facies and Stratigraphy*. Blackwell Science Ltd, Oxford, pp. 407-516.
- Suuroja, K., Suuroja, S., All, T., Floden T., 2002, Kärđla (Hiiumaa Island, Estonia) – the buried and well-preserved Ordovician marine impact structure, *Deep-Sea Research II*, v. 49, p. 1121-1144.
- Tanner, 2003 *In* Kalleson, E., Dypvik, H., Naterstad, J., 2008, Postimpact sediments in the Gardnos impact structure, Norway, *The Geological Society of America*, v. 437, p. 19-41.
- Turtle, E. P., Pierazzo, E., Collins, G.S., Osinski, G.R., Melosh, H. J., Morgan, J.V., Reimold, W. U., 2005. Impact structures: What does crater diameter mean? In: Kenmannn, T. Horz, F., Deutsch, A. (eds.) *Large meteorite impacts III: Geological Society of America Special Paper*, v. 384, p. 1-24.
- von Dalwigk, I. & Ormö, J., ????, Formation of resurge gullies at impacts at sea: The Lockne Crater, Sweden, *Meteoritics & Planetary Science*, v. 36, p. 359-369.
- Wasson, 1974 *In* Reading, H. G., 1996. *Sedimentary Environments: Processes, Facies and Stratigraphy*. Blackwell Science Ltd, Oxford, pp. 407-516.
- Wehr, A. and Lohr, U., 1999, Airborne laser scanning - an introduction and overview. *ISPRS Journal of Photogrammetry and Remote Sensing*, v. 54, p. 68-82.
- Wentworth, 1922 *In* Boggs, S., Jr., 2006, *Principle of Sedimentology and Stratigraphy*, Pearson Education, Inc., New Jersey, pp. 623.

- White, A.F., Buller, T.D., Vivit, D.V., Clow, D.W., 1998, The role of disseminated calcite in the chemical weathering of granitic rocks, *Geochimica et Cosmochimica Acta*, v. 63, p. 1939-1953.
- Worsley and Nakrem, 2008 *In* Ramberg, I.B., Bryhni, I., Nottvedt, A. & Rangnes, K. (eds)., 2008, *The Making of a Land: Geology of Norway*, Geological Society of Norway, 640pp.

## APPENDICES

**Appendix 1.** The strike measurement of beds and structures from the RITF-1 and RITF-4.

RITF-1			RITF-4		
no.	bed/structure	strike	no.	bed/structure	strike
1	ripple	216	1	bed	288
2	channel	230	2	bed	10
3	channel	240	3	ripple	294
4	bed	243	4	bed	288
5	ripple	248	5	ripple	275
6	ripple	250	6	ripple	272
7	bed	251	7	bed	280
8	ripple	255	8	ripple	265
9	ripple	255	9	bed	286
10	bed	261	10	ripple	270
11	ripple	279	11	ripple	268
12	ripple	279	12	ripple	262
13	trough	358	13	ripple	257



**Appendix 2.** The mineral estimation from X-ray diffraction (XRD).

Facies association	Sample name	Stilpnomelane %	Siderite %	Pyrite %	Chlorite %	Muscovite + Biotite %	Quartz %	K-feldspar %	Plagioclase %	Calcite %	Dolomite %	Actinolite %
FA3	RITF-3-6-09	0,00	0,44	0,92	1,72	0,34	11,31	56,82	21,08	1,29	0,77	5,32
	RITF-3-5-09	0,00	1,69	0,88	0,66	28,56	3,43	28,61	33,17	0,49	0,49	2,01
	RITF-3-4-09	0,00	0,54	0,30	0,47	2,53	8,72	69,31	12,59	0,97	3,00	1,57
	RITF-3-3-09	0,00	0,30	0,00	0,49	10,44	3,99	31,52	36,24	12,96	1,18	2,88
	RITF-3-2-09	1,13	0,64	0,63	4,51	2,86	5,81	38,54	40,62	0,31	2,00	2,96
	RITF-3-1-09	0,42	0,60	0,00	1,79	2,87	6,88	23,82	58,04	0,59	1,76	3,24
	RITF-4-8-09	0,54	0,46	0,00	3,33	3,65	4,61	35,04	37,76	11,03	1,28	2,30
	RITF-4-7-09	0,90	0,82	0,09	5,67	4,03	5,36	30,22	48,86	0,42	1,27	2,35
	RITF-4-6-09	1,51	0,95	0,21	7,79	4,50	10,03	30,27	37,98	0,73	2,11	3,92
	RITF-4-3-09	0,60	0,53	0,00	8,95	1,01	3,52	32,08	48,99	1,54	1,20	1,57
FA2	RITF-1A-3-09	1,02	0,57	0,00	2,29	4,39	5,44	41,90	37,79	1,39	1,87	3,34
	RITF-1A-2-09	0,39	0,80	0,13	9,73	3,90	7,54	27,13	44,12	0,46	1,27	4,51
	RITF-1A-1-09	0,00	1,07	0,00	4,98	0,27	7,49	34,17	44,32	2,02	2,08	3,59
	RITF-1-5-09	0,00	0,92	0,00	8,80	0,35	6,90	31,03	45,80	1,37	1,91	2,93
	RITF-1-3-09	0,00	0,51	0,15	0,63	4,45	2,81	12,32	11,17	65,65	0,88	1,44
	RITF-1-4-09	0,00	0,75	0,26	1,95	4,73	4,48	15,61	20,18	48,83	1,24	1,97
	RITF-1-6-09	0,32	2,14	0,56	6,26	1,75	11,49	34,21	33,25	0,96	3,52	5,53
	RITF-1-7-09	1,29	0,79	0,28	3,46	0,72	6,21	45,23	37,80	0,64	1,44	2,13
	RITF-1-2-09	0,00	1,90	0,00	6,00	0,67	13,33	34,36	31,86	3,68	3,08	5,12
	RITF-1-1-09	1,11	1,45	0,00	13,46	3,41	15,25	31,97	22,61	1,89	3,59	5,24
FA1	RITF-1-8-09	0,00	0,90	0,00	6,96	0,65	7,13	39,54	38,78	0,50	2,14	3,39
	RITF-4-5-09	0,00	0,24	0,00	17,16	5,88	8,13	25,90	37,57	0,44	2,08	2,59
	RITF-4-1-09	3,09	1,33	0,07	0,83	7,41	6,85	31,63	34,38	8,49	2,62	3,31
	RITF-4-4-09	2,10	2,65	0,39	1,21	17,29	12,77	28,72	18,61	5,55	5,43	5,29
	RITF-4-2-09	0,00	5,53	0,00	6,99	3,78	20,86	39,11	11,51	0,00	8,66	3,56

**Appendix 3.** The mineral counting in thin sections.

Facies association	Sample name	Mono-quartz %	Poly-quartz %	Feldspar %	Chlorite %	Carbonates %	Actinolite %	Heavy minerals %	Biotite %	Muscovite %	Matrix %	Rock fragments %	Pyrite %	Serycite %
FA3	RITF-3-6-09	11,48	0,00	52,15	0,96	0,00	3,59	0,48	12,68	0,24	6,94	10,77	0,00	0,81
	RITF-3-3-09	12,85	0,00	25,23	0,47	10,98	0,00	0,70	7,01	0,93	14,95	25,66	0,00	1,21
	RITF-3-2-09	4,47	0,00	32,27	6,71	0,32	2,24	0,64	3,51	0,32	5,75	42,98	0,00	0,79
	RITF-4-8-09	9,98	0,00	42,93	1,71	6,59	0,24	0,24	3,90	0,24	4,88	29,51	0,00	0,00
	RITF-4-7-09	10,28	0,00	28,01	0,00	0,00	0,00	0,00	6,38	0,00	10,28	45,04	0,00	0,00
	RITF-4-6-09	26,91	1,20	38,74	3,15	0,00	3,39	0,97	18,89	0,24	7,26	0,24	0,00	0,00
	RITF-4-3-09	14,22	0,90	50,63	4,62	15,13	0,00	0,21	5,25	0,00	0,21	8,82	0,00	0,00
FA2	RITF-1-5-09	14,29	0,00	72,18	7,27	0,00	0,75	0,50	1,00	0,00	4,01	0,00	0,00	0,00
	RITF-1-4-09	11,82	0,00	32,82	0,00	47,70	0,00	0,00	7,22	0,44	0,00	0,00	0,00	0,00
	RITF-1-6-09	20,34	0,00	57,44	1,47	0,00	0,21	1,05	4,19	1,47	13,84	0,00	0,00	0,00
	RITF-1-2-09	26,75	0,00	51,38	2,76	0,00	1,27	2,97	10,62	1,06	3,18	0,00	0,00	0,00
	RITF-1-1-09	25,54	1,60	60,00	3,17	0,49	3,17	1,22	3,66	1,22	1,46	0,73	0,00	0,73
FA1	RITF-4-5-09	20,25	0,00	50,62	5,68	0,00	0,99	1,48	6,91	0,00	13,83	0,25	0,00	0,00
	RITF-4-1-09	8,01	0,12	16,03	1,07	7,91	4,70	0,85	0,64	0,00	16,45	44,23	0,00	0,00

**Appendix 4.** The thin section description (part 1).

<b>Facies association</b>	<b>Sample name</b>	<b>Lithology</b>	<b>Compaction</b>	<b>Predominant structures</b>	<b>Average grain size</b>	<b>Most common grain shape</b>	<b>Sorting</b>	<b>Remarks</b>
<b>FA3</b>	RITF-3-6-09	breccia	strong	parallel lamination	fine sand	subangular	good	Biotite flakes have preferred direction. Fining upwards.
	RITF-3-3-09	breccia	weak	-	medium sand	angular	poor	Clast are filled with calcite. Large biotite flakes.
	RITF-3-2-09	breccia	moderate	-	medium sand	angular	moderate	-
	RITF-3-1-09	breccia	moderate	parallel lamination	fine sand	angular	poor	Fining upwards fine sand.
	RITF-4-8-09	conglomerate	moderate	-	fine sand	subangular	good	-
	RITF-4-7-09	conglomeratic sandstone	moderate	parallel lamination	medium sand	angular	poor	-
	RITF-4-6-09	sandstone	moderate	parallel lamination	fine sand	subangular	good	Homogenous fine sand.
	RITF-4-3-09	conglomeratic sandstone	strong	parallel lamination	fine sand	subangular	moderate	-

\ **Appendix 4.** The thin section description (part 2).

<b>Facies association</b>	<b>Sample name</b>	<b>Lithology</b>	<b>Compaction</b>	<b>Predominant structures</b>	<b>Average grain size</b>	<b>Most common grain shape</b>	<b>Sorting</b>	<b>Remarks</b>
<b>FA2</b>	RITF-1A-2-09	sandstone	moderate	-	fine sand	subangular	moderate	Well cemented fine sand.
	RITF-1A-1-09	sandstone	weak	-	medium sand	angular	poor	Local calcite cement concentration.
	RITF-1-5-09	sandstone	strong	fractures	medium sand	angular	moderate	Fractures filled with calcite.
	RITF-1-3-09	sandstone	weak	fractures	fine sand	subangular	moderate	Elongated grains have preferred direction. Well calcite cemented fine sand. Fractures filled with calcite.
	RITF-1-4-09	sandstone	weak	-	fine sand	subangular	moderate	Elongated grains have preferred direction. Well calcite cemented fine sand.
	RITF-1-6-09	sandstone	moderate	parallel lamination	medium sand	angular	moderate	Alternating very fine sand and upwards coarsening medium sand layers.
	RITF-1-2-09	sandstone	strong	parallel lamination	very fine sand	angular	moderate	Elongated grains follow the bedding. Fining upwards.
	RITF-1-1-09	sandstone	strong	parallel lamination	very fine sand	angular	good	Alternating silt and upwards fining very fine sand layers
<b>FA1</b>	RITF-4-5-09	breccia	moderate	-	fine sand	subangular	poor	Homogenous fine sand.
	RITF-4-1-09	breccia	moderate	-	coarse sand	angular	poor	Brown shards (melt?) in a matrix.
	RITF-4-4-09	suevite	moderate	-	very fine sand	angular	moderate	Fining upwards fine sand.
	RITF-4-2-09	suevite	moderate	melt particles	fine sand	angular	poor	Clasts and brown shards of altered melt rocks within matrix.

